CHALMERS
UNIVERSITY OF TECHNOLOGY

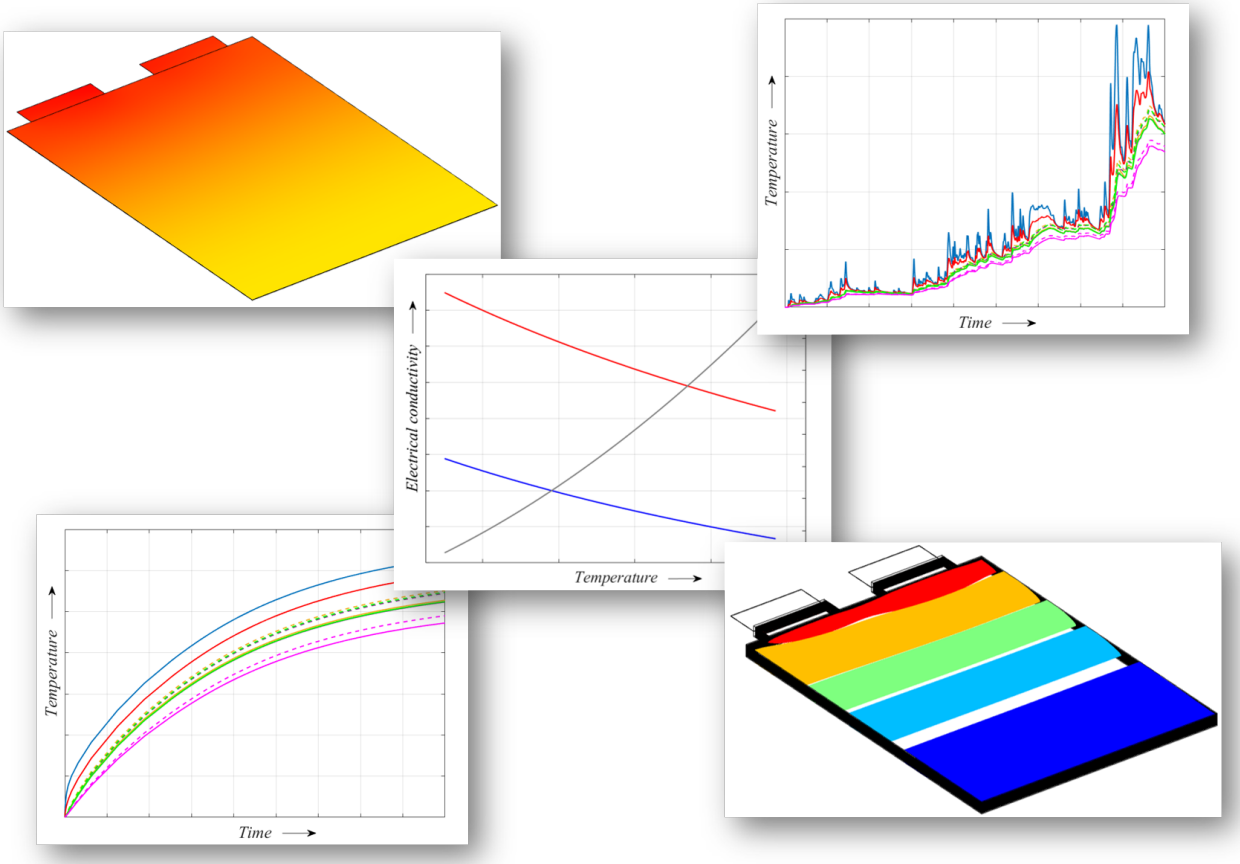

Anisotropic Temperature Distribution within Li-ion Cells in EV Batteries

an electro-thermal approach

Master's thesis in Automotive Engineering

SAURABH BIDARI

Department of Electrical Engineering
CHALMERS UNIVERSITY OF TECHNOLOGY
Gothenburg, Sweden 2020

Master's thesis in Automotive Engineering

Anisotropic Temperature Distribution within Li-ion Cells in EV Batteries

SAURABH BIDARI

CHALMERS
UNIVERSITY OF TECHNOLOGY

Department of Electrical Engineering
Chalmers University of Technology
Gothenburg, Sweden 2020

Anisotropic Temperature Distribution within Li-ion Cells in EV Batteries
an electro-thermal approach
SAURABH BIDARI

Academic Supervisors : Torbjörn Thiringer and Zeyang Geng, Department of Electrical Engineering, Chalmers University of Technology, Gothenburg, Sweden

Industrial Supervisors : Keerthana Arjun and Torbjörn Larsson, ART Power and Energy, Volvo Cars, Gothenburg, Sweden

Examiner : Torbjörn Thiringer, Professor, Department of Electrical Engineering, Chalmers University of Technology, Gothenburg, Sweden

Department of Electrical Engineering
Chalmers University of Technology
SE - 412 96 Gothenburg
Sweden
Telephone +46 (0)31 772 1000

Cover: Volumetric temperature distribution in a unit cell (top left), isothermal contours in a full cell (bottom right), plots of conductivity variation with temperature (centre), temperature variation over time for 2C current (bottom left) and for WLTC current (top right).

Typeset in LaTeX
Printed by Chalmers Reproservice
Gothenburg, Sweden 2020

Anisotropic Temperature Distribution within Li-ion Cells in EV Batteries
an electro-thermal approach
SAURABH BIDARI
Department of Electrical Engineering
Chalmers University of Technology

Abstract

One of the most crucial issues in the electric vehicle ecosystem is the service life of the Li-ion battery pack. As the cell's energy and power density improve, there has also been a reduction of thermal losses due to the internal resistance which depends on the electrical, chemical, thermal and mechanical properties of cell materials and their mutual interactions. Temperature plays a vital role in cell performance, safety and the nature of regular operation defines the variability of service life. For a cell with a volume of 225 cm^3, as in the current study, heat distribution through the volume becomes essential, especially when the constituent materials are anisotropic, temperature-sensitive and possess poor thermal properties which inhibit effective heat dissipation. This master thesis deals with understanding the interdependence of multiple physics contributing to the cell operation and creating an electro-thermal model of a Li-ion pouch cell determining temperature distribution within the cell volume. The finite element method is employed in multi-physics simulations. Experimental test results are also utilized to calibrate the model to improve its accuracy and reliability. Pulse tests and standardized drive cycle current profiles are fed as input to correspond real vehicles on-road operations, hence obtaining respective temperature distributions.

It is observed that the temperature is the highest at the positive tab than at the negative and a substantial difference in temperatures at the cell surface and cell core is detected. The higher temperatures at the specific sections of the cell correspond with the experimental results. A difference of 3.3 °C is detected between extremes, i.e., positive tab and lower cell surface while the difference between the cell surface and cell core peaked at 0.5 °C for boundary conditions of an ambient room at 20 °C and 2C electric current.

A reference vehicle model with minor modifications is used to compare the powertrain thermal management system (TMS) performance. The TMS which used cell core temperature as a cooling actuation parameter demonstrated a marginally higher drop in the state of charge as opposed to the system using cell surface temperature. This is due to the longer cooling requirement in the former case. However, the improvement in battery pack service life is not quantifiable because of single-cycle simulations and the complex chemical degradation phenomenon occurring over the cell lifetime. This reflection and its derivations provide an interesting scope for future studies.

Keywords : Powertrain, Li-ion batteries, Internal resistance, thermal management systems, Finite Element Analysis, electro-thermal modeling.

Acknowledgements

The thesis work has been carried out at the Division of Electric Power Engineering, Department of Electrical Engineering at Chalmers University of Technology, Sweden and ART Power and Energy, Volvo Cars, Sweden.

I would like to express my gratitude to,

- Torbjörn Thiringer and Zeyang Geng for their continuous support, patient guidance, regular technical reviews and motivating me throughout the research duration.
- Keerthana Arjun and Torbjörn Larsson for encouraging and mentoring me through these uncertain times while managing their commitments at the ART.
- Evelina Wikner for all the help and co-operation in providing detailed theoretical background behind cell operation, valuable insights on temperature effects and ageing.
- The 48 V System team at Volvo Cars for their untiring support and creating a welcoming, inclusive environment by involving me in technical discussions and project meetings hence familiarising me to the fascinating Swedish workplace.

Saurabh Bidari
Gothenburg, September 28, 2020

Contents

Nomenclature

ICE	-	Internal Combustion Engine
ICEV	-	Internal Combustion Engine Vehicle
HEV	-	Hybrid Electric Vehicle
BEV	-	Battery Electric Vehicle
FCEV	-	Fuel cell Electric Vehicle
EV	-	Electrified Vehicle
TMS	-	Thermal Management System
BTMS	-	Battery Thermal Management System
BMS	-	Battery Management System
SoC	-	State of Charge
WLTC	-	Worldwide harmonized Light duty driving Test Cycle
NEDC	-	New European Driving Cycle
CFD	-	Computational Fluid Dynamics
CAD	-	Computer Aided Design
EM	-	Electric Machine/Motor
Al	-	Aluminum
Cu	-	Copper
Li	-	Lithium
Co	-	Cobalt
e^-	-	Electron
OCV	-	Open circuit voltage
A/C	-	Air conditioning
IM	-	Induction Machine
PMSM	-	Permanent Magnet Synchronous Machine
VCR	-	Vapour Compression Refrigeration

1

Introduction

The urgency to transition from fossil fuel energy sources to sustainable, low-carbon energy providers has amplified during the past decade. Most industries have realized the need for this transition. They hence have correspondingly started transforming their respective business models by taking suitable actions. Next to the collective emissions from electricity generation in power plants, the transportation industry has long been responsible for carbon emissions [1]. The same is demonstrated in Figure 1.1. Most automotive manufacturers have started pushing hard towards the electrification of their product portfolios [2]. Many federal governments have also been considering incorporating new transformative norms for the automotive industry in their economic recovery packages announced due to the COVID-19 global pandemic.

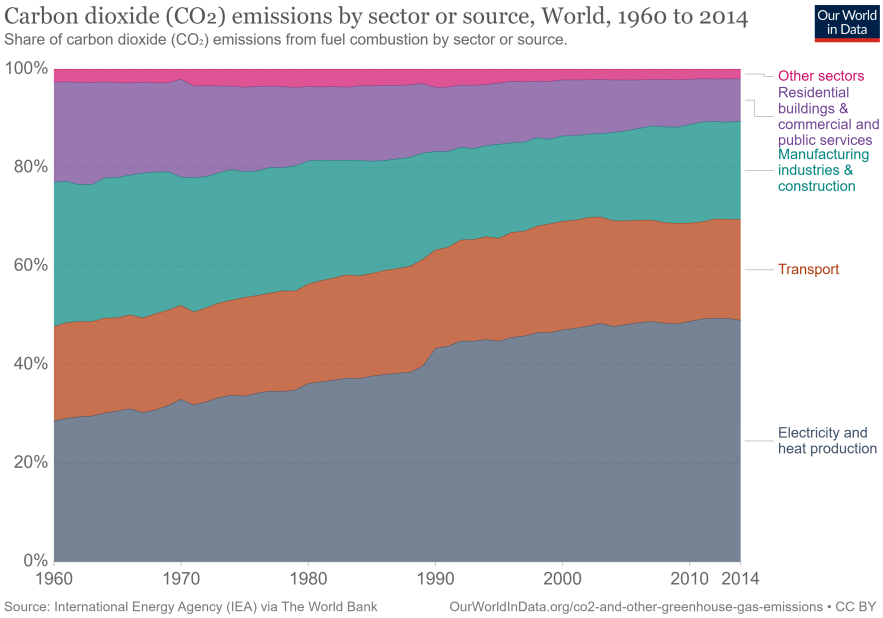

Figure 1.1: At the end of 2014, GHG emissions share were Electricity and heat production:49.04%, Transport:20.45%, Manufacturing and construction:19.96% and the rest accounting for about 10% [3]

Antithetical to the complexity of ICEV and HEV, BEV is relatively simpler based on the propulsion systems' perspective as there are relatively fewer moving parts. The energy source used defines the energy conversion method to be employed in the vehicles. High energy density fossil fuels need an ICE for converting chemical energy

to use into propulsion energy. In contrast, relatively lower energy-dense batteries need electric motors for converting electrical energy to useful propulsion energy in a HEV and a BEV. The development of highly optimized electric powertrains by seamlessly integrating hardware and software has become one of the vehicle manufacturers' prime challenges. This has compelled the EV battery suppliers to their limits in order to show appetence for high energy, power-dense batteries and deliver them in unprecedented lead times [4]. Figure 1.2 shows the past and projected Li-ion battery demand for different categories of transport.

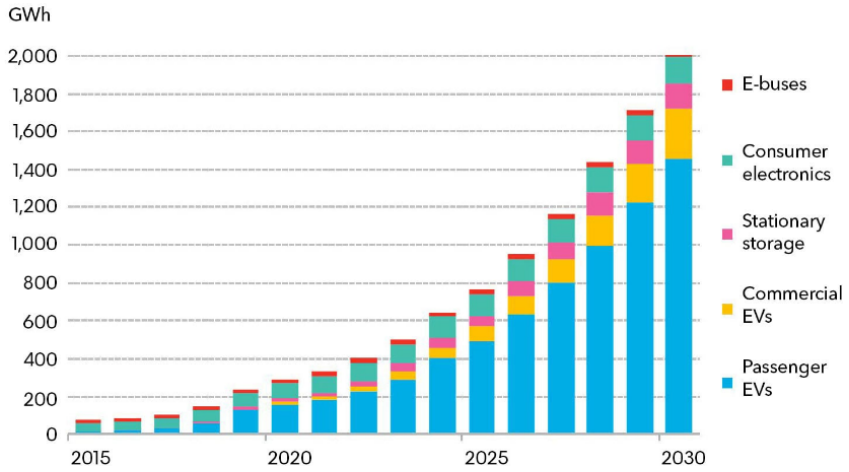

Figure 1.2: Bloomberg NEF 2019 forecast for annual Li-ion battery demand depicting majority share of passenger EVs beyond 2020 [5]

1.1 Problem Background

Volvo Cars has committed to the sustainable design of vehicles for a cleaner environment, which is reflected in its ambitious climate plans for future [6]. It intends to reduce the CO_2 emissions per car by 40% before 2025 and become climate neutral by 2040 [6]. VCC aims to sell 1 million electrified vehicles by 2025 and at the same time, stop the new development of pure ICEV [6]. Hence, most of the upcoming Volvos' will be either a BEV or an HEV with at least 48 V system, i.e., Mild hybrids [6]. Since the battery pack is a crucial component in the vehicles with some or other electric drive forms, proper optimization of this critical component becomes necessary. From the recent developments in battery technologies, Li-ion batteries stand out to have more relative advantages than disadvantages compared to lead-acid and Nickel-based batteries [7][8]. Li-ion battery performance and service life are strongly dependent on the temperature. Surprisingly, a reasonably high temperature is desired as the losses are lower due to a low resistance at higher temperatures [9]. However, it is essential to limit the average temperature to below 45 °C to decelerate aging and achieve a longer service life [9], which can be achieved by using a suitable BTMS. Typically, BTMS is a part of the BMS, which has a more extensive range of functions like monitoring of battery voltages, currents, SoC along with charging, cell voltage balancing, among other vital tasks [7].

BTMS is a closed-loop control system that continuously monitors the battery temperatures. Consequent to the extremes attained, it actuates the thermal management system based on specific pre-set target parameters. Typically, the temperature sensors of a BTMS are attached to some centrally placed cell surfaces within the battery pack, which leads to an underestimation of the actual cell temperature, i.e., within the cell [9]. The temperature within a cell could have reached much higher magnitudes as constituent materials' thermal conductivity (separator in particular) is significantly low compared to its neighboring components. This limits the heat dissipation to the heat sink - in the current case, the coolant used. It is to be noted that when the core temperatures are around 90 to 120 °C, a phenomenon called thermal runaway occurs. During this phenomenon, the exothermic reactions take over the heating and induce permanent damage in the battery cell [9] and can lead to critical battery pack fires [10].

A sufficiently high amount of electrical energy needs to be stored on-board the EV with well-balanced power and energy density to propel the vehicle, which typically weighs over 1600 kg [11]. Lithium-ion batteries, incorporating high energy densities while being relatively easy to operate, turn out to be a viable solution. However, Lithium-ion batteries need proper thermal optimization for the best possible performance characteristics [12]. This can be done in different ways. Two important examples are,

- by refining the materials used which govern the electro-chemical processes and are the basis for cell operation[13]
- by designing a thermal management system to ensure that the battery pack's temperature remains in the optimum range for cell reactions to occur effectively without a high rate of aging [14].

Both the above options tend to be challenging due to the nascency of a Li-ion cell application in high voltage EV and hence need to be addressed. Therefore, the concurrent work deals with the latter option of effective thermal management down from the root cell level. This ultimately has to account for variable external environmental factors while still serving the necessary driver's demands and optional auxiliary system power requirements during normal operations.

1.2 Objectives

- To develop a 3-dimensional electro-thermal model of a battery cell in a more detailed level where the geometry, anisotropic material properties of the electrode, separator, electrolyte and casing are taken into consideration.
- Use the developed electro-thermal model to estimate the battery cell internal temperature for various set of ambient conditions. The internal cell temperatures are functions of specific load cycles and cooling strategies used.
- To model and simulate two BEV thermal management models operating with standardized WLTC,

  a). one with a BTMS which uses the cell surface temperature as the control parameter

b). another with a BTMS using the cell core temperature from the electro-thermal model as the control parameter

1.3 Specifications of the Issue under Investigation

The current thesis work would address the following,

- The temperature distribution within the entire cell volume in x, y and z directions with a simple cooling arrangement.
- Real-time surface temperature of the cell when the cooling system needs to be actuated while the internal temperature has reached the stipulated limit.
- If there is any driving range improvement or hindrance due to the new target control parameters determined from the electro-thermal model.
- If the modeled cooling circuit is good enough to effectively cool the battery pack at high power demand applications like rapid accelerations, top speed operations and if necessary, suggest appropriate changes to meet the demands.

1.4 Delimitations

In order to have simplicity in the modeling, only BEV cooling systems will be considered as the HEV cooling systems are relatively more complicated due to the presence of an ICE. Heat transfer by conduction and convection will be considered, while no radiation effect will be taken into account due to a relatively lower heat loss by that means. The experimental verification of internal temperatures from the battery cell model developed is not carried out since it involves cell disassembly. However, surface temperatures are estimated from the model and compared with experimental results. When the vehicle model is designed to evaluate the cooling system's effectiveness and performance of a BEV, a simple vehicle model is used where a set of battery modules are simplified and considered as a single thermal node, which in turn constitute the battery pack. No detailed CFD simulations of the cooling system in COMSOL - Multiphysics® will be performed. Battery cell aging is a complex function of cycle aging and calendar aging mechanisms that are independent. Hence, a detailed qualitative and quantitative analysis of the reduction in the battery pack's aging rate and its constituent cells are ignored in this study.

2

Theory

The use of EVs dates back to the 19th century when horse carriages and buggies were the primary modes of transport and innovative engineers were planning to transform the transportation industry. With the invention of combustion engines powered by coal, gasoline, and diesel, an industry transformed reluctantly against the influence of innovators' efforts who built the galvanic cell-powered carriages. Due to a relatively higher energy density, convenient availability of fossil fuels and the desired longer range from competing combustion engines, the ICEV success overshadowed the EV [15]. EV growth seems relatively new when compared to the historical use of high power electricity in heavy transport like trains and city trams. Nevertheless, the use of electrical energy in first passenger vehicles dates back to 1881 in Gustave Trouvé's tricycle [16] and 1901 in Ferdinand Porsche's 'Semper Vivus', the first HEV [17], both presented in Figure 2.1.

In this chapter, a brief explanation of the theoretical background necessary to carry out the contemporary work in a concisely-structured way is laid out. It ranges from the basics of heat transfer while glancing through the aspects of battery cells and ends with describing the EV thermal management system. It is to be noted that the A/C system, which underlines the luxury and passenger comfort, is not considered in the study and any reference to the same is exclusively related to the powertrain cooling. However, the omission of the same does not in any way undermine its importance.

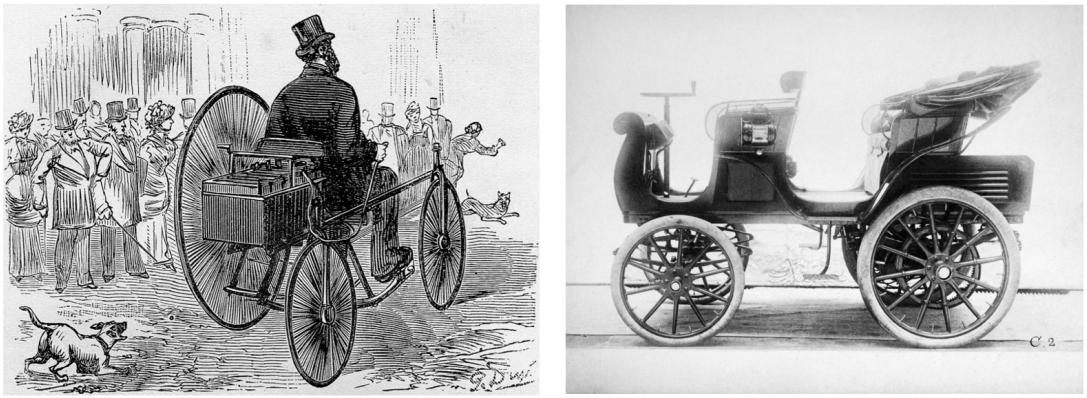

a b

Figure 2.1: The first EV, (a). Gustave Trouvé's tricycle (1881) [16] and (b). Ferdinand Porsche's Semper Vivus (1901) [17]

2.1 Electrified Vehicles - HEV and BEV

Conventional vehicles powered by combustion engines have a smaller 12 V lead-acid battery which serves as the power source for the auxiliary electrical/electronic systems in the vehicle. It is recharged during regular operation by an EM, which is known as the alternator. Its other function is to provide power to the auxiliary loads during normal operation. Another EM is affixed next to the engine with the primary function to crank up the engine during start-up and hence is called the Starter. Figure 2.2 illustrates the classification of vehicles based on the fuel source and propulsion device employed. As seen, in the case of EVs that comprise hybrids ranging from mild hybrids to PHEVs and complete BEVs, the use of Li-ion batteries has become standard but with varying energy content and operating voltages. In the automotive industry, high voltage refers to voltages over 60 V, which is typically found in EVs with EM power above 12 kW [18]. High voltage encompasses Mild Hybrids, all Full Hybrids, PHEV, FCEV and BEV. Figure 2.3 depicts the EV classification based of system parameters.

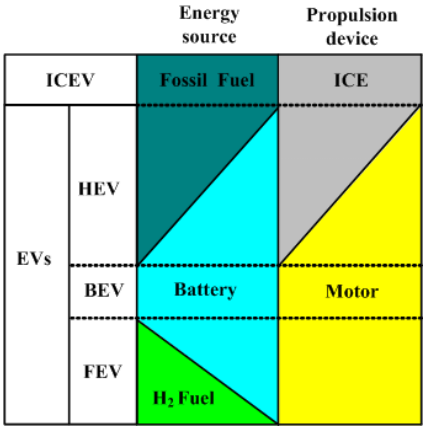

Figure 2.2: Vehicle classification based on fuel source used and propulsion device employed [19]

2.2 Importance of Heat Transfer Mechanisms

Heat energy is one of the most convenient forms of energy as it can be transferred by all known means, i.e., with or without the availability of transfer media. The energy flow is always from a body/section at a higher temperature to lower temperature analogous to water flow from a higher elevation to lower or charge flow from a region of higher potential to lower. In Li-ion cells, primarily, heat transfer within the cell dominantly occurs by conduction (as the material is solid) and the heat transfer from the cell surface to the coolant takes place through convection. The radiation heat transfer is promptly neglected as the temperature difference between the cell surface and the ambient is relatively low to account for radiation loss. As explained by *Cengel et al.* in [20], radiation heat loss becomes significant enough to consider only if the temperature difference between the source (cell) and the sink

E-mobility performance class overview for passenger vehicles										
		Mild Hybrid			Full Hybrid/Plug-in		EV (Batt/RE/FC)			Unit
		12 V	48 V	HV	mid	Power	Small car	Medium car	Sports car	
max. EM Power	motor-based	4	12	20	60	100	60	100	180	kW
max. EM Speed	motor-based	50	150	150	200	300	200	300	500	Nm
DC voltage	max. (generator-based)) min. (motor-based)	15 12	60 36	200 120	400 300	450 250	400 300	400 300	450/800 300/600	V V
max. current	DC AC	333 350	333 500	167 500	200 600	400 800	200 250	333 450	550/280 1000/500	A A
Speed/crankshaft speed ratio or max. EM speed		3	1	1	1	1	10–15 k/min		bis 20 k/min	
Power ratio max./duration		2	2	2	2	2.5	1.5	1.5	2	

Figure 2.3: EV classification based on primary voltage source used and EM power category [18]

(ambient/coolant) is higher than 300 °C. Table 2.1 represents the analogous comparison between the charge, heat and fluid transfer illustrating electrical, thermal and hydraulic circuits, respectively.

Table 2.1: Parametric comparison between Electrical, Thermal and Hydraulic circuits

	Electrical	**Thermal**	**Hydraulic**
Potential	Voltage	Temperature	Pressure
Flow	Current	Heat	Discharge (volume flow)
Opposition	Resistance	Thermal resistance	Hydraulic resistance (Viscosity, bends/turns)

2.2.1 Conduction

Conduction heat transfer occurs within solids or between solids in physical contact. As the heat energy is supplied to a solid, the constituent molecules start vibrating with higher amplitudes and frequencies and after reaching a limit called melting point, the closely packed molecules dissociate into the liquid phase. As a basic principle in heat transfer, a body above absolute zero (0 K) always has its constituent particles in vibration. Heat transfer through conduction is dependent on the thermal conductivity of the material, the temperature difference between points/surfaces of interest and the cross-sectional area for the heat flow. In a 1-D steady-state system, (2.1) represents the heat flow $Q_{conduction}$ through a solid with thermal conductivity k with one end of the solid at temperature T_1 which is continuously heated and T_2 is the temperature at a distance of δx from T_1 while A is cross-sectional area normal to $Q_{conduction}$. The same is shown in Figure 2.4. From Fourier's law of heat conduction, the above parameters are related as,

$$Q_{conduction} = kA\frac{(T_1 - T_2)}{\Delta x} = kA\frac{\delta T}{\delta x} \tag{2.1}$$

In the limiting case when $\Delta x \to 0$, (2.1) reduces to differential form and is given by,

$$Q_{conduction} = kA\frac{dT}{dx} \tag{2.2}$$

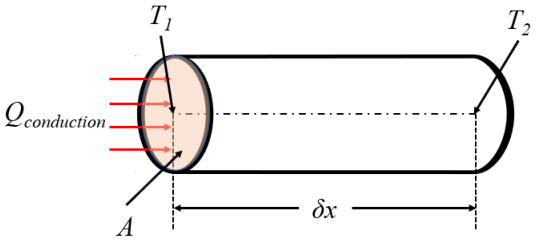

Figure 2.4: Heat transfer through a cylindrical body with thermal conductivity k

Here, k [W/m · K] characterises the material's ability to conduct heat. Typically, metals have higher thermal conductivity except for a few non-metallic conductors. One unique among them is Diamond. Diamond's thermal conductivity ($k = 2300\,\mathrm{W/m \cdot K}$) is almost over 5 times that of Silver ($k = 429\,\mathrm{W/m \cdot K}$) [20]. Thermal conductivity is also a temperature function and hence does vary with changing temperature. However, the range in which the current work deals with has no considerable effect on the same and hence ignored.

When the heat transfer takes place through all three primary directions within a body, it is said to be 3-dimensional (3-D) heat transfer and is given by equations (2.3) and (2.4). Figure 2.5 represents the 3-D heat transfer.

$$Q_{conduction} = Q_x + Q_y + Q_z \tag{2.3}$$

$$Q_{conduction} = k_x A_x\frac{dT}{dx} + k_y A_y\frac{dT}{dy} + k_z A_z\frac{dT}{dz} \tag{2.4}$$

In case of isotropic materials, $k_x = k_y = k_z$ while for anisotropic materials, $k_x \neq k_y \neq k_z$.

2.2.2 Convection

The mechanism of heat transfer where the movement of constituent particles is due to the difference in their thermal energies is called convection. For example, the air molecules at higher temperature are less dense and possess higher thermal energy, while molecules at a lower temperature are dense and have lower thermal energy. This heat transfer involves contribution from conduction and from the motion of constituent particles. Generally, convection is found between the solid surface in contact with a moving fluid, be it gas or liquid. Considering a solid surface in contact with a fluid flowing on its surface, the heat is initially transferred to the

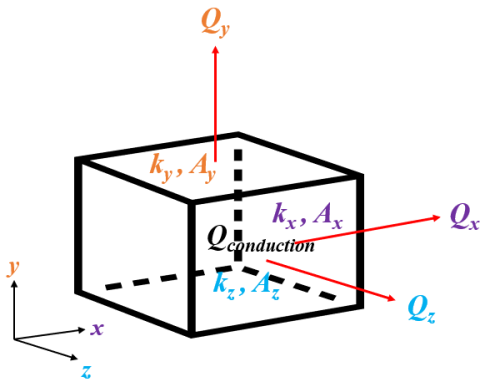

Figure 2.5: Heat transfer in a 3-D block

fluid molecules closest and in contact with the surface. Then, these warmed up molecules collide and transfer heat to the upper layers by conduction and then by moving upwards as the density of fluid molecules at higher temperatures is lower [20]. When the fluid is confined to narrow spaces and not at the liberty of free movement, the heat transfer in it is by conduction for instance, as in two solids with rough surfaces in contact with each other. The fluid between the voids formed due to crests and troughs as a result of rough surface conducts heat. Convection is a fairly complicated phenomenon when analysed against conduction.

A generalised equation for convection heat transfer $Q_{convection}$ between a solid surface at temperature T_s and fluid in motion at temperature T_∞ is given by (2.5). Figure 2.6 illustrates the steady-state heat transfer with blue and red arrows representing airflow and heat flow respectively.

$$Q_{convection} = hA(T_s - T_\infty) \tag{2.5}$$

where, A is the solid's surface area in contact with fluid and h is the heat transfer coefficient, which varies largely based on the fluid, velocity/flow rate and phase.

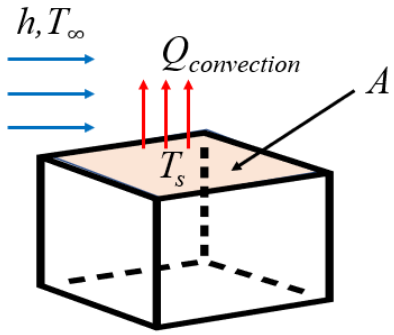

Figure 2.6: Heat transfer between a block surface and fluid in motion

When the fluid is induced to flow over a certain surface by use of external means like a blower, fan, the phenomenon is called *Forced Convection*. In contrast, if the fluid motion is only caused by buoyancy effects due to density differences as a result of different temperatures in different layers, it is characterized as *Natural Convection*.

2.2.3 Radiation

Heat transfer occurring between bodies above absolute zero temperature by electromagnetic waves constitutes radiation heat transfer. The heat energy from the stars in the cosmos reaches the revolving planetary bodies by radiation and Earth is no exception. It is also to be noted that these electromagnetic waves are not categorised as gamma rays, radio waves, x-rays, ultraviolet rays. Typically, radiation is considered as a surface phenomenon for opaque solids as the radiations from interior regions cannot reach the surface and incident radiation on surface cannot penetrate beyond a few microns. The maximum radiation heat released $Q_{radiation}$, from a body with surface area A, absolute temperature T_s is expressed using Stefan-Boltzmann law as,

$$Q_{radiation} = \sigma A {T_s}^4 \tag{2.6}$$

where, σ is the Stefan-Boltzmann constant with a magnitude of 5.67×10^{-8} W/m$^2 \cdot$ K^4. Figure 2.7 depicts the radiation heat transfer represented by red arrows from the shaded surface. The maximum radiation emitted by an ideal surface is called black body radiation and the body emitting it is called black body. Hence, the generalised equation for a body above absolute zero temperature is given by (2.7) where ϵ is the *emissivity* of the body.

$$Q_{radiation} = \epsilon \sigma A {T_s}^4 \tag{2.7}$$

Emissivity is the property which describes how closely a body resembles a black body which has $\epsilon = 1$ and hence, for rest of the surfaces - $0 < \epsilon < 1$ [20].

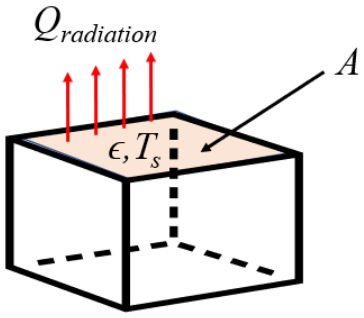

Figure 2.7: Steady-state heat radiation from a surface with ϵ at T_s

Though radiation constitutes for most of the energy transfer in the universe, its applicability in the current study scenario is negligible since ϵ and T_s are significantly lower. This leads to a sufficiently low radiation heat transfer when compared to conduction and convection. Therefore, the radiation heat transfer mechanism is ignored in the current study.

2.2.4 Steady-State Operation

When a specific small volume of a 1-D object is considered, there is a continuous exchange of thermal energy. A measurable quantity of heat flows into the volume Q_{in}

and a different quantity of heat flows out of the same volume Q_{out}. The difference between these quantities gives the rate of change of energy of the volume $\frac{dE_{vol}}{dt}$. These parameters are related as,

$$Q_{in} - Q_{out} = \frac{dE_{vol}}{dt} \tag{2.8}$$

However, after a sufficiently long duration, the rate of energy change becomes nil and a thermal equilibrium is attained. When a time-dependent process is executed for an extended period of time, which results in the attainment of a state where the resulting parameters attain equilibrium. The passing of time does not affect the state of the system. Hence, the underlying state reached known as steady-state is reached. This leads to (2.8) transformation as,

$$Q_{in} - Q_{out} = 0 \tag{2.9}$$

For 1-D conduction under steady-state,

$$Q_{in} = Q_{out} = Q_{conduction} = kA\frac{T_1 - T_2}{l} \tag{2.10}$$

where, T_1 and T_2 are wall temperatures at heat entry and exit of the volume respectively, whereas k and A are thermal conductivity and cross-sectional area for heat flow. l represents the transverse distance between the heat entry and the exit surfaces.

$$Q_{conduction} = \frac{T_1 - T_2}{R_{therm}} \quad \rightarrow I = \frac{V_1 - V_2}{R} \tag{2.11}$$

$$R_{therm} = \frac{l}{kA} \quad \text{[K/W]} \tag{2.12}$$

Equation (2.10) can be compared to an electrical circuit with temperatures analogous to potentials and heat flow to electric current and the thermal resistance (R_{therm}) is computed as in (2.12). Using a similar approach, heat transfer for convection can be corresponded to an electrical circuit and equivalent thermal resistance computed based on steady-state convection.

$$Q_{convection} = hA(T_s - T_\infty) = \frac{T_s - T_\infty}{R_{therm}} \quad \rightarrow I = \frac{V_1 - V_2}{R} \tag{2.13}$$

$$R_{therm} = \frac{1}{hA} \quad \text{[K/W]} \tag{2.14}$$

2.2.5 Transient Operation

In reality, most of the processes are short enough to fulfil their purpose based on the application and hence a steady-state is rarely reached. Especially in the present work, traction batteries are operated based on the power demand from the driver during driving maneuvers; hence a transient behavior is not uncommon. The heat generated by the battery varies continuously with time and a lumped

system analysis is a method to solve for the temperature while assuming uniformity throughout the study volume. However, it does not apply accurately to the battery due to anisotropic properties. However, a brief background of the lumped system is helpful in understanding the transient simulations carried out in the present work.

Considering a body with mass m, density ρ, surface area A volume V and specific heat capacity C_p at temperature T_{init} as shown in Figure 2.8. At time $t = 0$, it is placed in a medium at temperature T_∞ and heat transfer coefficient h. Let $T_\infty > T_{init}$ and as temperature is assumed to be uniform in the body, it only varies with time $T(t)$. Hence, in a time interval dt, the body temperature increases by dT. From energy balance, the heat transfer into the body in dt increases the energy of the body [20].

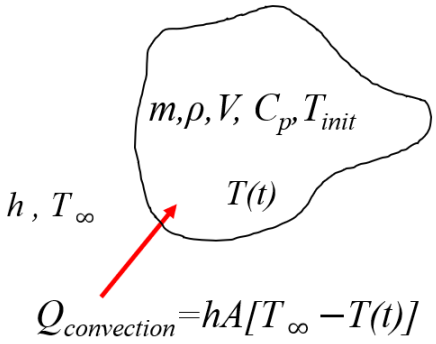

Figure 2.8: Arbitrary body with respective parameters for transient analysis

$$hA(T_\infty - T_{init})dt = mC_p\, dT \tag{2.15}$$

Since, $m = \rho V$, $dT = d(T - T_\infty)$ and T_∞ is constant external temperature, (2.15) can be written as,

$$\frac{d(T - T_\infty)}{T - T_\infty} = -\frac{hA}{\rho V C_p}dt \tag{2.16}$$

On integration from $t = 0$ when $T = T_{init}$, until anytime t when $T = T(t)$ leads to,

$$ln\frac{T(t) - T_\infty}{T_{init} - T_\infty} = -\frac{hA}{\rho V C_p}t \tag{2.17}$$

Using exponential function on both the sides and rearranging,

$$\frac{T(t) - T_\infty}{T_{init} - T_\infty} = e^{-\alpha t} \tag{2.18}$$

where,

$$\alpha = \frac{hA}{\rho V C_p} = \frac{hA}{m\ C_p} \quad [1/\text{s}] \tag{2.19}$$

α is positive in magnitude and is called *time constant* while its reciprocal has unit as [s].

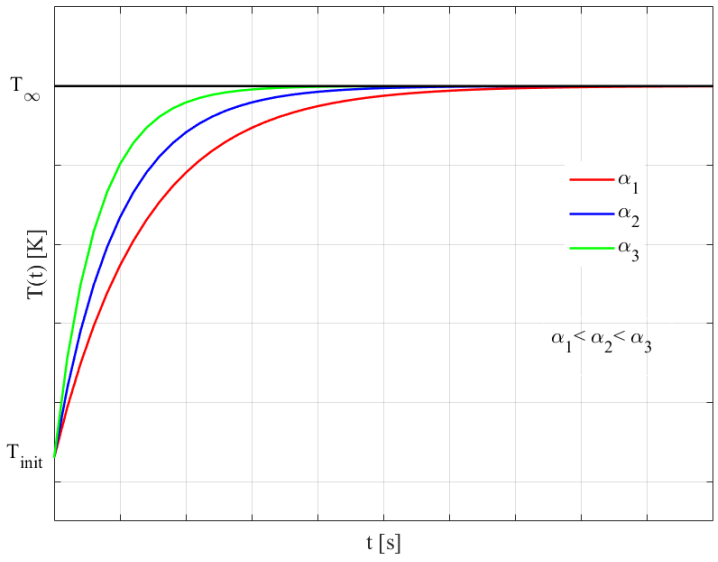

Figure 2.9: Variation of temperature with respect to time for different α

Hence, from (2.18), for different α, $T(t)$ at different time instants can be obtained.

For the highest value of α i.e., α_3, the body reaches steady-state temperature which is same as surrounding temperature T_∞ much faster than α_2 and α_1 which are lower than α_3.

From the Figure 2.9, one can determine the time required for the body to reach a certain target temperature, which is undoubtedly below the surrounding temperature. Subsequently, one can also analyse the time required for the body to reach a steady-state. It is easier to understand the same more intuitively as α is directly proportional to the area and inversely proportional to C_p, m. This means it takes longer for a heavier object to reach the steady-state than a lighter object and the inverse holds true for a body with a larger surface area than for a smaller area.

2.2.6 Thermal Contact Resistance

When multiple solids are in physical contact with each other and heat transfer is taking place between them, the concept of contact resistance comes into the picture. Practically, there is always some resistance to the heat flow at the interface between the two bodies in contact and this resistance per unit interface area is called thermal contact resistance R_c.

Consider the bodies A and B in Figure 2.10. As all the practical surfaces have irregularities on their surfaces, their surface roughness measures the extent to which a surface has a deviation in its crests and troughs. It is a primary parameter that determines the surface finish along with other measurements like flatness and waviness. Hence, two bodies in contact microscopically are actually in contact touch only at a few individual points. Even at contact pressures of 10 MPa, the actual contact area is $1 - 2\%$ of the nominal area [21]. This results in a sudden temperature drop δT, as shown in Figure 2.10 a. Typically, the contact resistance which

is the reciprocal of contact conductance is determined experimentally by a set of experiments in vacuum and media of interest.

As shown in Figure 2.10 b, the heat flux from solid A flows to B through contact spots ($Q_{contact}$) and the voids filled with fluid (Q_{gap}). Hence, the heat transferred at the interface is a combination of the above two modes.

$$Q = Q_{contact} + Q_{gap} \tag{2.20}$$

In analogous to Newton's law of cooling,

$$Q = h_c A\ \delta T \tag{2.21}$$

where, A is the apparent interface area and δT is temperature drop at interface. h_c corresponds to heat transfer coefficient is called thermal contact conductance computed as,

$$h_c = \frac{Q/A}{\delta T} \quad [\mathrm{W/m^2 \cdot K}] \tag{2.22}$$

As R_c is the reciprocal of h_c,

$$R_c = \frac{1}{h_c} = \frac{\delta T}{Q/A} \quad [\mathrm{m^2 \cdot K/W}] \tag{2.23}$$

The value of R_c is dependent on the fluid property in the voids/gaps, the surface roughness of contact faces, contact pressure. As expected, R_c seems to reduce with reducing surface roughness and increased contact pressure. Most of the experimentally determined contact resistance range between 0.000005 and 0.0005 $\mathrm{m^2 \cdot K/W}$ or thermal contact conductance of 2000 to 200000 $\mathrm{W/m^2 \cdot K}$.

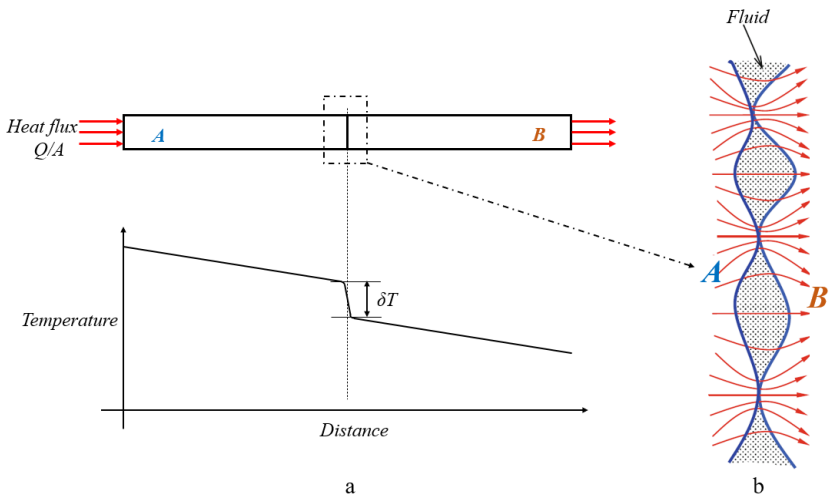

Figure 2.10: (a). Solids A and B with imperfect contact interface and constant heat flux through the assembly, (b). Microscopic representation of contact interface [21]

In the present study, application of thermal contact resistance exists between different layers within the cell. During the manufacturing of a Li-ion pouch cell,

current collectors coated with electrode materials are stacked and assembled with a separator between anode and cathode repetitively for multiple times. Furthermore, during the cell operation, the heat generated from the electro-chemical reactions flows to the surface by obeying the principles of contact resistance. However, since the material properties and surface roughness of the electrodes and separator are trade secrets and variability due to the addition of electrolyte cannot be approximated appropriately, the thermal contact resistances between layers in a cell are not considered in this study. One more plausible reason is the use of an electro-thermal approach which disregards mechanical pressures which act on the cell due to expansion and contraction during charging and discharging processes and hence a continuously varying contact pressure exists between cell layers. However, in some instances of experimental tests and corresponding simulations, the concept is used and justified.

2.3 Li-ion Batteries

With the onset of the industrial revolution in the late 18th century, energy storage and conversion to useful work became the prime focus of industrialists. Fossil fuels and steam, ICE fulfilled these blanks and propelled the developments. Eventually, as electrical energy became more familiar, various methods were being worked towards to store this efficient, noise-free and robust energy that could run the industries which were slowly being replaced by high capacity electric motors. Since then, various technological innovations have come to light, especially during the World wars and the electronics industry revolution starting with the transistors in 1947.

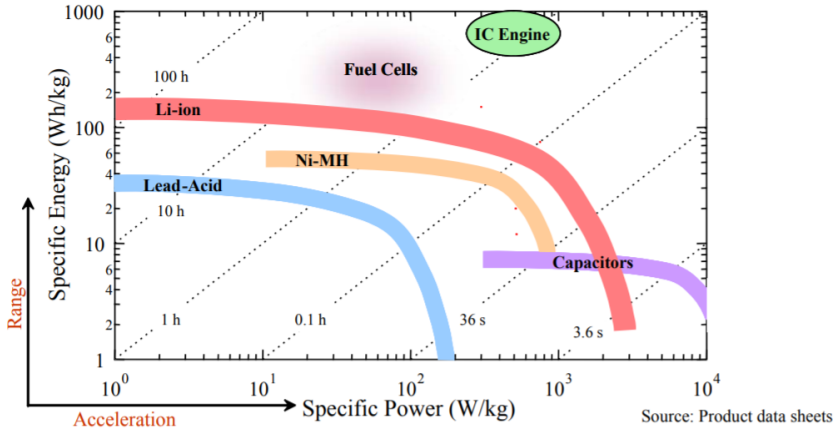

Figure 2.11: Ragone plot displaying the driving range and acceleration capability based on different kind of fuel sources used with their respective drive units [22]

One of the earliest electrical energy storage solutions was invented by Allesandro Volta in 1800, - Voltaic Pile [23]. As the technology improved by works of various pioneers and some major breakthroughs in the 19th and 20th centuries, Li-ion batteries came into existence. Other electrical energy storage devices like hydrogen fuel cells and super-capacitors have also been around and being used based on the different applications. However, after careful evaluation of the advantages and

disadvantages, Li-ion batteries have come up to extensive usage by less debatable conflicts. Due to their higher energy density and relatively moderate power density (which can be regulated by cell chemistry used). Li-ion batteries have become a plausible choice for most of the EV manufacturers with a sufficient balance between Driving range and acceleration capability. Figure 2.11 shows the Ragone plot enabling the proper choice of energy source based on applicability. The source furthest to the top right proves to be the best choice provided it is eco-friendly.

Table 2.2: Comparison between Capacitors, Super-capacitors, Hydrogen Fuel cells and Li-ion cells [24]

Property	**Supercapacitors**	**Capacitors**	**Hydrogen fuel cells**	**Li-ion cells**
Charge/Discharge time	ms to s	ps to ms	10 to 300 hrs. instant charge (refuel)	1 to 10 hrs
Operating temperature	-40 to +85 deg,C	-20 to +100 degC	+25 to +90 degC	-20 to +65 degC
Operating voltage	2.3 to 2.75 V	6 to 800 V	0.6 V	1.25 to 4.2 V
Capacitance	100 mF to 1500 F	10 pF to 2.2 mF	N/A	N/A
Life	50,000+ hrs, unlimited cycles	>100,000 cycleds	1500 to 10000 hrs	150 to 1500 cycles
Weight	1 g to 230 g	1 g to 10 kg	20 g to >5 kg	1 g to >10 kg
Power density	10 to 120 kW/kg	0.25 to 10000 kW/kg	0.001 to 0.1 kW/kg	0.005 to 0.4 kW/kg
Energy density	1 to 10 Wh/kg	0.01 to 0.05 Wh/kg	300 to 3000 Wh/kg	8 to 600 Wh/kg
Pulse load	up to 100 A	up to 1000 A	up to 150 mA/cm^2	up to 5 C

2.3.1 Battery Cell Terminologies

The general terminologies associated with batteries are described briefly as below.

1. *State of charge (SoC)*: The remaining charge capacity within a battery expressed as a fraction of maximum capacity is SoC. It is one of the most common terms which one can observe on electronic/electrical devices expressed in % [25].
2. *Depth of discharge (DoD)*: The amount of charge which has been consumed during an operation is depth of discharge [25]. It is opposite to that of SoC and is generally represented in %. Hence, when a battery is fully charged, its SoC is 100%, while DoD is 0% and vice-versa when the battery is fully discharged.

$$DoD = 100 - SoC \quad \% \tag{2.24}$$

3. *Terminal voltage*: The potential difference between the battery terminals when the circuit is complete with a load is the terminal voltage. It takes into account the potential drop across the internal resistance of the battery [25]. Terminal voltage also varies with SoC and current direction, i.e., charging or discharging.
4. *Open circuit voltage (OCV)*: The potential difference between the terminal of the battery without a load connected in the circuit.
5. *Internal resistance (R_{int})*: Internal opposition offered to the flow of charge when the circuit is completed is called the internal resistance. It is a strong function of temperature and moderately related to the current direction and SoC [25]. In large commercial batteries, R_{int} is of the order of $m\Omega$.

6. *Nominal voltage*: The reference voltage of a battery which is typically mentioned as voltage on batteries. It is also characterised as the normal voltage of the battery.
7. *Capacity*: The charge content of a battery is called its capacity and is expressed in Ah (ampere-hour) [25]. When the SoC is 100%, the battery is assumed to be at its highest capacity and at lowest when SoC is 0%. A battery of capacity 26 Ah is fully discharged if a constant current of 26 A is drawn for 1 hour from the initial SoC of 100%.
8. *C-rate*: It is the current at which a battery is charged or discharged and is expressed in A [25]. A C-rate of 1C for a 26 Ah cell means a constant current of 26 A while 2C would equate to $26 \times 2 = 52$ A. When a fully discharged cell is charged at 1C and 2C respectively, it theoretically charges fully in 1 hour and 0.5 hour respectively.
9. *Energy*: The power delivered by a cell at instantaneous C-rates for specified times at corresponding battery voltage is called energy delivered by the battery. It is expressed in watt-hours [Wh] [25]. It is obtained by multiplying discharge power with discharge time.

Below is a brief description on Li-ion batteries mostly dealing with the structure and basics of construction, working principles, different formats commercially available, materials used, methods employed to manufacture format under consideration, among others relevant to the current study.

2.3.2 Construction

Similar to historically available electro-chemical cells, the three sections which are essential for the battery operation are cathode (+ve electrode), electrolyte (charge carrier) and anode (-ve electrode). As the development advanced over decades, based on the construction and applications to specific shapes and sizes, a separator soaked in the electrolyte was installed between cathode and anode to avoid their physical contact and cause short circuits. It is to be noted that an electrolyte is capable of carrying the positively charged ions but not the electrons which are negatively charged. The cathode material is coated onto a +ve metal current collector (typically Al) and the anode material onto a -ve metal current collector (typically Cu). A single unit cell is made up of stacking of these materials in the order as -ve electrode (Cu+anode material) | separator/electrolyte | +ve electrode(Al+cathode material).

It is to be observed and noted from Figure 2.12 that anode, separator and cathode materials are porous with electrolyte in the crevices. There are several additives and binders added to the electrode materials which enhance specific properties like working temperature range, resistance to degradation, high C rate tolerance among several others. These additives are trade secrets that are specific to the manufacturers and no mention of these materials is given in the manufacturer data-sheet. There are several unit cells repetitively arranged next to each other to make one battery cell. Cu current collectors from each of the unit cell is projected at the top and welded, attached to a relatively thicker Cu piece forming the -ve tab. Similarly, Al current collectors are projected and welded to Al piece forming the +ve tab. It is

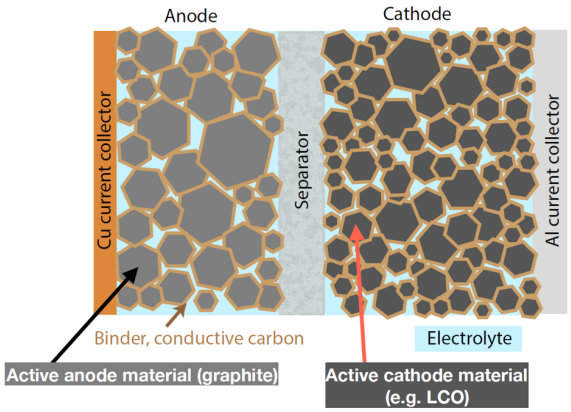

Figure 2.12: Basic electro-chemical unit cell construction [22]

also to be noted that the current collectors are coated on either faces. The current cell under study has 38 [26] unit cells represented by the dotted line in Figure 2.13.

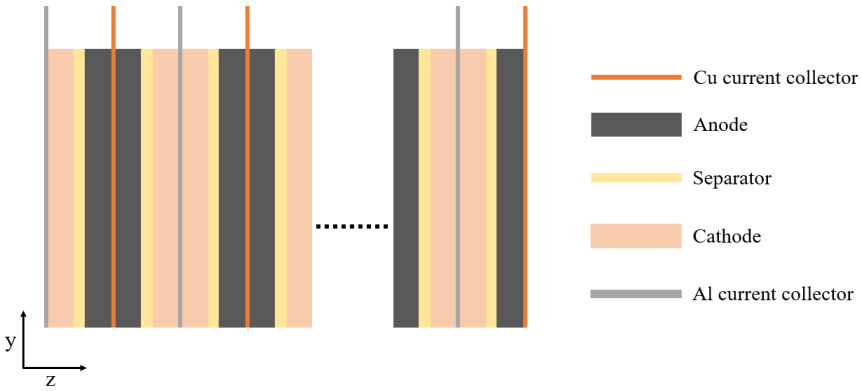

Figure 2.13: Battery cell construction with repeated unit cells

2.3.3 Working Principle

Batteries store electrical energy in the form of chemical energy. It is the chemical reactions that determine the behavior, limitations of these cells. The thermodynamics and kinetics of chemical reactions are the origin for voltage, capacity, power and energy in the cells. Based on the requirement, cells are arranged in series and parallel to obtain suitable voltage and capacity for the required end application. The components of the cell where the characteristic redox reactions take place are called *Active materials* i.e., anode and cathode while the components which are passive during these reactions are *Non-active materials* i.e., current collectors, separator and electrolyte.

Thermodynamics of the active materials used and the absolute temperature when the redox reactions take place determine the voltage level and behavior during charging and discharging. The rate of chemical reactions that affect the rate of energy transformation from chemical energy to electrical energy depend on the mass transport and diffusion in active and non-active materials used [27]. The individual

thermodynamic properties of electrodes determine the theoretical cell voltage E_{cell} of the cell, which is also called electromotive force (emf). The driving force for redox reactions is expressed as Gibb's free energy ΔG_{cell} [27].

$$\Delta G_{cell} = -nFE_{cell} \tag{2.25}$$

where, n = number of electrons transferred, F = Faraday constant (96485 As/mol) and E_{cell} is difference between electrode potentials [27].

$$E_{cell} = E_{positive} - E_{negative} \tag{2.26}$$

For a cell to undergo continuous discharge, ΔG_{cell} needs to be negative. As seen from (2.25), this is only possible when E_{cell} is positive. The cells which can only act as sources converting chemical energy to electrical energy are called galvanic cells and are considered as *Primary cells*. But, the cells which can convert electrical energy to chemical energy are called electrolytic cells. Cells that exhibit both behaviors as galvanic and electrolytic cells are considered as *Secondary cells*. Hence, the Li-ion cells which are under consideration here are Secondary cells as they need to be recharged regularly for EV operation.

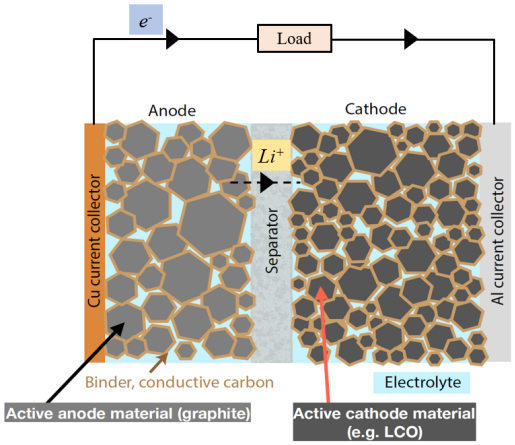

Figure 2.14: Illustration of charge movement during a cell discharge [27]

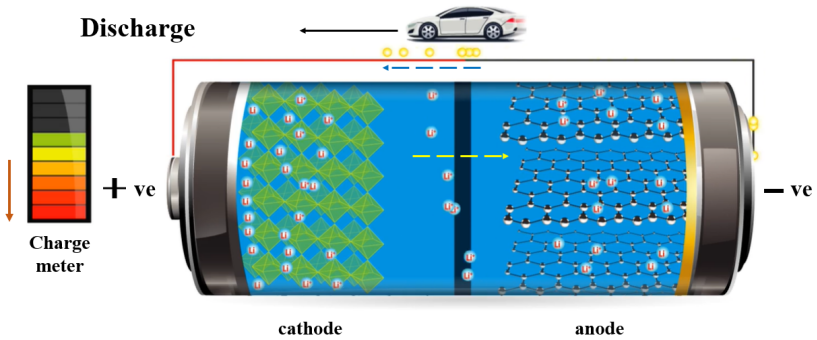

Figure 2.15: Discharge animation of a Li-ion battery illustrating transfer of +ve and -ve charges [28]

During discharge, ΔG_{cell} drives the e^- from the anode to the cathode through the external load and Li^+ ions travel through the electrolyte/separator to maintain charge balance. However, all the Li^+ ions are not extracted out of the cathode since it otherwise would cause irreversible damage to its micro-structure and result in excessive degradation which is specified as the cutoff voltage with some safety margin by the manufacturers. Hence, the electrode materials used play a major role in cell performance over its lifetime [27]. Figure 2.14 and Figure 2.15 depict the charge movement during discharge.

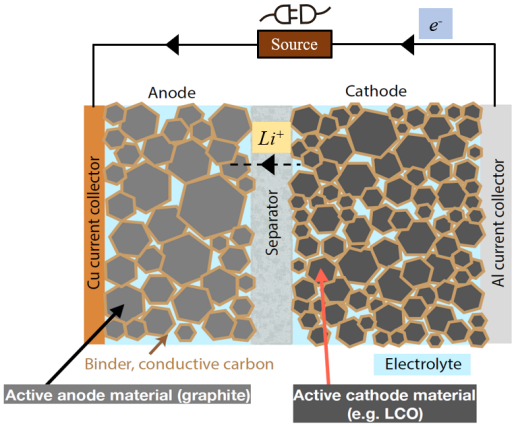

Figure 2.16: Illustration of charge movement during a cell charge [27]

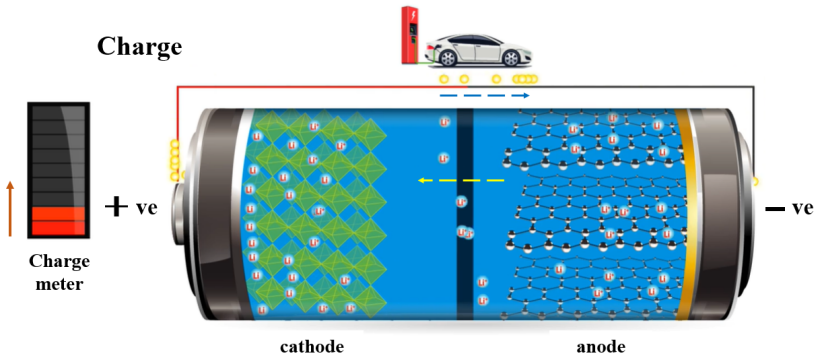

Figure 2.17: Charging animation of a Li-ion battery illustrating transfer of +ve and -ve charges [28]

After the cell is discharged, i.e., the cutoff voltage is reached, the specified concentration of Li^+ ions is reached in the anode and further discharge could cause irreversible damage to the material structure. Figure 2.16 and Figure 2.17 depict the charge movement during charging. An external emf which is applied to reverse the redox reactions and drive the e^- back from cathode to the anode while inducing Li^+ ion transport from the cathode to the anode is considered as an external source [27]. The process of removal of Li^+ ions from an electrode micro-structure is called *Delithiation* whereas addition of Li^+ ions into an electrode micro-structure is called *Lithiation*. These terms are extensively used in battery cell research.

2.3.4 Multi-physical Component

A Li-ion cell is a complicated device with multiple-physical principles and laws working simultaneously during normal operation. The chemical reactions are providing electrons, electrical connections are forming a path for their travel, heat is generated/absorbed during chemical reactions, electron flow and the external mechanical pressure is acting based on the cell's application area.

2.3.4.1 Chemical

Analogous to a traditional Pb-acid battery, a Li-ion battery also operates based on the potential difference between 2 electrodes, namely Cathode and Anode. Gibb's energy is the driver which forms the basis for operation. The anode (-ve electrode), which is typically made of porous lithiated graphite, is where the e^- and Li^+ ions are separated. Due to the concentration gradient and selective permeability of separator towards Li^+ ions, they travel through to the cathode (+ve electrode) and electrons travel along the external circuit and end up at the cathode to maintain charge balance. The separator and the cathode materials are porous as well and entirely soaked in liquid electrolyte along with the anode.

2.3.4.2 Electrical

The electrons provided by the chemical reactions are what constitute the electrical energy for all the systems within the vehicle. During discharge, electrons flow from the anode to the cathode through the external circuit. This external circuit is where the energy is utilised for vehicle propulsion and other auxiliary functions. As all the electrical systems operate on AC or DC based on the appropriateness, e.g., Propulsion motors (IM or PMSM) use AC, while infotainment or lighting systems use DC. Conventionally, discharge is represented by current flow direction from the positive terminal to the negative (e^- flow from negative to positive terminal) and vice-versa for charging.

2.3.4.3 Thermal

Heat energy is dissipated or absorbed during the chemical reactions leading to electron free-up. Depending on the SoC and temperature of the Li-ion cell, net heat dissipated can be positive (exothermic) or negative (endothermic). This part is accounted for from the chemical reactions in the cell. However, the flow of electricity through the conductors also generates heat and this heat is always positive irrespective of the direction of flow (charging or discharging). This heat is the combination of heat from the e^- flow through anode/electrolyte, anode current collector (Cu), cathode current collector (Al), cathode/electrolyte and Li^+ ion flow through anode/electrolyte, separator/electrolyte, cathode/electrolyte.

2.3.5 Materials and Properties

As mentioned in the previous sections, typically a Li-ion cell is primarily made up of 6 components, namely (1). positive current collector, (2). cathode, (3). separator, (4). anode, (5). negative current collector and (6). electrolyte. Some of the above components have common materials among different cell manufacturers. Generally, the positive current collector is made of Al and the negative current collector is made of Cu [27].

2.3.5.1 Electrolyte and Separator

As the combination of electrodes determine the energy, voltage and cell capacity, the electrolyte used determines the rate at which energy is released or accepted. Hence, it is vital for Li-ion transport between electrodes. Electrolytes are electrically and chemically inert as they do not take part in redox reactions. Most of these are a combination of fluoridated salts and organic solvents with some additives to enhance charge transport characteristics and be sacrificial to temperature increases hence avoiding electrode damage. Typical solvents used are ethers, esters or carbonates like propylene carbonate (PC), ethylene carbonate, dimethyl carbonate (DMC) or a combination of these in specific proportions. The most common salt found in most of the commercial Li-ion batteries is Lithium hexafluorophosphate ($LiPF_6$) which is also used in the current study cell. The solvents used are a combination of EC/DMC/Ethylmethyl Carbonate (EMC)[26].

Separator is a thick porous membrane which separates the electrodes and holds a significant quantity of the electrolyte. It is an electrical insulator and also has poor thermal conductivity. Since it is a polymer, its functionality is dependent on temperature. Though it is desirable to have the separator thickness constant over the cell's lifetime, it's thickness varies as the cell ages. It also acts as a passive safety component. It is tailored to melt and block the path between electrodes entirely with sufficient mechanical strength to avoid short circuit during thermal runaway situations. It's ageing is mainly characterised by blocking of the pores within from solid electrolyte interphase (SEI) particles and hence increase cell impedance. Most of the separators are made up of polypropylene membranes but the choice also varies based on the electrolyte used as they complement mutual functioning.

2.3.5.2 Electrodes

Electrodes are the active materials which are the sources of e^- and Li^+ ions hence forming the primary materials for a cell's voltage source. Anode and cathode are made of different materials and their combination determines the operating voltage, power and energy of the cell. In general, the cathode material is coated onto an Al current collector and together, it is called +ve electrode while the anode material is coated onto a Cu current collector and together is called -ve electrode. Sometimes, anode and -ve electrode are used interchangeably while the same applies to the cathode and +ve electrode. Commercially available Li-ion cells have anode materials as silicated graphite, which is a layered structure with voids to be filled by Li^+ ions. As the cell is discharged, lithiated graphite loses Li^+ ions to the cathode

and its half cell reactions during discharge and charging are as below.
During discharge at the -ve electrode,

$$LiC_6 \rightarrow C_6 + Li^+ + e^- \tag{2.27}$$

During charging at the -ve electrode,

$$C_6 + Li^+ + e^- \rightarrow LiC_6 \tag{2.28}$$

The spectrum and variability of materials available for the cathode are innumerable and new materials are being continuously synthesised as cathode material is currently one of the limiting factors for cell capacity [27]. A different arrangement of Li^+ ions within either layered or spinel ionic compounds containing heavy metals like Mn, Co, Ti and Ni are not uncommon. One of the most common layered materials employed is Lithium cobalt oxide (LCO) and NCA, NMC are two variants of LCO which have a relatively lower amount of Co and is substituted by Ni, Al and Mn with some improvements in capacity, structural and thermal stability. The half cell reactions during discharge and charging are as represented below.
During discharge at the +ve electrode using LCO,

$$xLi^+ + Li_{1-x}CoO_2 + e^- \rightarrow LiCoO_2 \tag{2.29}$$

During charging at the +ve electrode using LCO,

$$LiCoO_2 \rightarrow xLi^+ + Li_{1-x}CoO_2 + e^- \tag{2.30}$$

where, $x = 0.5$ to 0.6

On the other hand, spinel structures have also become common lately which sport high C rate capability and structural stability while compromising on capacity. One example of this is lithium manganese oxide (LMO) which is often mixed with NMC to combine advantages of higher capacity. In the current study, the cathode material is a combination of 30% by weight of spinel LMO and 70% by weight of NMC [26].

2.3.6 Cell Configurations

Li-ion cells come in various shapes and sizes and for different applications, the most suitable ones are chosen with some reasonable trade-offs. The most commonly used formats in automotive applications are cylindrical, prismatic and pouch. Each of these have their own advantages and disadvantages as presented in Table 2.3. Based on the energy and power required for a particular class of vehicle for a certain driving range and acceleration capability, cells are arranged in series and parallel into the battery pack as **ns mp** where n is the no. of cells in series and m is the no. of cells in parallel. The format chosen for each EV application is also dependent on the chassis employed and space available for efficient packaging as it largely determines the battery pack energy and hence range. The format of the cell considered in the present study is a pouch cell and hence the manufacturing methods discussed in the next section exclusively deal with the same. Figure 2.18 represents the most widely available and used Li-ion cell formats.

Table 2.3: Comparison of standard cell formats commercially available [7]

	Small cylindrical	**Large cylindrical**	**Prismatic**	**Pouch**
Shape	Encased in a metal cylinder, usually 65 mm long	Encased in metal or hard plastic cylinder	Encased in semi-hard plastic case	Contained in a soft bag
Connections	Welded Ni or Cu strips or plates	Threaded stud for nut or threaded hole for bolt	Threaded hole for bolt	Tabs that are clamped, welded or soldered
Retention against expansion when fully charged	Inherent from cylindrical shape	Inherent from cylindrical shape	Requires retaining plates at ends of battery	Requires retaining plates at ends of battery
Appropriateness for small projects	Poor: high design effort, requires welding, labor intensive	Good: some design effort	Excellent: little design effort	Very poor: design effort too high
Appropriateness for production runs	Good: welded connections are reliable	Good	Excellent	Good: high performance
Field replacement	Not possible	Possible but not easy	Easy	In general, not possible
Other notes	Best for retrofits, as small shape can be fit in all available space	Not widely available	Best availability, very little design effort required	High energy/power density (by themselves); significant design effort required: only appropriate for large production runs

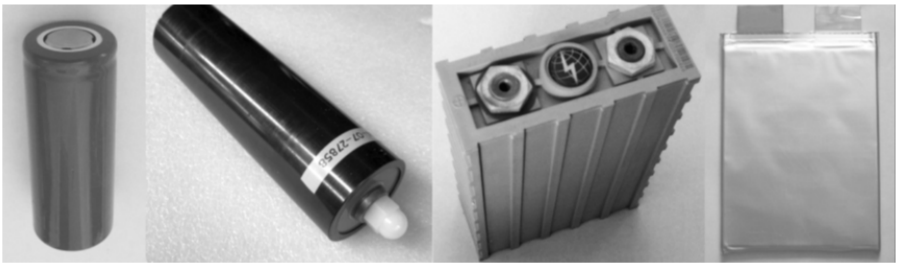

Figure 2.18: Li-ion cell formats: (a). small (left) and large (right) cylindrical cells, (b). Prismatic cell and (c). Pouch cell [7]

2.3.7 Manufacturing Methods

As the cells considered in the study are pouch cells, this section focuses on the manufacturing methods for the same and how different methods can affect cell behavior. There are four methods most widely followed in the battery manufacturing industry, namely,

1. *Single sheet stacking* : In this method, flat sheets of double side coated current collectors, both anode and cathode are assembled alternatively with a separator in between each set of anode and cathode sheets. It is one of the most effective uses of raw materials as no resource is wasted in the lateral direction, i.e., along the thickness that could cause stresses at the foldings, which is the case in other processes as described below. The process is demonstrated in Figure 2.19.
2. *Winding* : Four different rolls of the anode, separator, cathode, separator are wound onto a rotating rectangular block based on the capacity of the cell

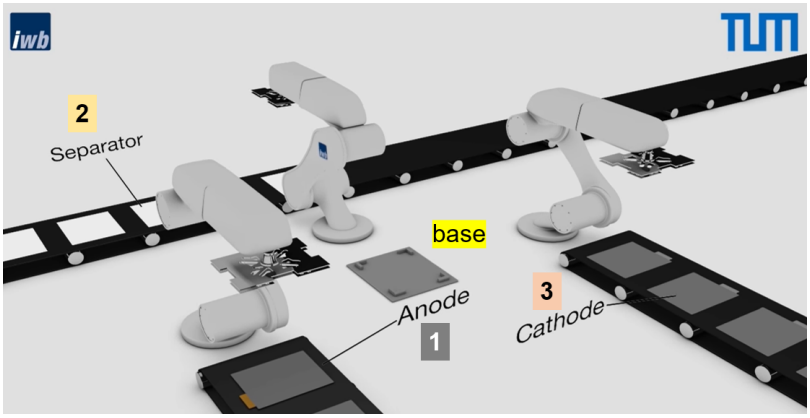

Figure 2.19: Single sheet stacking on the base in order 1,2,3,***2***,1,2,3,***2***,1,2,... [29]

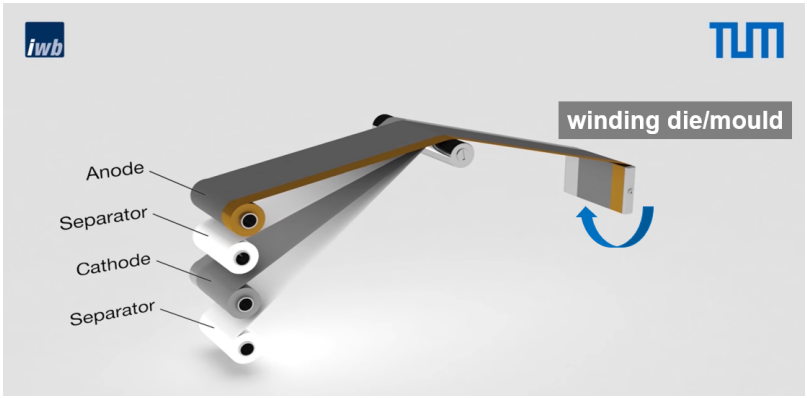

Figure 2.20: Winding of individual layers of the cell [29]

required. After of set number of rotations, the rolls are sliced out and the wound cell is taken off the die and the next cell is rewound. The process is demonstrated in Figure 2.20.

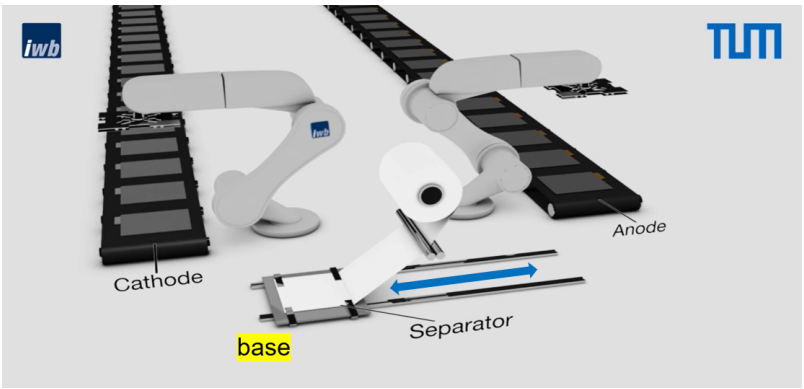

Figure 2.21: Z-folding with single electrodes [29]

3. *Z-folding with a single electrode* : The base on which layers are stacked moves in such a way that every alternate layer is a separator and it extracts separator from the separator roll. At each end, the clipping is done to ensure

even distribution of separator at the folds and separator material exists along the thickness on the lateral face inside the pouch. The cell under study is manufactured by this process. The process is demonstrated in Figure 2.21.

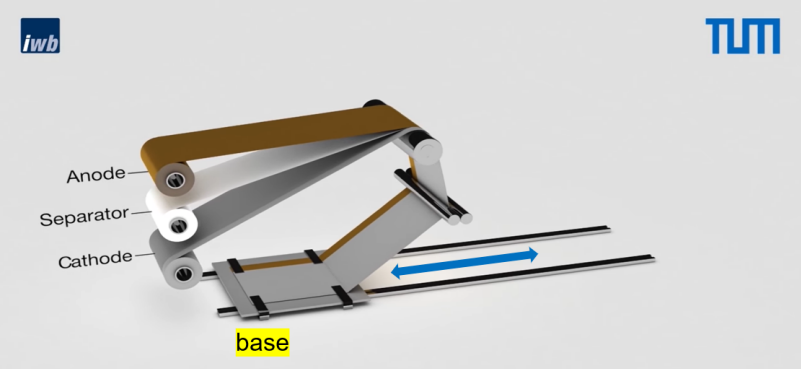

Figure 2.22: Z-folding [29]

4. *Z-folding* : This particular process is partly similar to the previous one except that the active material layers are existing on the lateral side of the assembly and hence cause excess stress at the folding lines leading to uneven expansion and accelerated localised ageing. The process is demonstrated in Figure 2.22.

After stacking a sufficient number of unit cells/layers, the stack is inserted into a pouch and a predefined amount of electrolyte is filled to soak and fill the porous voids of the separator and the electrodes. Then, the projected current collectors are welded and attached to tabs forming +ve and -ve terminals.

2.3.8 Heat Sources

During the battery cell operation which involves either charging or discharging, there are always losses accompanied in the form of heat. After all, a Li-ion cell is an electro-chemical system wherein the electrons made available for operation are a result of chemical reactions rather than free electrons available in high electrical conductivity metals. Battery cells exhibit a peculiar behavior as a combination of a resistor and capacitor. The capacitor accounts for the gradual variations in current with respect to time while the resistor corresponds to the internal resistance leading to heat dissipation.

Here in Figure 2.23, R_{load} is the external load which the battery powers while R_{int} is the internal resistance of the cell, which is a cause for the heat losses. OCV is the open circuit voltage of the cell and V_{cell} is the terminal voltage while I is the current. I is negative when the battery is being discharged and positive when it is charged. R_{int} is largely dependent on the temperature of the cell. However, the dependence on its SoC is more pronounced at a lower SoC window [30] and for the sake of reducing complexity, it is ignored in the current study. This is also justified by using the cell at higher SoC windows in the simulations.

As described before, the capacitors C_1 and C_2 account for the dynamic behavior of the cell. However, the combined effect of R_0, R_1 and R_2 in Figure 2.24 equates

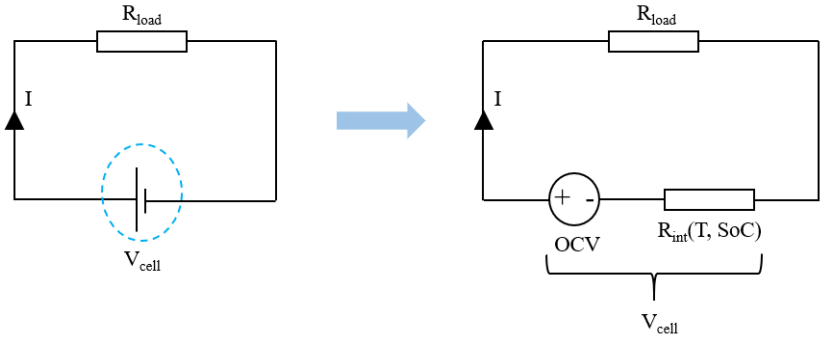

Figure 2.23: Cell representation in a simple circuit with $V_{cell} = OCV - IR_{int}$

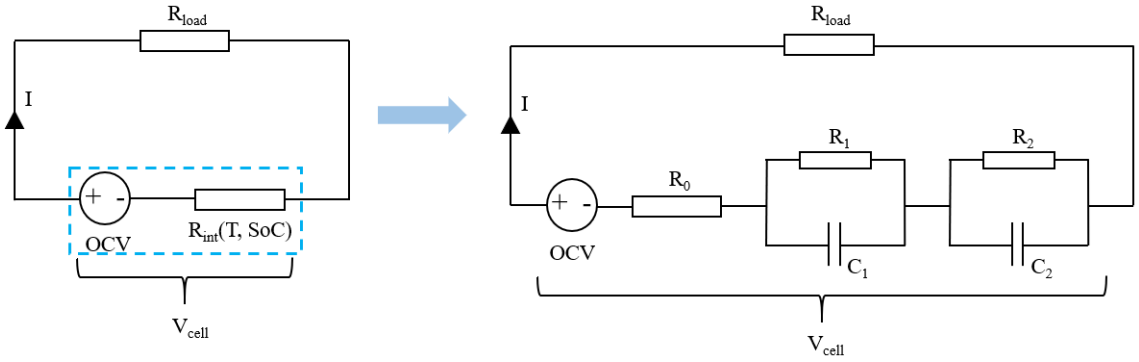

Figure 2.24: Cell representation with a 2-RC circuit in a simple electric load application

to R_{int}.

The heat generated during normal operation is subdivided into Joule heat (irreversible heat) and Entropic heat (reversible heat). Joule heat is the loss proportional to the square of current flow I^2R_{int} while entropic heat is related to the characteristics of chemical reactions which is dependent on the entropy coefficient and is characteristic of each cell. The entropic heat coefficient can be positive or negative based on the SoC, hence representing exothermic (heat releasing) or endothermic (heat absorbing) behavior. Hence the total heat dissipated from the cell is the algebraic sum of reversible and irreversible heat. The irreversible heat generated is by the internal resistance of the cell which is accounted to the individual resistances of current collectors, electrode materials, separator and electrolyte.
The total heat generated from the cell is given by,

$$Q_{total} = Q_{irr} + Q_{rev} \tag{2.31}$$

where, Q_{irr} is irreversible heat and Q_{rev} is reversible heat.

$$Q_{irr} = I^2 R_{int} \tag{2.32}$$

$$Q_{rev} = IT\frac{dU_{OCV}}{dT} \tag{2.33}$$

where, T is the absolute temperature of the cell in kelvin and $\frac{dU_{OCV}}{dT}$ is the entropic heat coefficient whose variation with SoC is shown in Figure 2.25. Hence, from (2.31),

$$Q_{total} = I^2 R_{int} + IT\frac{dU_{OCV}}{dT} \tag{2.34}$$

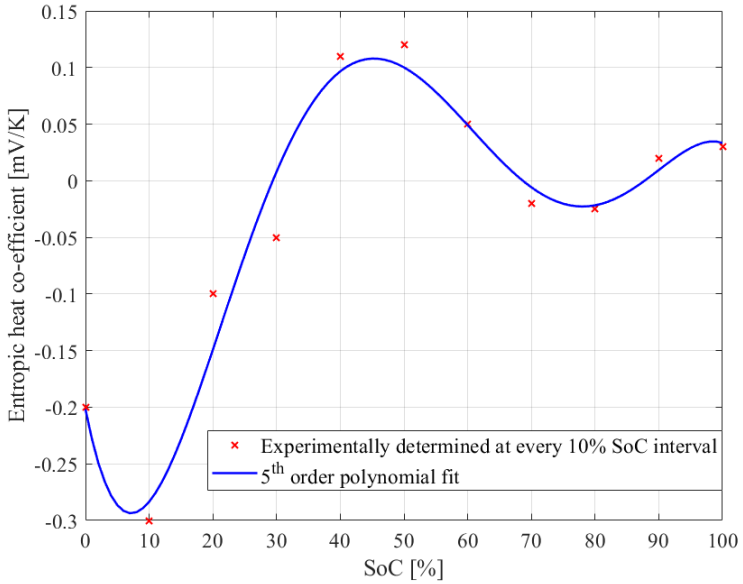

Figure 2.25: Variation of entropic heat coefficient with SoC

2.3.9 Temperature Effects and Regulation

The Li-ion cell performance varies significantly as a function of temperature. Though a fairly high temperature is ideal to reduce the resistance during the cell operation, maintaining the limit is also equally crucial since the side reactions deteriorate the compounds in the cell, especially the active materials. Even the polymer is selected so that at higher temperatures, it completely blocks the flow of ions through it and avoids short-circuiting of the anode and the cathode, reassuring safety against fire in a BEV. Figure 2.26 depicts some instances of EV fires which has made certain customers reluctant to switch to an EV.

Unlike fossil fuels which need oxygen to ignite, Li-ion batteries contain oxygen as one of the elements in compounds used as cathode and electrolytes in different proportions. Hence, it is relatively easier to ignite batteries than fossil fuels in closed spaces with no gaseous oxygen. As the powertrain system extracts from highly energy-dense sources (in this case, batteries) in a controlled manner, the effect of a sudden high temperature pulse would be challenging to comprehend immediately, especially in long term usage.

Extreme temperatures not only have an effect on the safety aspect but also on the overall performance of the EV. The parameters described in section 2.3.1 have the varying effect of temperature and the effects are briefly explained.

Figure 2.26: Some instances of EV fires reported by NTSB [31]

- *Capacity*: Based on the chemistries used, batteries have different optimum temperature windows, which can extract maximum capacity. However, during normal operation, heat is generated from the reactions and hence the temperature increases. In general, for cells used in automotive applications, cells have a larger charge capacity above 30 °C than discharge capacity and it is vice-versa below 30 °C [32]. However, when batteries are stored or operated at higher temperatures (above 50 °C) [33], the recoverable capacity reduces significantly [34]. A significant reduction of capacity can also be observed if repeatedly operated below the temperature of −10 °C [34]. Hence, the operating temperature defines the extent of electrical energy that can be extracted but also constrains based on lower and upper temperature limits to avoid damage to the battery.
- *Internal resistance*: As the chemical resistance cannot be accurately quantified into electrical resistance from theory, cells are tested after assembly and a quantification of specific vital parameters relevant to the design of the power system are carried out. As the manufacturers specify the internal impedance of the battery at high frequencies, it involves the resistance contribution from the current collectors, the active materials, separator, contact resistances between and within repetitive unit cells in a single cell [35]. For the metal current collectors as defined by physics, the electrical conductivity decreases as there is an increase in temperature because of constraint to the mobility of electrons. It is defined by the temperature coefficient of the metal which is material specific [36]. Figure 2.27 presents the electrical conductivity (in mega Siemens per meter) variation of Cu and Al over most of the EVs battery operating temperature range.

$$\sigma_{T_1} = \sigma_{T_0}[1 + \alpha(T_1 - T_0)] \tag{2.35}$$

where, σ_{T_1} - conductivity at desired temperature T_1 in S/m

σ_{T_0} - conductivity at reference temperature 273 K in S/m
α - temperature coefficient of the metal in /°C or /K
for Cu, α is 0.0040 /K and σ_{T_0} is from [36]
for Al, α is 0.0043 /K and σ_{T_0} is from [36].

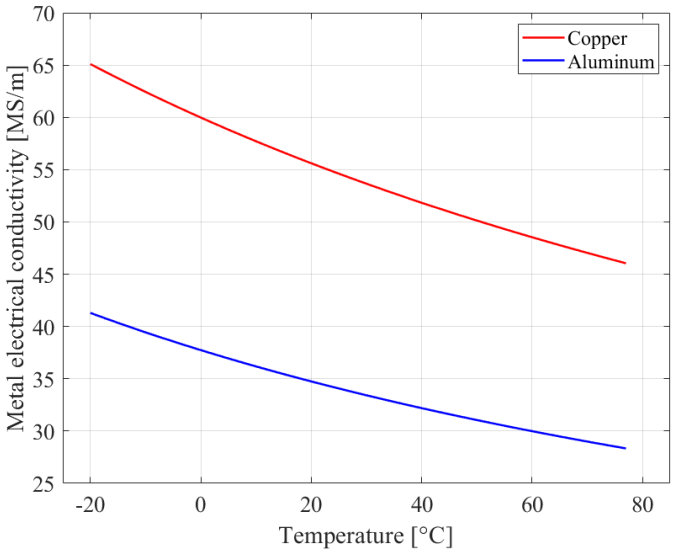

Figure 2.27: Variation of electrical conductivities of Aluminum and Copper which are used as current collectors

In contrast, the conductivity of active materials, i.e., the rate of reaction, which defines the chemical resistance equated to electrical resistance, improves with an increase in temperature. It is evident from the laws of physical chemistry where the rate of a chemical reaction is proportional to the absolute temperature of the chemical system. More discussion about the same for the current cell under study is described in chapter 3.

As the remaining parameters in section 2.3.1 are mostly dependent on capacity and internal resistance, their variations based on temperatures are co-related from the same.

2.4 Thermal Management System

As the basic principles of physics apply to energy conversion in vehicles, a certain amount of energy is evidently lost as heat. In ICEVs, an ICE has up to a maximum of 45% [37] energy conversion efficiency and most of the energy is lost as heat as an ICE work on thermodynamic principles. Hence, as the powertrain developments progressed for different classes of vehicles, more and more sophisticated thermal management systems (TMS) evolved. With the transition into HEVs and BEVs, relatively complicated systems were augmented.

While keeping the fundamental vehicular systems under moderate operating temperatures, passenger comfort with air conditioning system came into the picture during mid 1930s [38]. Though it was retrofitted initially, manufacturers began offering

models with A/C and an additional TMS was to be assembled along with the primary system. Eventually, with further optimizations, systems with comprehensive control transitioned on to the roads.

2.4.1 Types

As A/C became more common in passenger vehicles, TMS with two separate circuits became standard in vehicle architectures. One with Radiators which uses liquid coolant, another with phase change material like the refrigerant **R1234yf** which operates based on the Vapour-compression refrigeration cycle (VCR). The latter is the working principle employed in A/C. Almost all the vehicles these days employ either of the above or their combination to manage heat in the powertrain and the passenger cabin.

Since the current study is exclusively dealing with TMS of powertrain, the same will be kept as the focus for the theory below and TMS for passenger comfort is omitted. Based on the target temperature range for sections of the powertrain, namely, EM, power electronics, inverter and battery pack, TMS primarily consists of,

1. *Radiator cooling circuit*: It is one of the simplest cooling solutions in an automobile. The heat source, which in the present case is an EM (IM or PMSM) has a cooling jacket surrounding it that is in contact with crucial areas of excess heat loss in the EM. The coolant continuously flows through the jacket and absorbs heat and flows through the radiator, which has a very large surface area with fins [39]. This hot coolant flows through the fins and due to vehicle motion, surrounding ambient air flows over the fins. Heat exchange occurs across the fins and hence the coolant is cooled by fast flowing ambient air. There is also a surge tank available which supplies extra coolant when there is a pressure drop in the system. A pump induces the flow of coolant and is regulated by a closed-loop controller actuating based on set temperature targets. The coolant typically used consists of a mixture of water and anti-freeze agents like ethylene glycol in pre-defined proportions [40]. One of the main limiting factors of a radiator circuit is its effectiveness. It cannot cool the coolant to a temperature below the ambient.
2. *A/C circuit*: The ineffectiveness of radiator cooling is addressed by A/C (refrigeration) cooling circuit. Due to the negative effects on the ozone layer from the use of traditional refrigerants, a new refrigerant **R1234yf** is currently being employed in automotive applications [39]. The refrigeration circuit consists of a compressor, condenser, receiver/dryer, Thermal Expansion Valve (TXV) and Evaporator as main elements along with support elements like accumulator and service ports. During normal operation, the gaseous refrigerant at low pressure and a low temperature enters the compressor where it is converted into a high temperature, high-pressure gas. This gas flows through a condenser where the gaseous refrigerant exchanges heat with the ambient and is converted into high temperature, high-pressure liquid. Then from the discharge side of the condenser, the refrigerant is filtered off the moisture and contaminants in the receiver/dryer. The filtered refrigerant at high temperature, high

pressure passes through the TXV which converts it into a low-pressure liquid which flows through the evaporator where it boils by absorbing heat from the source (EM/Battery) and gets converted to a low-pressure gas. Then it passes through a low service port into the condenser for the next cycle [40].

2.4.2 Suitability in Different Vehicle Configurations

Though the A/C circuit seems to be a better choice for heat regulation over wider temperature ranges, it also demands more energy to operate when compared to the radiator circuit. Considering the systems only relevant to powertrain cooling, a radiator circuit would be a viable choice for an ICEV based on effectiveness and economy. However, EVs have batteries which are highly temperature sensitive. Hence, choosing an A/C circuit could be more plausible, but utilising a slightly over sized compressor to cool the battery pack along with EM would lead to system inefficiencies. This could hurt the viability of the relatively lower driving range EVs which compete against longer range, fast refuelable ICEVs. As a result, a combination of the above circuits is utilised in EVs to maintain higher system efficiency while ensuring temperature ranges for battery safety, performance requirements and the same is considered from [39]. A radiator is used to cool the EM while an A/C circuit manages heat dissipated from the battery pack. Figure 2.28 shows the cooling circuit layout of a battery pack and inverter which are cooled by both, a chiller (A/C circuit) and a radiator.

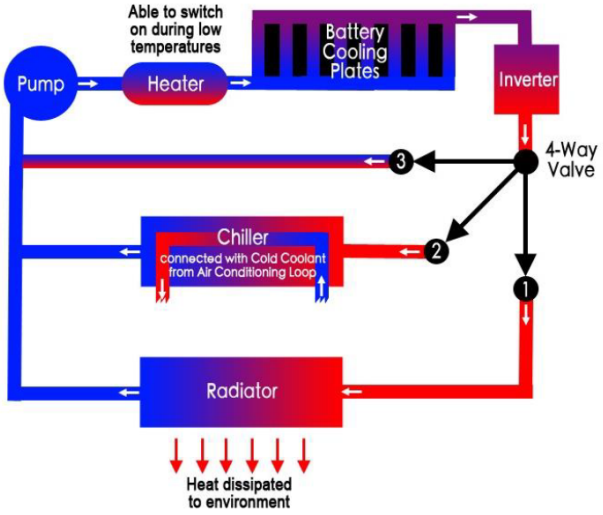

Figure 2.28: Combination of a radiator and A/C cooling circuit with heater for warming the battery during low ambient conditions [41]

2.5 Modeling Methods

Over the course of improvements in computing power, analytical calculations have moved over to more sophisticated methods which can be solved in seconds based on the level of complexity. Some of the most common methods followed in the industries around the world include the Finite Element method (FEM), Finite Difference Method (FDM) and Finite Volume Methods (FVM). While for simpler solid geometrical objects, all the above methods give similar results, the situation turns tricky when the geometries and the physics involved change and some methods appear to have the upper hand over the other based on accuracy, computation time and resource availability. Generally, FEM is used for solids and FVM for simulations involving fluids.

Table 2.4: Comparing advantages and disadvantages of FEM, FDM and FVM [42]

Method	Advantages	Disadvantages
FEM	1. More mathematics involved 2. Natural boundary conditions (for fluxes) 3. Master element formulation 4. Any shaped geometry can be modeled with the same effort	1. More mathematics involved - less physical significance
FDM and FVM	1. Fluxes have more physical significance	1. Irregular geometries require far more effort

2.5.1 FEM, FDM and FVM

All the above methods are solved on the basis of partial differential equations (PDE). As PDE are converted to algebraic equations to be solved by the processors, this conversion/discretization is done using one of these methods.

In FEM, the CAD model/geometry is subdivided into small finite-sized elements with similar geometrical shapes whose collection constitute the finite element mesh. The PDE are used to represent the physics and interaction between each element with the adjoining ones. After assembling all the PDE and converting into algebraic matrices, which are solved by available matrix solvers [43]. However, the type of solver is dependent on the physics involved as each physics has a specific imprint on each matrix. Hence, this condition is exploited by tailored numerical methods. Due to the extensiveness of applications and the possibility to utilise a multi-physics approach, the present study uses FEM in COMSOL-Multiphysics®.

FDM is a relatively direct method to discretize PDE. An arbitrary point considered in the continuum is replaced with discrete equations called finite difference equations. It is defined for a regular grid and hence can provide efficient solution methods. Nevertheless, this method is not often used for irregular CAD geometries rather rectangular or regular block-shaped objects [43].

FVM is similar to FEM in that the CAD model is divided into similar shaped smaller elements. However, it is different in other aspects, starting from the concept of elements which are referred to as cells. FVM is based on the fact of conservation laws in physics, which means the quantity going into a wall of a finite cell leaves

through one or several other walls. From this, one ends up with flux conservation equations averaged over finite cell boundaries. This method is widely used for computational fluid dynamics and electromagnetic simulations [43].

2.6 Vehicle Mechanics

The intended vehicle motion is due to the tractive force (F_t) exerted by the wheels on ground/road surface. This force is produced by the prime mover (ICE or EM) through complex electromechanical systems linking the prime mover to the wheels. F_t has to overcome the resistive forces when moving on a particular terrain [39]. The longitudinal dynamics of a vehicle with mass m_v moving at speed as function of time t as v is given by,

$$m_v \frac{dv}{dt} = F_t - (F_d + F_r + F_g) \tag{2.36}$$

where, F_d is the aerodynamic drag force, F_r is the rolling resistance between wheels and the ground and F_g is the gradient force, as presented in Figure 2.29.
The tractive power (P_t) for a vehicle to move at speed v is given by,

$$P_t = F_t v \tag{2.37}$$

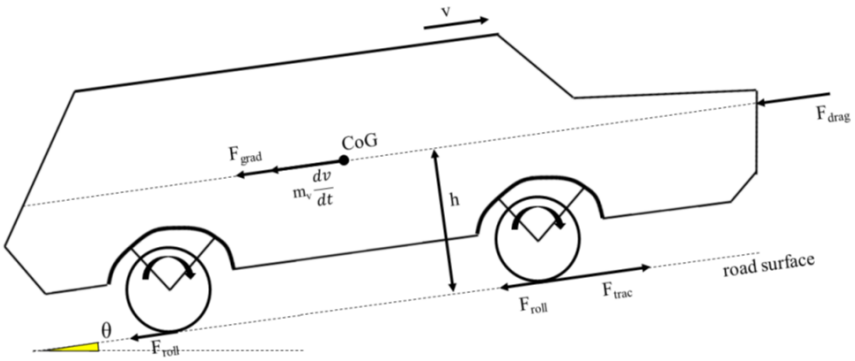

Figure 2.29: Free body diagram illustrating forces acting on a vehicle moving on a non-horizontal surface at an angle θ [39]

The aerodynamic drag force F_d is dependent on the frontal area A_f of the vehicle, the density ρ of the ambient air, the drag coefficient c_d and the relative speed v of the vehicle. In the current case, the surrounding air's speed is neglected. Hence, the vehicle speed becomes the relative speed [39]. F_d is computed as,

$$F_d = \frac{1}{2} \rho \, c_d \, A_f \, v^2 \tag{2.38}$$

The rolling resistance F_r is the resistance experienced by the body which is rolling on a surface. In the case of vehicles, rolling bodies are the wheels. It mainly depends on the vehicle mass m_v, coefficient of rolling resistance c_r and acceleration due to gravity g. Though c_r is dependent on the vehicle speed and tyre pressure, it does

not vary significantly within operating speeds of a typical road vehicle; Hence, its dependence is neglected. c_r is also proportional to $1/\sqrt{p}$, where p is tyre pressure. For the sake of simplicity, this influence is neglected as well [39]. F_r is given by,

$$F_r = c_r m_v g \tag{2.39}$$

When the vehicle is moving uphill, it experiences a resistance due to its own weight and hence, a higher amount of tractive force is required to maintain the same speed as on a flat road. On the other hand, when moving downhill, the gravity-induced force due to the vehicle's own weight acts in the downhill direction and the net force acting in the direction of vehicle motion increases [39]. Considering the road angle to be θ, acceleration due to gravity as g, F_g is calculated as,

$$F_g = m_v g \sin(\theta) \tag{2.40}$$

3

Methodology

The procedure followed to simulate and obtain results was iterative in nature where a simplified model was created with some reasonable assumptions. With considerably plausible results, the procedure was further refined and assumptions were dropped one by one with proper justification to ascertain a close real-world design problem.

3.1 Critical Considerations

Some of the prominent factors which affect the modeling and results need to be quantified and accounted for before proceeding. Below are the factors playing a significant role in the current study and are justified accordingly.

3.1.1 Multiphysics Approach

In the present study, the effect of mechanical stresses due to expansion, contraction of a pouch cell during charging and discharging is ignored. Figure 3.1 shows the interdependence of physics' involved and omission of mechanical contributions. A separate 1-D electro-chemical model developed as part of a more elaborate research work from *Wikner et al* [26] is also used and a separate 3-D electro-thermal model is developed while taking some critical temperature-dependent inputs from the aforementioned work.

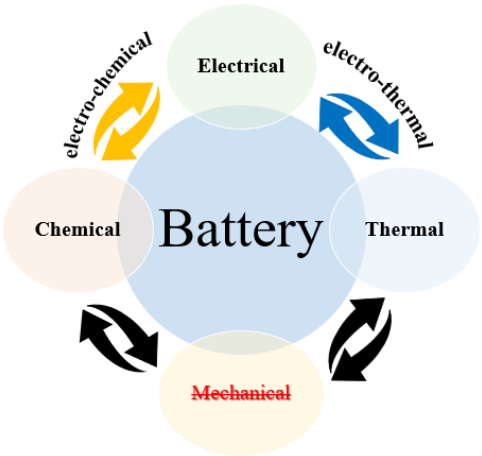

Figure 3.1: Battery modeling methodology with interdependent physics while ignoring mechanical stresses

3.1.2 Contact Resistances

As a Li-ion cell is an assembly of different layered materials, the physical contact between them also plays a considerable part in the determination of heat distribution through the volume of the cell. Since the unknowns in specifying the parameters for the contact interfaces for both electrical and thermal are relatively complicated to quantify and assume, no effect of the same is reasonably justified by accepting perfect contact between the interfaces while still ensuring overall electrical resistance and thermal capacity. Material properties of the anode and cathode and the coatings, electrolytes used are considered as industry secrets for each manufacturer, unless tested and permitted to be used by researchers, it would be a violation of the privacy of competencies in the development divisions within a manufacturer.

3.1.3 3.1.2 Drive Cycle

In the present work, the class 3 WLTC is chosen to assess the performance of the vehicle [39]. The class 3 WLTC consists of four zones which represent urban driving, suburban driving, extra-urban driving and highway driving. The total distance of the cycle is 23.262 km, the duration of cycle is 1800 s and the average speed is 46.5 km/h. The vehicle speed variation with respect to time for the class 3 WLTC is shown in Figure 3.2.

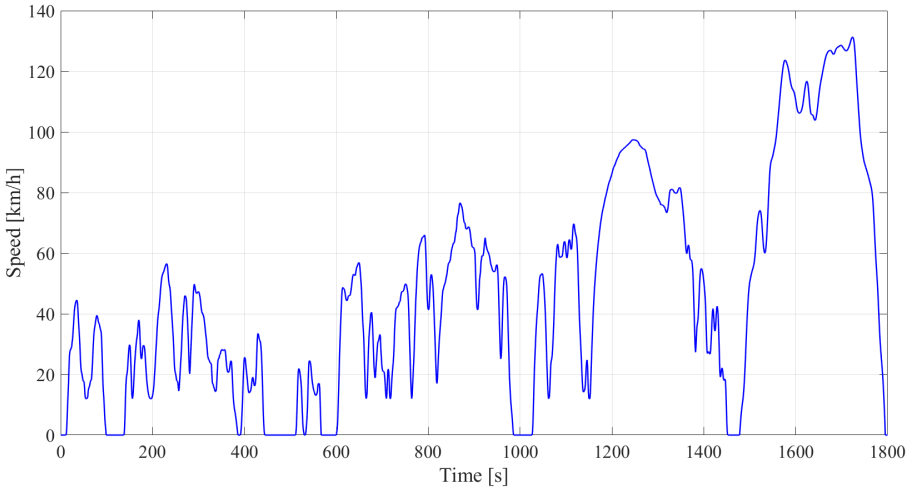

Figure 3.2: class 3 WLTC speed profile

3.1.4 Vehicle Parameters and Cell Specifications

The vehicle parameters which define the Power delivery, acceleration capability, top speed, gradeability and driving range are as given in Table 3.1. Section 2.6 described their use in computations which follow in subsequent sections. Table 3.2 provides the quantified electrical and physical cell parameters, which are typical specifications available from respective cell suppliers. The given parameters are specific to the cell under study.

Table 3.1: Chosen vehicle parameters similar to a modern sedan like Polestar 2, Tesla Model 3 as considered in [39]

Parameter	Variable	Value
Vehicle mass	m_v	1726 kg
Drag co-efficient	c_d	0.23
Frontal area	A_f	2.33 m^2
Rolling resistance	c_r	0.01
Air density	ρ	1.2 kg/m^3

Table 3.2: Reference cell specifications along with operating parameters of the cell under study [44]

Capacity	26 Ah
Maximum charge voltage	4.15 V
Discharge cut-off voltage	2.8 V
Internal impedance	3 mΩ
Dimension (width x height x thickness)	150 mm x 200 mm x 7.5 mm

3.1.5 Cell Sub-Component Material Properties

The sub-components which are used in an entire functioning cell constitute of both metallic, organic and inorganic compounds with a varying magnitude of isotropic and anisotropic properties. Even the pouch used has three constituent layers with their respective share of parameters affecting cell performance in one or the other way. Table 3.3 specifies the materials used in the pouch and equivalent material properties computed in section 3.2.4.1. Table 3.4 presents the sub-component material properties and also the simplified equivalent material properties of lumped active material modeled in section 3.2.4.2. Justifications for these equivalent material considerations follow as below.

Table 3.3: Three layered pouch material properties and its equivalent used in simulations for faster processing [45]

Parameter	Polypropylene (Inner layer)	Al (Middle layer)	Polyamide (Outer layer)	Pouch equivalent
thickness (μm)	288.475	147.5156	88.5094	524.5
density (kg/m^3)	900	2700	1150	1450
specific heat capacity ($J/kg \cdot K$)	1883	900	1100	1262.7
thermal conductivity ($W/m \cdot K$)	0.16	238	0.245	$k_x = k_y =$ 67.0668 $k_z =$ 0.2423
electrical conductivity (S/m)	10^{-6}	3.774×10^7	10^{-6}	10^{-6}

Lumped material - as the individual material properties of anode, separator, cathode and electrolyte are industry secrets and due to additives added, an reasonably accurate approximation cannot be made for the same. Hence, based on proven

Table 3.4: Sub-component parameters of the cell under study [26]

Parameter	Cu current collector	Anode	Separator	Cathode	Al current collector
thickness (μm)	10	64.5	16	74	20
density (kg/m^3)	8700	2304			2700
specific heat capacity (J/kg $\cdot$ K)	385	1120.5			900
thermal conductivity (W/m $\cdot$ K)	400	$k_x = k_y$ =11.051; k_z =1.512			238
electrical conductivity (S/m)	5.998×10^7 at 0 °C	$\sigma_x = \sigma_y = 100$; $\sigma_z = 0.048$ *at* 20 °C			3.774×10^7 at 0 °C

experimental tests and known quantification of the cell, anode, separator, cathode and electrolyte are combined and made into a single material called lumped active material and its equivalent parameters are approximated by the weighted average method and experimental measurements as described in further chapters.

Pouch material - since no specific study of the pouch was found in [26] just as its unavailability in the data- sheet, a similar research article was referred. In [46] the pouch materials used and thickness of individual layers is specified, but the thickness is not the same as of the cell under study. Hence, a proportional increase was made and an equivalent pouch material with matching properties [45] was used with more description of calculations in the subsequent sections.

3.2 Modeling and Simulation : Li-ion Cell

Modeling of a Li-ion pouch cell is one of the primary objectives of this thesis work. Hence, a comprehensive procedure was followed while modeling with a detailed parametrization of the variables. All of the geometric and material parameters are from Table 3.4. This section is divided into the modeling of a unit cell which on repetitive arrangement form a single pouch cell. Then it is scaled to an entire pouch cell with pouch materials and tabs. To reduce the complexity and computational time, a preliminary analysis to merge the active materials (cathode, separator, anode and electrolyte) is made as well.

3.2.1 Unit Cell

When compared to an entire pouch cell, a unit cell is the basic building block. A repetitive arrangement of unit cells forms the operational unit of the cell. Then, this operational unit with current collector projections will have low temperature weld forming the +ve and -ve tabs. Then the entire assembly is inserted in a pouch/bag and the air is vacuumed out before sealing the open side.

3.2.1.1 Layered Unit Cell

A real unit cell as shown in Figure 3.3 consists of a double-coated Al current collector (cathode), separator, a double-coated Cu current collector (anode). A model with all the layers in an unit cell is built accordingly. All the layers in a unit cell have similar height ($H = 200\ mm$) and width ($W = 150\ mm$) but different thicknesses as given in Table 3.4. Since each of the current collectors are shared between two unit cells, a single unit cell model houses half the thickness of current collectors ($t_{Cu} = \frac{10}{2} = 5\,\mu$m) and ($t_{Al} = \frac{20}{2} = 10\,\mu$m). It is also to be noted that the current collectors have projections on top for connection to the tabs for assembly which however will be illustrated in subsequent sections involving full cell modeling.

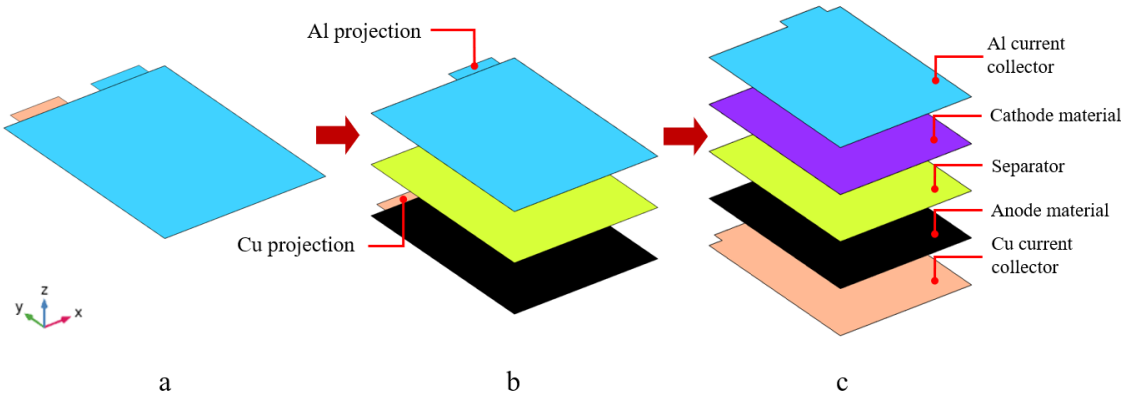

Figure 3.3: (a). Isometric view of an unit cell. (b). Exploded view with anode and cathode material coatings on Cu and Al current collectors respectively & (c). Indication of individual layers with separated anode and cathode materials

3.2.1.2 Lumped Unit Cell

The unit cell model where in all the constituent layers are modeled without merging to make an equivalent layer is called the layered model. As can be observed from the Figure 3.3, each unit cell has five constituents (layers) and an accurate knowledge/data of each layer, especially cathode, separator and anode is relatively difficult to find from literature or manufacturer due to confidentiality of recipes. It is also to be noted that a single unit cell has three layers along with shared current collectors. Hence, in a full cell with 38 unit cells as in this study for the reference cell, the total number of layers sum up as below.

$$N_{total} = 38 \times (n_{cathode} + n_{separator} + n_{anode}) \; + \; n_{Cu\ collectors} + n_{Al\ collectors} \tag{3.1}$$

$$N_{total} = 38 \times (1 + 1 + 1) + 20 + 18 = 152 \tag{3.2}$$

The number of Cu and Al current collectors are 20 & 18 respectively as anode and cathode materials are coated on either sides. From the preliminary analysis, this accounted for excessive computational power and memory requirement along with redundant meshes. As the relevant material properties of the cathode, separator and anode are of same order it was decided to merge the central parts of unit cells into a single **lumped active material** with the equivalent properties based on weighted average methods and calibration from experimental tests and available literature. Figure 3.4 represents the arrangement of the constituents in the lumped unit cell.

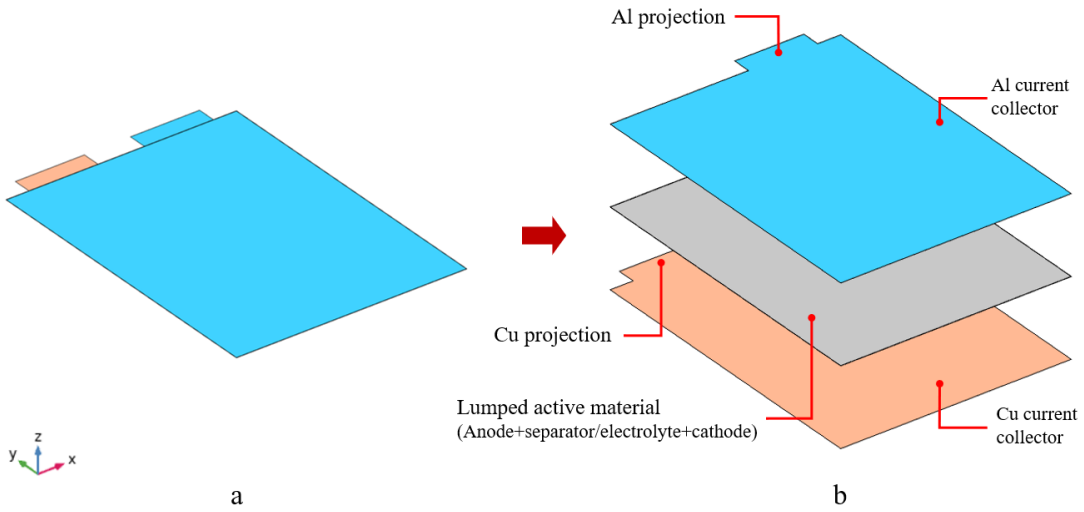

Figure 3.4: (a). Isometric view of a lumped unit cell. (b). Exploded view with the lumped active material between current collectors

3.2.2 Set-up for Preliminary Analysis

Since the determination of temperature distribution within cell volume was of primary importance in the present work, a set of preliminary models were created for the initial analysis. This was done in order to compare the variations in internal temperature distribution between the layered cell which considered all the actual constituent layers and the lumped cell which considered an equivalent lumped material for the cathode, separator and the anode. As the models in this particular section are purely thermal, the relevant material properties are density, specific heat capacity and thermal conductivity.

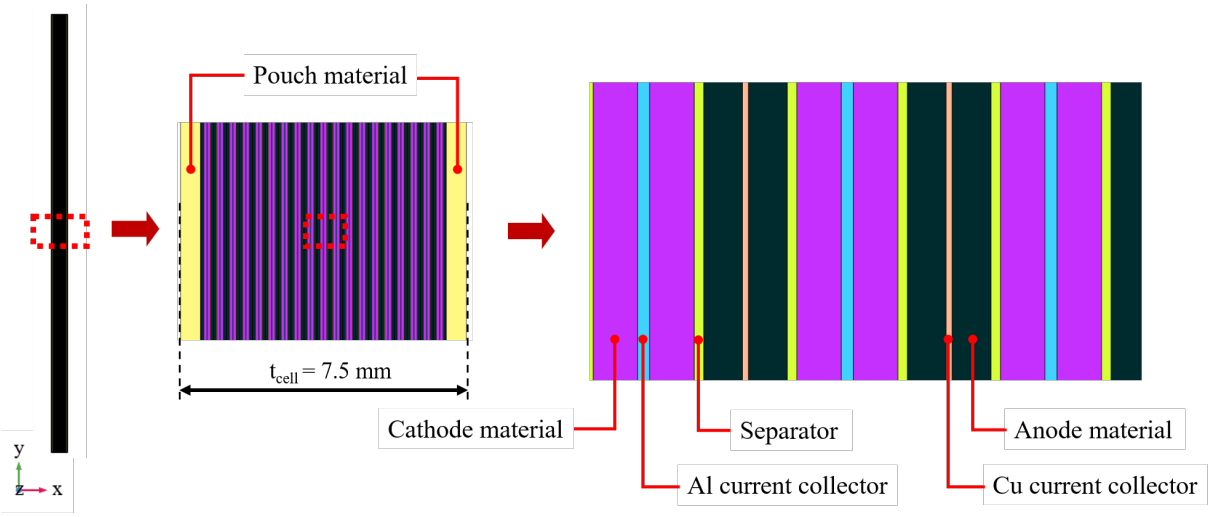

Figure 3.5: 2-D view of layered thermal model with all constituent layers and cell height of 200 mm

3.2.2.1 Layered Thermal Model

A 2-D thermal model with the height as specified in Table 3.2 and the thickness of individual layers specified in Table 3.4 was used. The pouch material on either sides were specified as per the specifications from Table 3.3. Approximate material properties of individual layers were selected from [45] and are mentioned in Table 3.5. Figure 3.5 shows the layered thermal model used in the preliminary analysis setup. A simple free triangular meshing was used.

Except for the pouch materials on either sides, rest of the layers are considered to be heat sources with a total heat output of $15\,000\,\mathrm{W/m^3}$. It is to be noted that this is an assumed value and its significance is ignorable as the same heat output will be considered in the lumped thermal model. Outer pouch surfaces, upper and lower surfaces are taken to be exposed to air at an ambient temperature of 20 °C and heat transfer coefficient $h = 10\,\mathrm{W/m^2 \cdot K}$. The boundary conditions are shown in Figure 3.6.

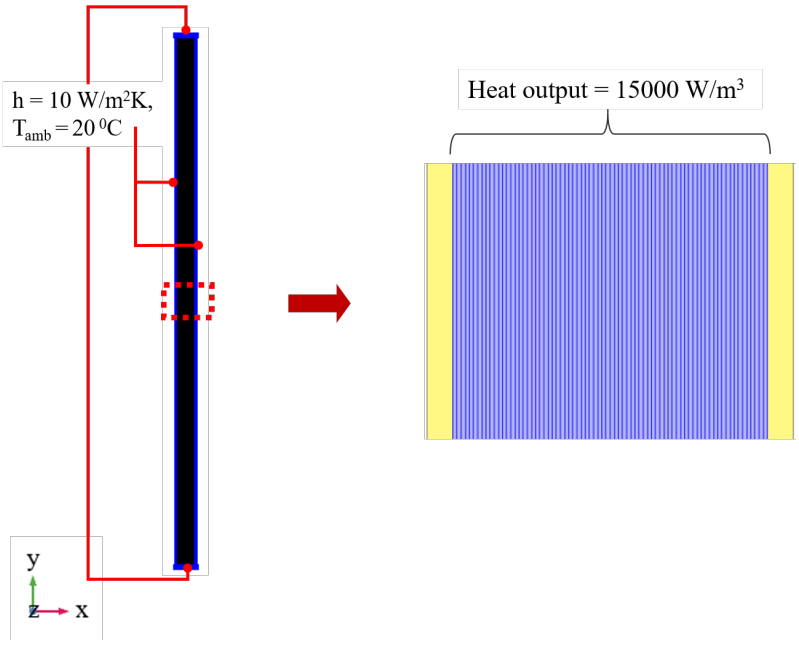

Figure 3.6: Boundary conditions used for layered thermal model

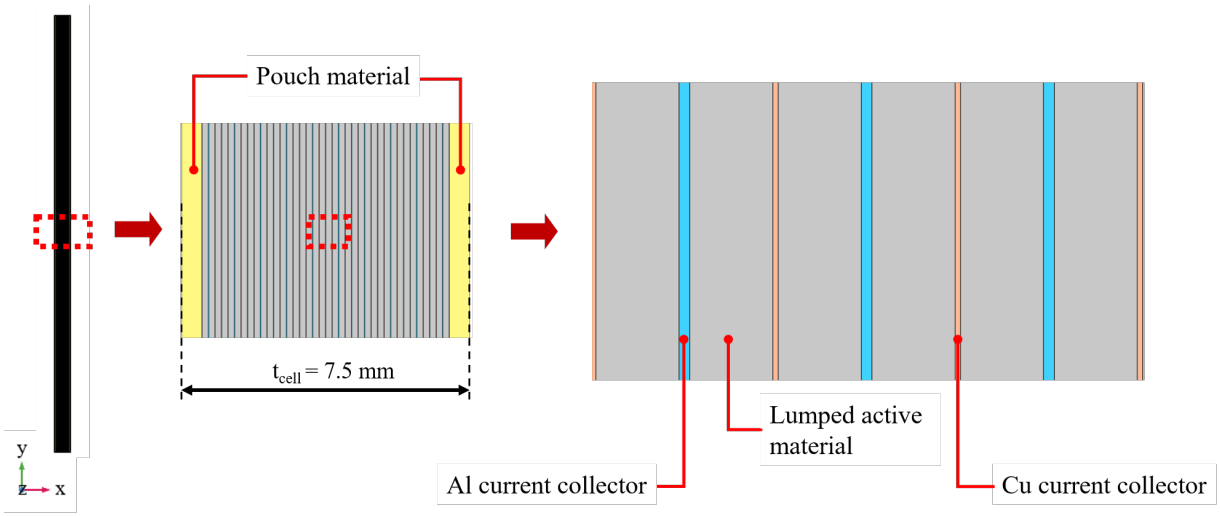

Figure 3.7: 2-D view of lumped thermal model with lumped active material and cell height of 200 mm

3.2.2.2 Lumped Thermal Model

In case of the lumped thermal model as shown in Figure 3.7, layers between a set of Cu current collector and Al current collectors are replaced by an equivalent lumped active material with the equivalent properties. Grey layer shown in Figure 3.7 refers to this lumped active material. Its equivalent properties are computed from the individual material properties specified in the first three columns of Table 3.5. The final column represents the lumped material properties and calculation procedure is as below, which is based on weighted average methods explained in the following sections. The subscripts 'an' relates to the anode, 'sep' relates to the separator and

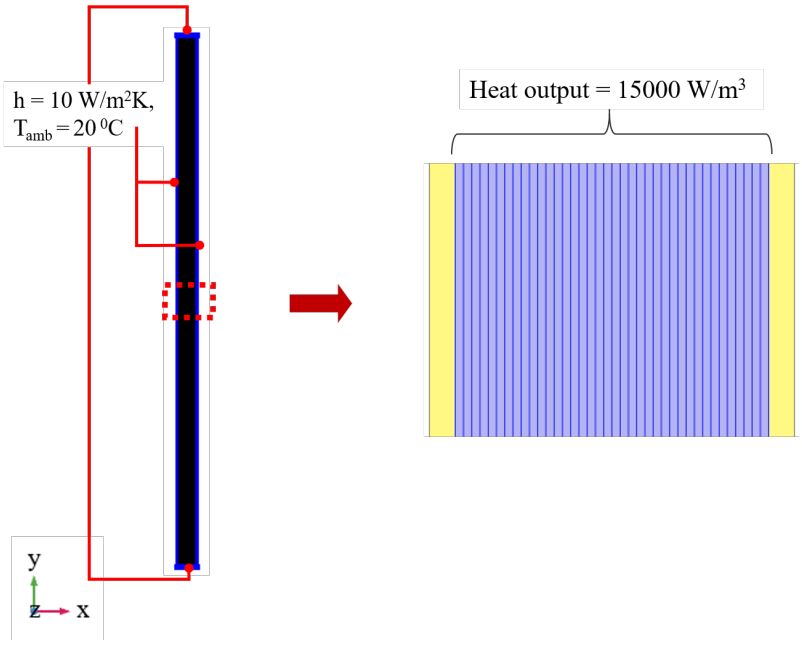

Figure 3.8: Boundary conditions used for lumped thermal model

'cath' relates to the cathode.

$$\rho_{\ lumped} = \frac{\rho_{an}\ V_{an} + \rho_{sep}\ V_{sep} + \rho_{cath}\ V_{cath}}{V_{an} + V_{sep} + V_{cath}} \tag{3.3}$$

$$Cp_{\ lumped} = \frac{Cp_{an}\ \ \rho_{an}\ \ V_{an} + Cp_{sep}\ \ \rho_{sep}\ \ V_{sep} + Cp_{cath}\ \ \rho_{cath}\ \ V_{cath}}{\rho_{an}\ \ V_{an} + \rho_{sep}\ \ V_{sep} + \rho_{cath}\ \ V_{cath}} \tag{3.4}$$

In the above equations, the volume of the layers V_{an}, V_{sep} and V_{cath} are computed using the individual thicknesses and the cell height, width.

$$V_{an} = H_{cell}\ W_{cell}\ t_{an} \tag{3.5}$$

$$V_{sep} = H_{cell}\ W_{cell}\ t_{sep} \tag{3.6}$$

$$V_{cath} = H_{cell}\ W_{cell}\ t_{cath} \tag{3.7}$$

$$k_x = \frac{t_{an} + t_{sep} + t_{cath}}{t_{an}/k_{an} + t_{sep}/k_{sep} + t_{cath}/k_{cath}} \tag{3.8}$$

$$k_y = \frac{k_{an}t_{an} + k_{sep}t_{sep} + k_{cath}t_{cath}}{t_{an} + t_{sep} + t_{cath}} \tag{3.9}$$

k_x represents the through-plane conductivity and k_y represents the in-plane conductivity. The same boundary conditions used for layered thermal model are used which aid in the comparison of the temperature distribution discussed in the results section. Figure 3.8 depicts the boundary conditions considered.

Table 3.5: Individual layer properties solely used for thermal model [45]

Parameter	Anode	Separator	Cathode	Lumped active material
thickness (μm)	64.5	16	74	154.5
density (kg/m^3)	2250	886	2200	2084.8
specific heat capacity (J/kg · K)	707.7	1700	641	717.66
thermal conductivity (W/m · K)	24	0.249	2.1	$k_x = 1.512$ $k_y = 11.051$

The main purpose of this comparison was to determine if the individual layers such as the anode, separator and the cathode can be replaced by an equivalent material to simplify the model and reduce computational demand. Consequently, the discussion in the results section supports the lumped material consideration and hence the lumped active material is used in the following sections.

3.2.3 Full Cell

A full cell has 38 unit cells arranged as described for the single sheet stacking in Figure 2.19 and the same method is followed in creating a full cell geometry. The thickness of operational material of the cell, i.e., without the pouch is 6451 μm. As no specific data was available for the pouch material of the given cell, considering less significant differences in materials, the pouch layer from [46] was used. Since the total thickness of the cell was 7500 μm, the constituent sub-layers from [46] with a proportional increase to make cell thickness as 7500 μm was modeled. This meant a 524.5 μm thick pouch layer on either surfaces as depicted in Figure 3.9. Due to surface meshing errors and lower heat transfer area, lateral surfaces and tab collars were not covered.

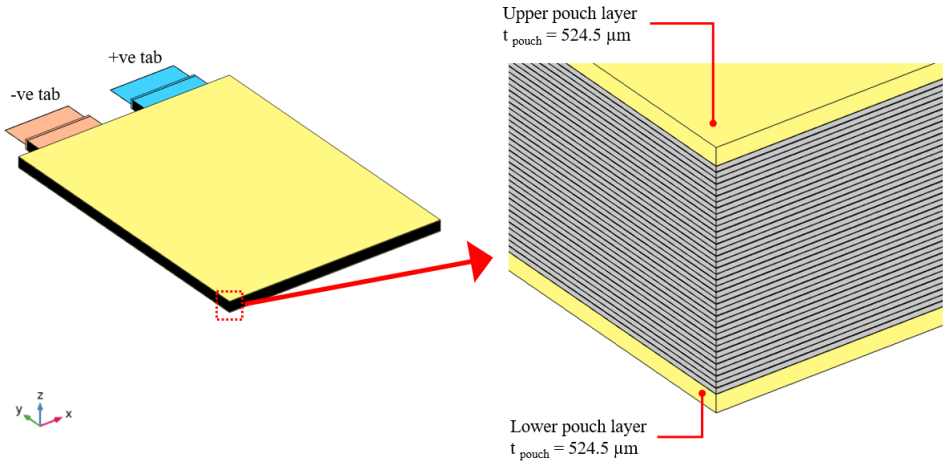

Figure 3.9: 3-D geometry of the full cell with magnified pouch layer

As it is not particularly possible to represent the weld between current collector projections and tabs, a solid contact was used for the same accounting for metal fusion at the contact. This closely relates to the arrangement in the real cells.

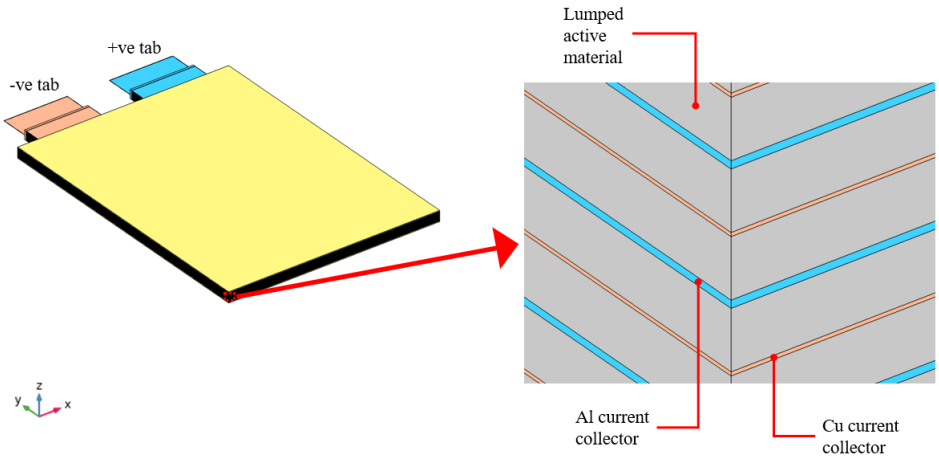

Figure 3.10: 3-D geometry of the full cell with magnified layer arrangement

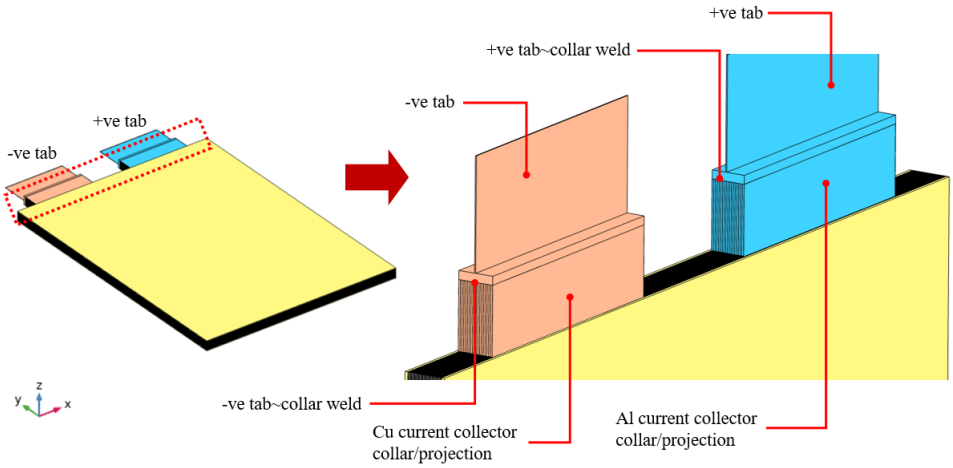

Figure 3.11: 3-D geometry of the full cell with magnified tab and current collector arrangements

Figure 3.10 and Figure 3.11 represent the magnified views of individual lumped layer arrangements and tab assembly respectively.

3.2.4 Material Properties

Some of the materials used in Li-ion cells are relatively common and their respective alloys are used widely in other applications on a daily basis. These are the current collectors - Al and Cu. Their material properties relevant to the simulations are tabulated in Table 3.4. As Al and Cu are pure in this study, their properties are assumed to be isotropic.

3.2.4.1 Pouch Material

Table 3.3 quantifies the pouch material properties used. Based on the weighted average method, density, specific heat capacity and thermal conductivities are computed. It can be noted that instead of using all three layers on each side of the cell surface as pouch cover to ease meshing and computations while not compromising on accuracy. The innermost layer is polypropylene (PP), the middle layer is aluminum (Al) and the outer layer is polyamide (PA.) V represents the volume of each substituent in the subscript.

1. *Density* (ρ_{pouch}) : The generalised individual material densities are taken from [45]. Minor adjustments were made based on calibrations of active material density.

$$\rho_{pouch} = \frac{\rho_{PP}\ V_{PP} + \rho_{Al}\ V_{Al} + \rho_{PA}\ V_{PA}}{V_{PP} + V_{Al} + V_{PA}} \tag{3.10}$$

2. *Specific heat capacity* (Cp_{pouch}) : The individual material specific heat capacities are taken from [45].

$$Cp_{pouch} = \frac{Cp_{PP}\ \ \rho_{PP}\ \ V_{PP} + Cp_{Al}\ \ \rho_{Al}\ \ V_{Al} + Cp_{PA}\ \ \rho_{PA}\ \ V_{PA}}{\rho_{PP}\ \ V_{PP} + \rho_{Al}\ \ V_{Al} + \rho_{PA}\ \ V_{PA}} \tag{3.11}$$

3. *Thermal conductivity* (k_{pouch}) : Individual material thermal conductivities are taken from [45]. Thermal conductivity is anisotropic in nature, hence is computed as along the surface, i.e., in the x-y plane called in-plane conductivity k_x, y and along z-direction called through-plane, with each layer thickness t followed by respective subscript.

$$k_{pouch\ x,y} = \frac{k_{PP}t_{PP} + k_{Al}t_{Al} + k_{PA}t_{PA}}{t_{PP} + t_{Al} + t_{PA}} \tag{3.12}$$

$$k_{pouch\ z} = \frac{t_{PP} + t_{Al} + t_{PA}}{t_{PP}/k_{PP} + t_{Al}/k_{Al} + t_{PA}/k_{PA}} \tag{3.13}$$

4. *Electrical conductivity* (σ_{pouch}) : A very low non-zero electrical conductivity is used since pouch material is an insulator with Al layer in between for mechanical strength. The presence of PP and PA on either sides of the Al layer attenuates the conductivity both in-plane and through-plane.

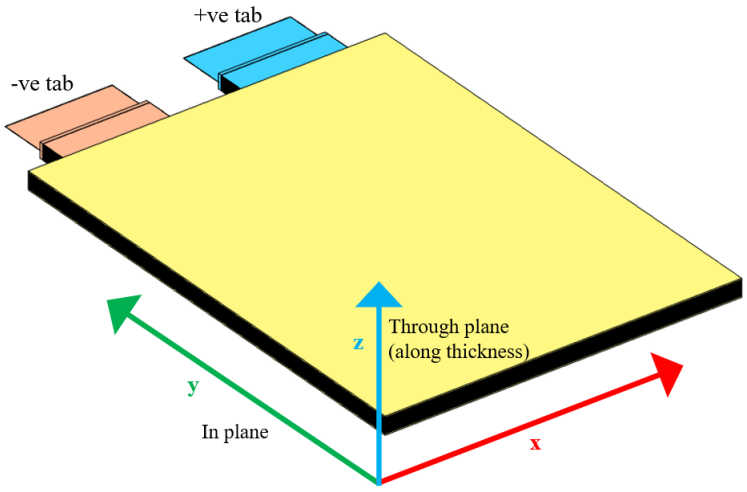

Figure 3.12: 3-D geometry of the full cell illustrating in plane and through plane axes

3.2.4.2 Lumped Active Material

As mentioned in previous sections, a lumped material with equivalent material properties was created. Contrary to the current collectors, lumped active material has anisotropic properties and they define the behavioural characteristics of the cell. Based on the general properties of the study cell from [47], density, specific heat capacity and electrical conductivity were calibrated. These calculations involved the consideration and contributions from the pouch material, current collectors. Figure 3.12 shows the reference axes used for the cell geometry along with in and through-plane directions.

1. *Density* (ρ_{active}) : Based on the weighted average method, when the individual densities, volumes of constituent materials (in this case, current collectors, tabs) is known along with the overall weight of a cell, the density of the remaining material is calculated based on its known volume. The active material's volume is the sum of cathode, separator and anode of all the unit cells. The current collector tabs volume are included in their respective current collector volumes. The mass of cell (m_{cell}) was taken from [47].

$$V_{active} = 38 \times (V_{cathode} + V_{separator} + V_{anode}) \tag{3.14}$$

Equation (3.14) uses 38 times the magnitude of individual layers as the study cell has 38 active layers.

$$t_{active} = 38 \times (t_{cathode} + t_{separator} + t_{anode}) \tag{3.15}$$

$$\rho_{active} = \frac{m_{cell} - (\rho_{Cu}\, V_{Cu} + \rho_{Al}\, V_{Al} + \rho_{pouch}\, V_{pouch})}{V_{active}} \tag{3.16}$$

The lateral layers' material was compensated in equation (3.16) itself.

2. *Specific heat capacity* (Cp_{active}) : Similar to the method followed above, weighted average procedure aided in specific heat capacity calculations. Specific heat capacity (Cp_{cell}) of the cell was taken from [47].

$$Cp_{active} = \frac{Cp_{cell} \;\; m_{cell} - (Cp_{Cu} \;\; \rho_{Cu} \;\; V_{Cu} + Cp_{Al} \;\; \rho_{Al} \;\; V_{Al} + Cp_{pouch} \;\; \rho_{pouch} \;\; V_{pouch})}{\rho_{active} \;\; V_{active}} \tag{3.17}$$

3. *Thermal conductivity* (k_{active}) : Similar to the thermal conductivity of pouch material, the active material is anisotropic in nature as well. Due to lower thermal resistance in-plane, the conductivity is higher in the x-y plane when compared to the through-plane in the z-direction. Available general material properties of LMO-NMC (cathode), Graphite (anode) and polypropylene (separator) are considered from [45].

$$k_{active\ x,y} = \frac{k_{cathode}t_{cathode} + k_{separator}t_{separator} + k_{anode}t_{anode}}{t_{cathode} + t_{separator} + t_{anode}} \tag{3.18}$$

$$k_{active\ z} = \frac{t_{cathode} + t_{separator} + t_{anode}}{t_{cathode}/k_{cathode} + t_{separator}/k_{separator} + t_{anode}/k_{anode}} \tag{3.19}$$

4. *Electrical conductivity* (σ_{active}) : Contrary to the magnitude of electrical conductivity of current collectors, the magnitude of active material is significantly lower and contributes to most of the internal resistance of the cell. To determine the active material's conductivity variation with temperature, a 1-D electro-chemical model developed by *Evelina et al.* in [26] was used. For a fixed current, with the same initial SoC, cases with different temperatures were simulated and corresponding resistances were calculated using basic relations between voltage drop, current and resistance. Then, the electrical conductivity was computed from the resistances for different temperatures to arrive at empirical polynomial functions relating to electrical conductivity and temperature. For the calibration of the model, the active material's conductivity was deduced to be 0.048 S/m at 20 °C resulting in the full cell's resistance to be 3 mΩ. A temperature range of −10 °C to 77 °C was considered as a common Li-ion cell operating window.

$$\sigma_{active} = 7 \times 10^{-6}\ T^2 - 0.0025\ T + 0.17956 \tag{3.20}$$

where, σ_{active} is in S/m and T is in K.

As can be seen from Figure 3.13, the magnitude difference between current collectors and the active material is of the order 10^8 and its effect on cell resistance is elaborated in the results section.

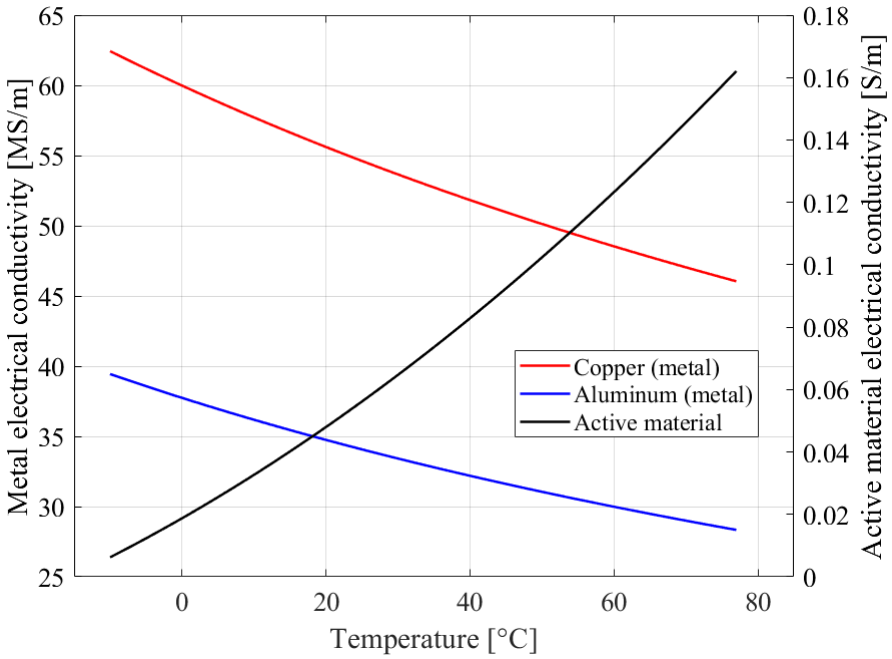

Figure 3.13: Electrical conductivities of Cu and Al current collectors, Lumped active material

3.2.5 Simulation Set-up in COMSOL - Multiphysics®

Based on the fundamental repeatability of the unit cells, two models are built. One which represents unit cell and the other representing a full cell. The modeling procedure was described in sections 3.2.1.2 and 3.2.3 respectively.

3.2.5.1 Unit Cell

- Meshing : As shown in Figure 3.14, a swept mesh was created as it provides good accuracy with lower memory and computational power demand. The Al current collector outer face is the start face and the opposite Cu current collector face is the destination for the sweep. The sweep passes through the lumped active material. The average element quality was 0.9459, while the maximum possible quality is 1.
- Boundary conditions
  - Thermal : An initial temperature of 20 °C was considered for the entire unit cell. This was based on the assumption that the cell was not operational for a significant amount of time and stored at room temperature. Both the opposite faces were exposed to air at 20 °C with heat transfer co-efficient $10\,\mathrm{W/m^2 \cdot K}$. Since a single unit cell is modeled in this section, the heat dissipated is $1/38^{th}$ times the full cell. Hence, h is revalued at $10/38\,\mathrm{W/m^2 \cdot K}$.
  - Electrical : As the charges flow through the cell during charging and discharging, the internal resistance generates heat. During charging, -ve electrode is the source of charges (Li^+) ions which flow through the cell

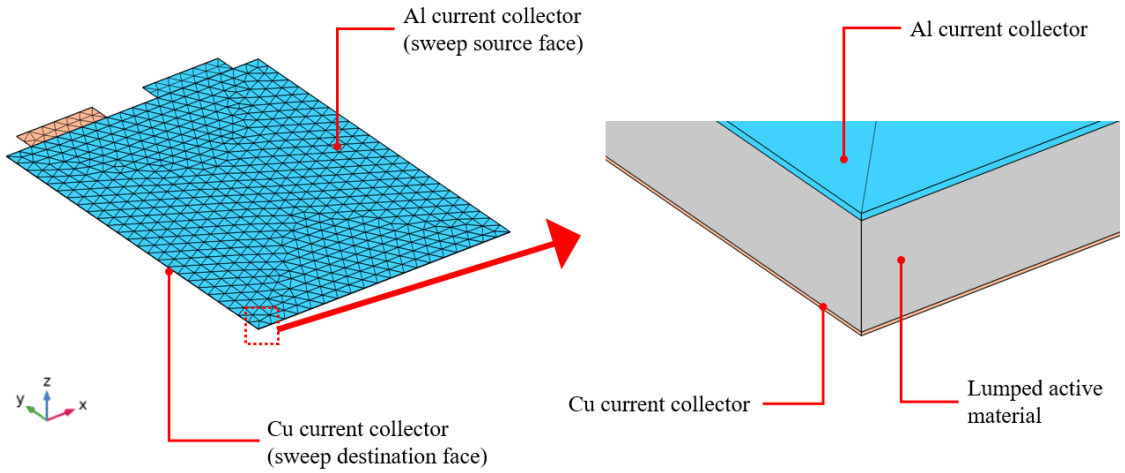

Figure 3.14: Sweep mesh of an unit cell

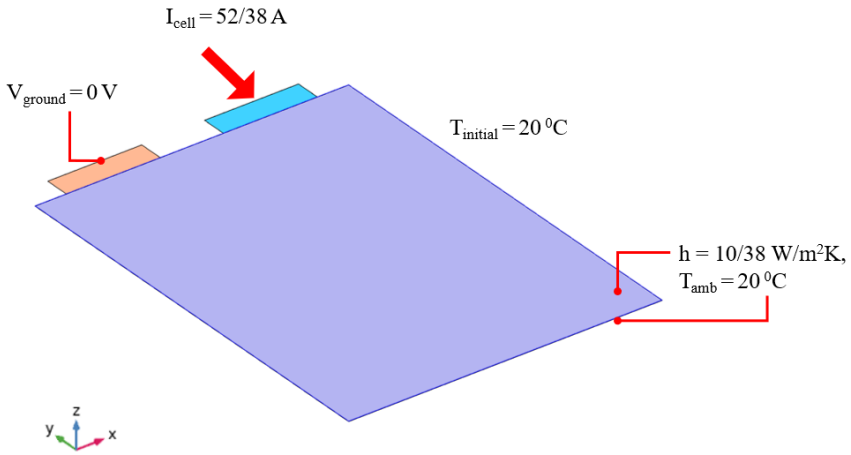

Figure 3.15: Electrical and Thermal boundary conditions

while +ve electrode is (Li^+) ions source during discharge. To simulate the same, one of the electrodes was grounded and the other electrode was fed an input current of 2C, i.e., 52/38 A as it is a unit cell model. Figure 3.15 illustrates the thermal and electrical boundary conditions considered for the unit cell.

- Steady-state simulations : As described before, a current of 2C for a single unit cell was used. For the calibration of electrical conductivity (σ) of active material, no temperature dependence of electrical conductivity was considered initially. After the calibration, temperature dependence and temperature independent conductivity simulations were carried out to understand the temperature distribution.

3.2.5.2 Full Cell

- Meshing : The assembled full cell with all 38 layers and pouch material was meshed using the same method as in the unit cell model. However, the source

face in the full cell was the pouch material surface on one side with the destination ending on the opposite face as shown in Figure 3.16. The tabs were meshed separately using domain sweep function and prismatic elements. The average element quality of the entire cell was 0.8466.

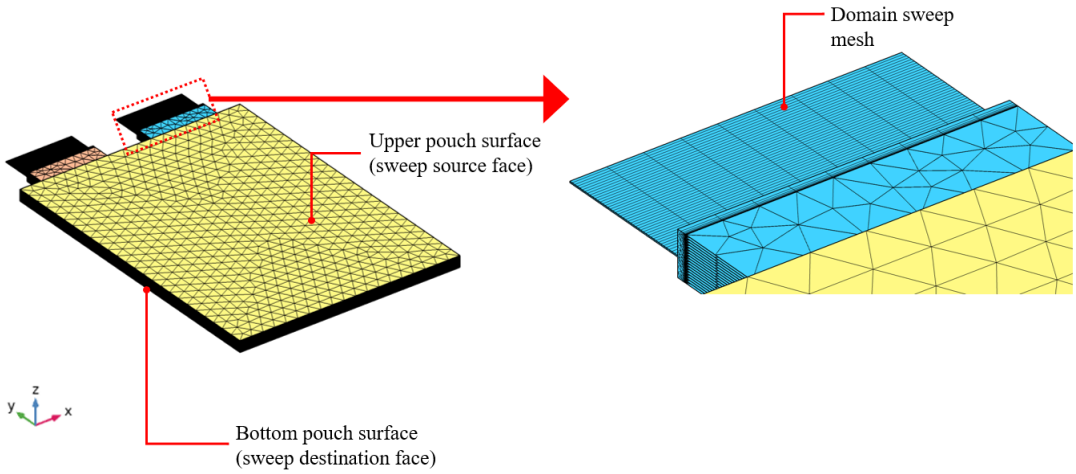

Figure 3.16: Sweep mesh of a Full cell

- Boundary conditions
  - Thermal : Both the pouch surfaces are exposed to ambient conditions of air at 20 °C and a heat transfer co-efficient 10 $W/m^2 \cdot K$ as illustrated in Figure 3.17. Similar to the unit cell, the initial state is at 20 °C. The rest of the external surfaces are assumed to be insulated with no heat loss either by convection or radiation.

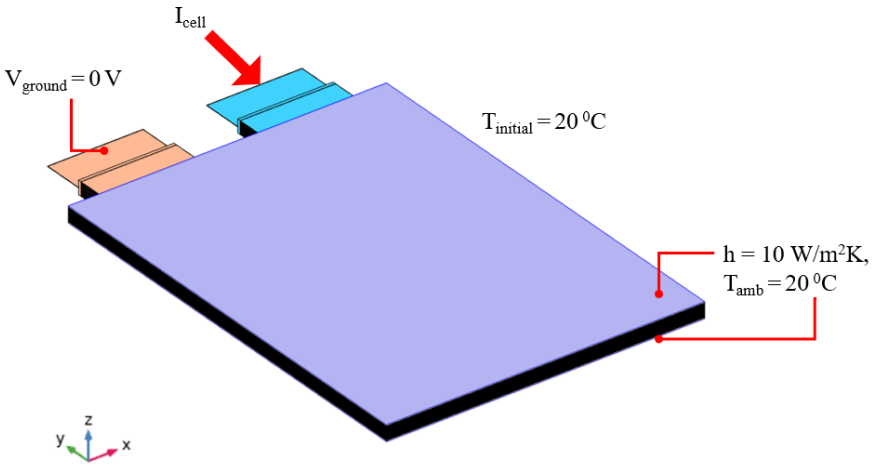

Figure 3.17: Electrical and Thermal boundary conditions of a full cell

  - Electrical : Similar to the unit cell, one of the tabs was grounded and the other one was fed with input current which represents the current delivery from the cell. In steady-state simulations, I_{cell} had a constant value while it varied with time in the WLTC transient simulations.

- Steady-state simulations : A constant 2C was used to simulate the steady-state temperatures and the volumetric temperature distribution was observed. As the cell capacity is 26 Ah, 2C current is 52 A. In order to detect the temperatures at specific locations, theoretical temperature probes were specified as shown in Figure 3.18.

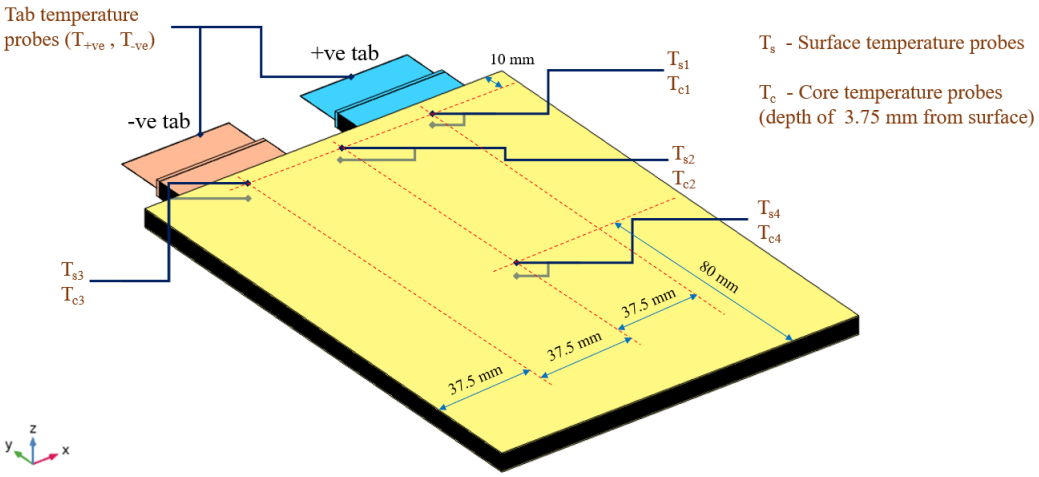

Figure 3.18: Full cell geometry indicating the temperature probe locations

- Transient simulations : From section 2.6, i.e., forces acting on a vehicle during normal operation, the power required at wheels is computed. For the current full cells, their configuration into battery pack is assumed to be made of 80 cells in series and 3 of these 80 cell modules in parallel. From the data-sheet, the cell's nominal voltage was 3.7 V. For the given vehicle parameters in Table 3.1, the tractive power required and current profile for the WLTC was computed. The obtained current profile acts as input for the full cell model. It is to be noted that the dynamic variations in the inverter and power electronics (PE) is ignored and a constant loss of 20% is considered.

  Another case with just 2C current flowing through the cell for 1800 s i.e., 30 minutes was simulated as well to analyse the temperature increase on the surface and at the central layer.

  As shown in Figure 3.19, the total power is determined from the WLTC. Considering inverter and PE bypassing to ignore the dynamic variations with constant loss, current profile is determined.

$$P_{total}(t) = F_{total}\ v(t) = \left[\frac{1}{2}\ \rho\ c_d\ A_f\ m_v\ v^2(t) + c_r\ m_v\ g + m_v\ \frac{dv}{dt}\right] v(t) \quad (3.21)$$

Equation (3.21) gives both the tractive power (+ve) and regenerative power (-ve). The tractive power discharges the battery while the regenerative power recharges. But, all of the regenerative power cannot be utilised; hence only 60% is assumed to be regeneration efficiency.

$$P_{total}(t) = P_{tractive}(t) + P_{regen}(t) \quad (3.22)$$

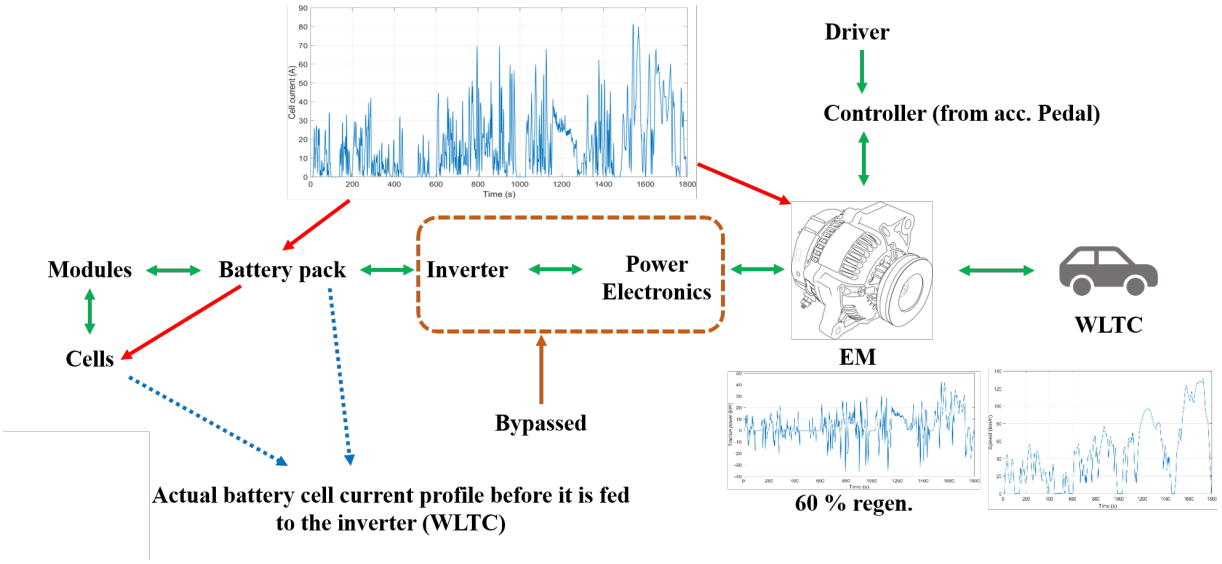

Figure 3.19: Graphical representation of bypassed vehicle sections

$$P_{demand}(t) = 1.2 \times P_{tractive}(t) + 0.6 \times P_{regen}(t) \tag{3.23}$$

$$I_{cell}(t) = \frac{P_{demand}(t)}{n_s \; n_p \; V_{cell}} \tag{3.24}$$

In equation (3.23), 1.2 represents the system losses of 20%, which include EM, the inverter and the PE. Hence, current I_{cell} provided by each cell at each time instant is dependent on power demand from each cell arranged in series and parallel, n_s and n_p respectively with nominal voltage V_{cell}.

Contrary to the cell current profile in Figure 3.20, the cell current in Figure 3.21 is positive throughout the entire duration. This is done to avoid the -ve current error in simulations. Since the cell is purely resistive, the current direction change would not affect the outcome.

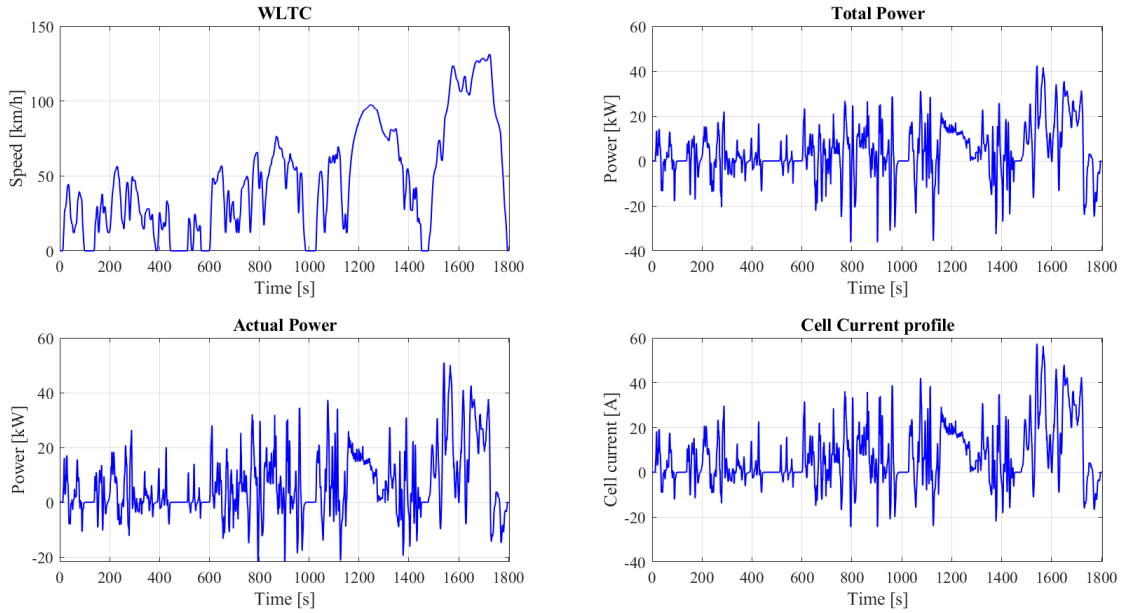

Figure 3.20: Chronological steps and respective plots in calculation of cell current profile

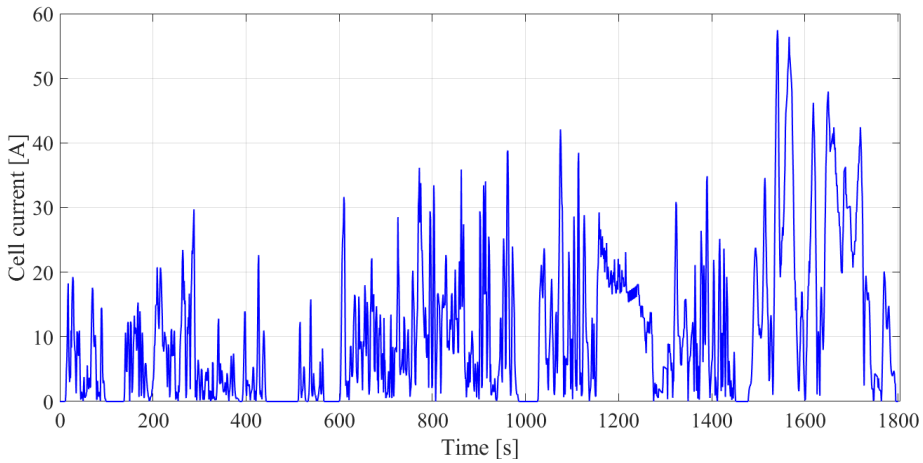

Figure 3.21: Individual cell current profile for WLTC

3.2.5.3 Pulse Test Set-up

- 3-D geometry modeling : The experimental test set-up was arranged from a bakelite base fixed with an Al plate on the surface. Then a thin cardboard was placed on an Al plate on which the test cell lied. The tabs were connected to brass blocks with a textured surface on contact areas for effective electrical contact which compensated the bends and distortions between tabs and brass blocks. The brass blocks got the connections from Cu cables for pulse test inputs. Temperature sensors were attached on the +ve and the -ve tabs, surface of the cell near +ve tab, -ve tab and cell centre. Consequently, a 3-D model for simulation was built with the omission of nut, bolts and Cu cables to avoid the unknown heat transfer direction, i.e., whether heat flowed from

or to the cables.

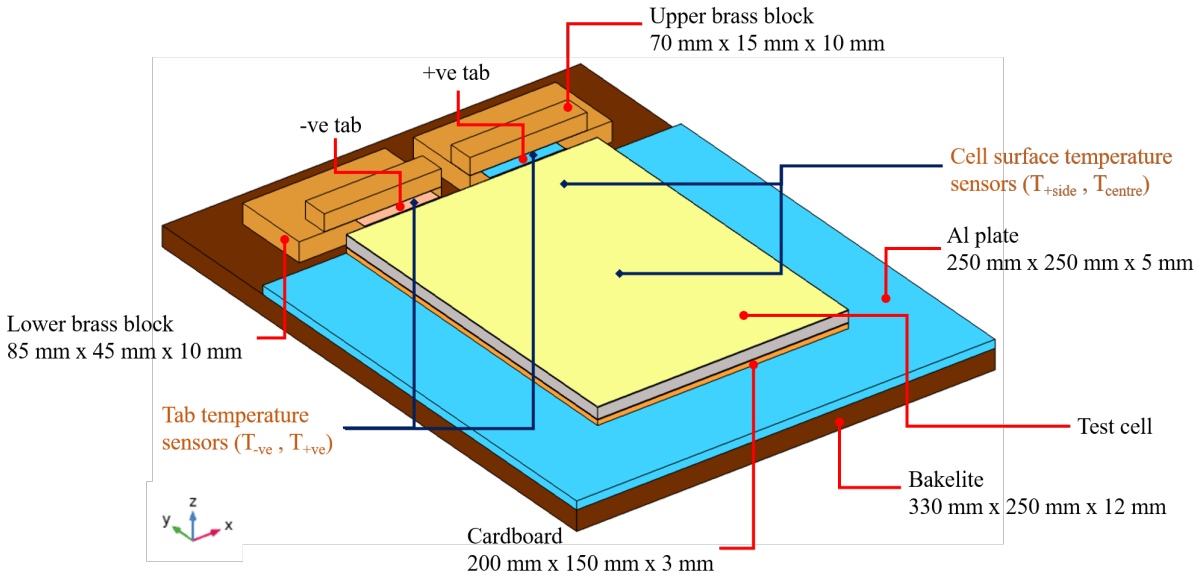

Figure 3.22: 3-D model of pulse test set-up and temperature sensor locations

As can be seen in Figure 3.22, the test cell is modeled as a single central lumped block except for the pouch materials. This simplification is done to accommodate excessive meshing, simulation duration by replacing with equivalent material properties.

- Material Properties : Similar to the calculations in section 3.2.4.2, the cell core material (grey in Figure 3.22) properties were calculated including the current collector materials as well. No temperature dependent conductivity was considered as reversible heat simulation at low SoC was to be simulated. The remaining set-up material properties were taken from [45].

Table 3.6: Test set-up material properties [45]

Parameter	Cell core	Bakelite	Cardboard	Brass
density (kg/m^3)	2600	1300	344.5	8615.4
specific heat capacity (J/kg · K)	1894	920	668	380
thermal conductivity (W/m · K)	$k_x = k_y = 48.931$, $k_z = 1.0647$	0.2	0.064	109

Since the model was based on the constant internal resistance of the cell, it was created as a thermal model with heat input given from equivalent current and internal resistance.

- Meshing : Sweep mesh was created from the cell surface through cell core until the cardboard face, which is in contact with Al plate. For the rest of the components, free tetrahedral meshing was generated. The average element quality was 0.6056. Figure 3.23 represents the meshing details with a total of 374,203 elements in the pulse-test set-up.
- Boundary conditions

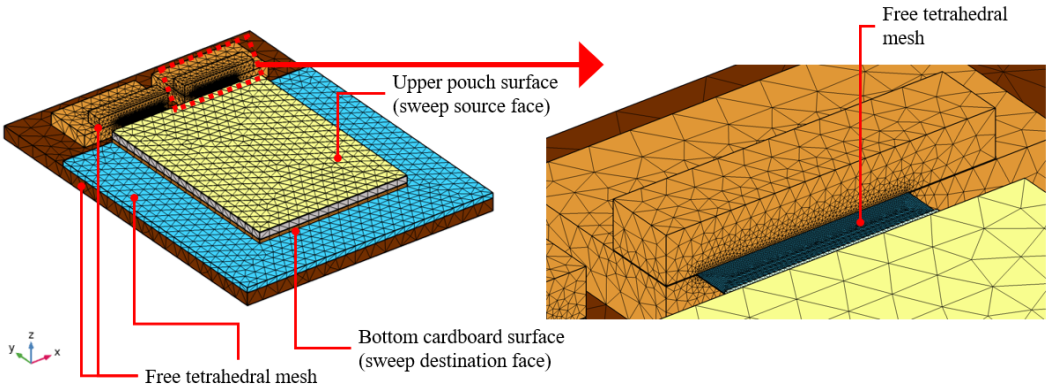

Figure 3.23: Test set-up meshing with 374,203 elements

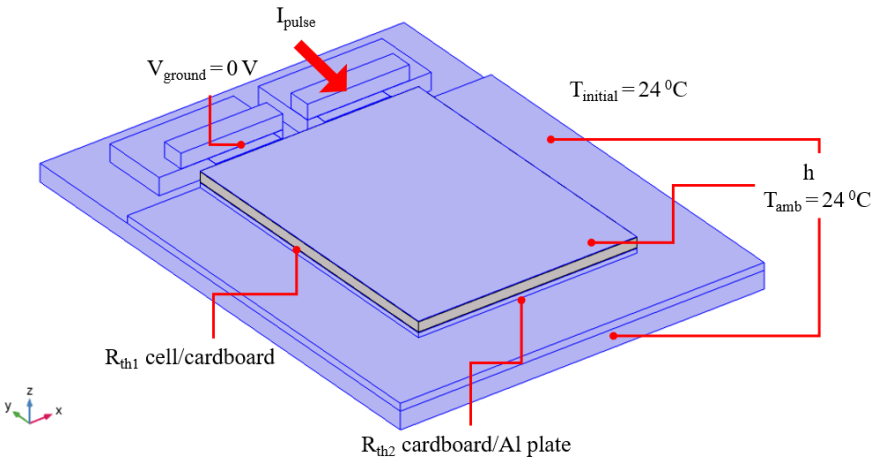

Figure 3.24: Pulse test set-up's boundary conditions with to be calibrated htc

– Thermal : As the experiments were carried out in lab conditions maintained at 24 °C and cell surface exposed to the ambient conditions, the same were used for the simulations. Just similar to experiments, two separate simulations were run. One at high *SoC* (starting at 95%) and another at low *SoC* (starting at 5%). The surroundings for both the cases were almost the same with an excess of about 1 °C in low *SoC* case. Since the tests were run for extended periods of duration, due to limited memory availability, certain particular duration of simulations were run with corresponding inputs to compare similarities. Based on the steady-state temperatures reached on the cell surface, heat transfer co-efficient was calibrated. The thermal contact resistances as shown in Table 3.7 were specified with reasonable assumptions on default surface roughness of Al sheet [45], air gap conductance [45], Al sheet microhardness [45] and calculated contact pressure based on weight are contact areas of cell and cardboard while perfect contact between Al plate and bakelite was considered. The boundary conditions are shown in Figure 3.24. As the length and width of the cell surface is known to be 200 mm and 150 mm respectively, its surface area A in contact with cardboard is 0.03 m^2. The case between cardboard and Al plate is also the same. As the cell weighs

550 g and volume, the density of the cardboard is known, the contact pressures between Cell/Cardboard (P_{th1}) and Cardboard/Al plate (P_{th1}) due to their weights affected by g are calculated as below.

$$P_{th1} = \frac{cell\ weight\ in\ N}{contact\ area\ in\ m^2} \quad \text{Pa} \tag{3.25}$$

$$P_{th1} = \frac{0.55\ kg \times 9.81\ m/s^2}{0.03\ m^2} \approx 180\,\text{Pa} \tag{3.26}$$

$$P_{th2} = \frac{cell\ +\ cardboard\ weight\ in\ N}{contact\ area\ in\ m^2} \quad \text{Pa} \tag{3.27}$$

$$P_{th2} = \frac{(0.55 + 0.031)\ kg \times 9.81\ m/s^2}{0.03\ m^2} \approx 190\,\text{Pa} \tag{3.28}$$

Table 3.7: Thermal contact resistance parameters between cell surface/Cardboard and Cardboard/Al plate

Parameter	Cell / Cardboard interface	Cardboard / Al plate interface
Contact model	Constriction conductance with interstitial gas	Constriction conductance with interstitial gas
Constriction conductance	Cooper-Mikic-Yovanovich correlation	Cooper-Mikic-Yovanovich correlation
Gap conductance ($\text{W/m}^2 \cdot \text{K}$)	0.5	0.5
Surface roughness - asperities avg. height (μm)	15	15
Surface roughness - asperities avg. slope	0.5	0.5
Contact pressure (Pa)	**180**	**190**
Microhardness (MPa)	3	3

  - Electrical : As given in the equation (2.34), during a charging or discharging process, SoC varies hence changing the reversible heat quantity. Consequently, the total heat released can be +ve or -ve based on the magnitude of current and SoC at which the current is delivered. As the complexity of introducing -ve heat is high in COMSOL®, an equivalent current is computed in MATLAB and the same is fed in COMSOL-Multiphysics® simulations. The same currents as in the experimental test are used. Hence the two cases adopted are high SoC and low SoC.

$$Q_{total}(t) = I^2(t)R_{cell} + I(t)\ T\ \frac{dU_{OCV}}{dT}(SoC) \tag{3.29}$$

- Steady-state simulations : A constant current of $2C = 50\ A$ was used for calibration of heat transfer coefficient and thermal contact resistance between cell lower face, cardboard and Al plate. Since the heat exchange between the Cu cables used to provide and draw current from the cell could not be quantified, tab temperatures were given less prominence against temperatures at cell centre and +ve side.

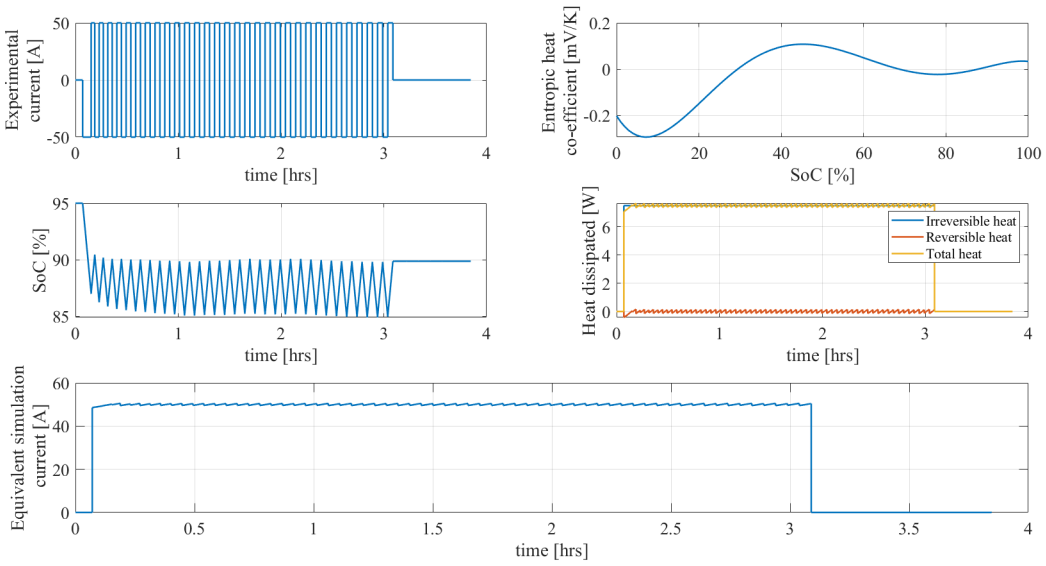

Figure 3.25: High *SoC* equivalent simulation current

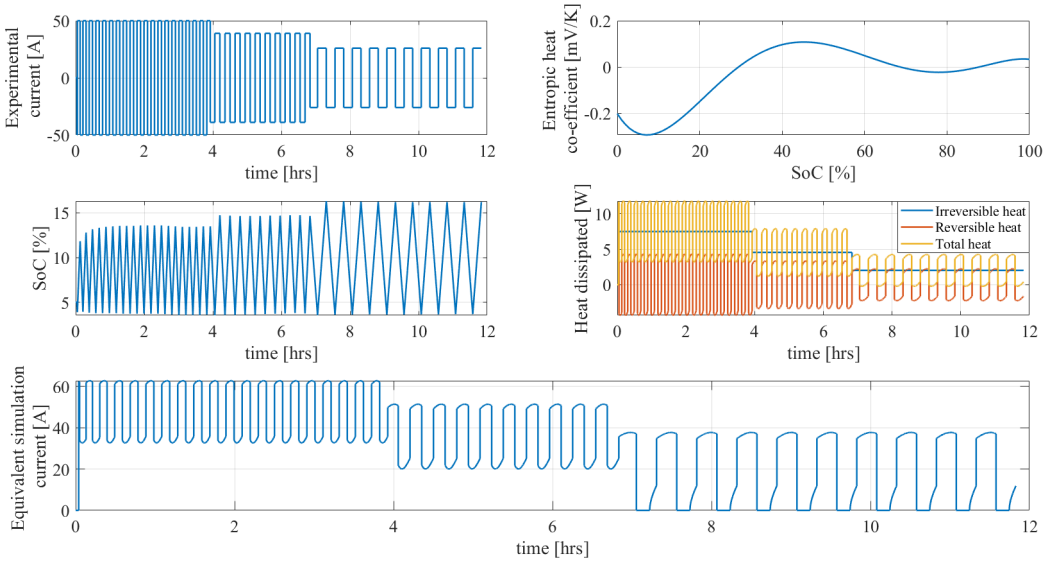

Figure 3.26: Low *SoC* equivalent simulation current

- Transient simulations : For high *SoC*, only an initial section until 4800 s was simulated to determine the similarities. Since the reversible heat effect is not significant at high *SoC*, the total heat generated is within a few percent deviations from the irreversible heat. Figure 3.25 shows the equivalent simulation current used in simulation and the *SoC* variations, heat dissipation for the pulses. In low *SoC* simulations, two separate subcases were considered. One at the start of simulation from 0 s to 3600 s, another from 10140 s - 13800 s to observe the trend of variation. As mentioned before, due to the major contribution from reversible heat at low *SoC*, the total heat dissipated from the cell varied significantly when compared to the high *SoC* case. Correspondingly, the

equivalent simulation current characteristics varied as well. Figure 3.26 shows the simulation input current used along with the resulting SoC variation with the initial state at 5% and individual heat contributing factors.

3.2.6 Establishing Quantitative Relation between Cell Core and Surface Temperatures

As can be intuitively deduced, the temperature at the core of the cell is always higher than at the surface unless the cell is being heated externally as in case of low temperature operations. From the simulations carried out based on previous sections and corresponding results obtained, quantitative empirical relations were formed between surface and core temperatures. As two cases - 2C and WLTC were considered, two empirical equations were obtained based on resulting plots from Figure 4.16 and Figure 4.23. Since the temperatures were relatively higher near the +ve tab region i.e., below the tab and current collector projections, relations between T_{s1} and T_{c1} were established as described in section 4.3.2 for 2C and WLTC currents. The empirical relations between T_{s1} and T_{c1} obtained were basis for cooling system simulations.

$$T_{c1} = 1.038 \times T_{s1} - 0.6824 \tag{3.30}$$

Equation (3.30) is the empirical relation obtained for 2C current simulation results which approximately relates to high speed/high acceleration vehicle operation.

$$T_{c1} = 1.051 \times T_{s1} - 1.015 \tag{3.31}$$

Equation (3.31) is the empirical relation obtained for WLTC current simulation results which is not as aggressive as 2C current operation.

3.3 Modeling and Simulation : Powertrain Cooling System

Section 2.4 has laid out the importance of a cooling system and how it affects vehicle performance. A cooling system consisting of a Radiator and an A/C integration has proved to be most effective and is employed currently in the automotive industry. Hence, for the system analysis, a reference model created previously in GT-Suite® as part of the engineering project described in [39] is used. The model considered is called Even-split model, which assumes an equal amount of parallel refrigerant flow through the battery modules. Due to limited knowledge of proper sub-component sizing in the A/C circuit, the components were dimensioned based on intuition and logical assumptions. These sub-components include compressor, piping, heat exchangers, accumulators, pump, cooling fans, among others shown in Figure 3.27. The highlighted section is a battery TMS operated on VCR, i.e., A/C circuit and is of primary focus in the current study. Just as mentioned in the previous sections, simulations are run with 2C and WLTC, the former representing a high-speed operation, rapid acceleration.

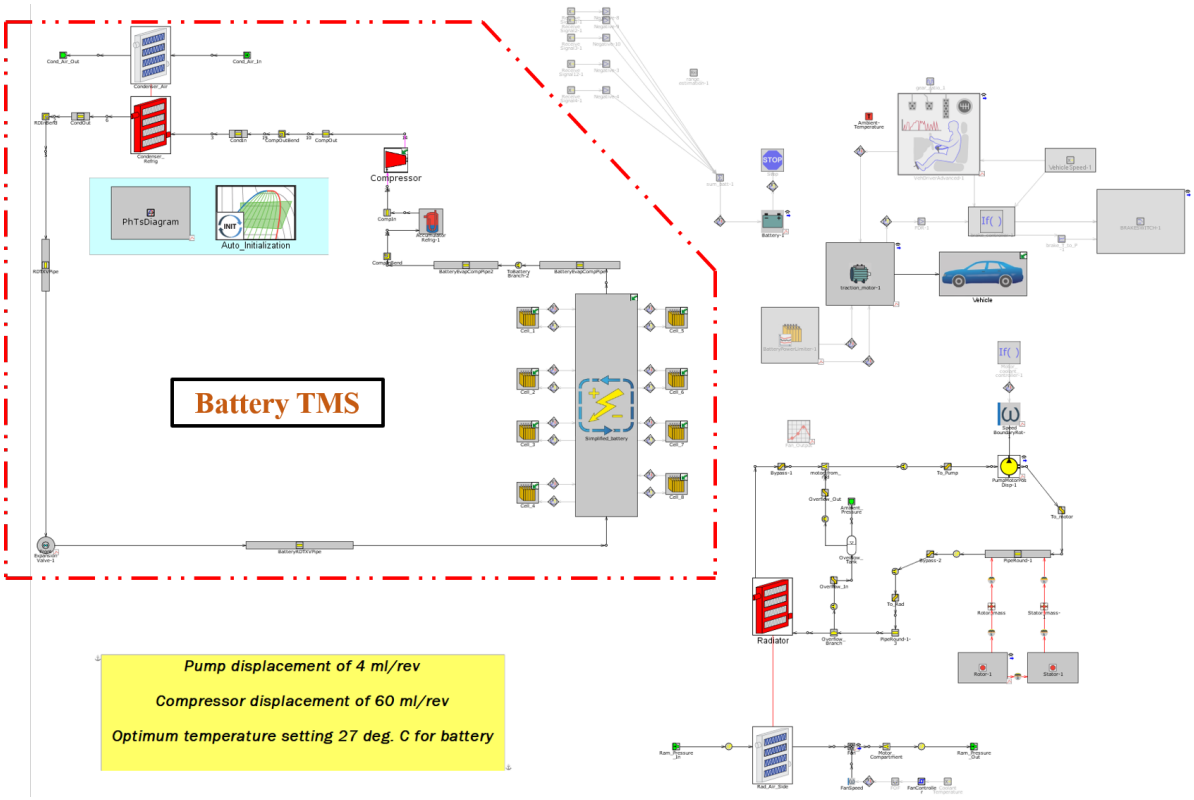

Figure 3.27: Vehicle model with battery TMS operating on VCR and IM TMS working with radiator

Figure 3.28 shows the magnified view of battery TMS with all the prominent components. The compressor has a simple inbuilt controller which moderates the compressor speed based on the temperature input signal from the simplified battery.

Figure 3.29 depicts the internal arrangement of a simplified battery where each

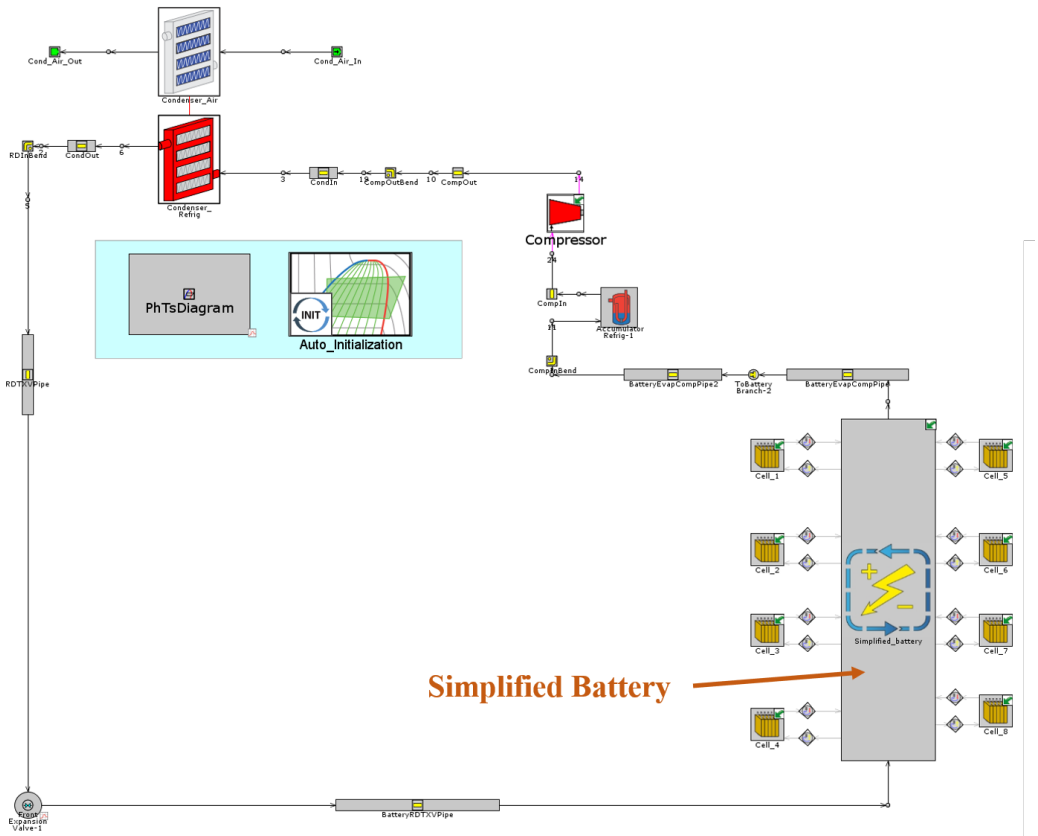

Figure 3.28: Magnified Battery TMS with the arrangement of system sub-components

red dot represents a set of modules and all modules together forming a battery pack. The thermal mass at top quantifies the casing and flow channel masses. t_avg is the average surface temperature of cells which is input signal for the compressor controller.

3.3.1 Conventional VCR Cooling System

As shown in Figure 3.30, a simple if-else controller operating based on the average cell surface temperature is employed. For the temperature range between 27 °C and 32 °C, the compressor runs at 1000 RPM while above 32 °C, it runs at 2000 RPM. Hence, for simulations with a conventional cooling system using surface temperatures, t_avg is used as input for both 2C and WLTC case simulations.

3.3.2 Enhanced VCR Cooling System

An enhanced VCR cooling system employs the cell core temperatures as opposed to surface temperature. Hence, from the simulations results obtained in COMSOL - Multiphysics® for both 2C and WLTC, empirical equation relating surface and core temperature near the +ve tab represented in Figure 3.18 as T_{s1} and T_{c1} are used. Hence, t_avg is replaced by $(1.038 \times t\_avg - 0.6824)$ for 2C from (3.30) and by $(1.051 \times t\_avg - 1.015)$ for the WLTC from (3.31).

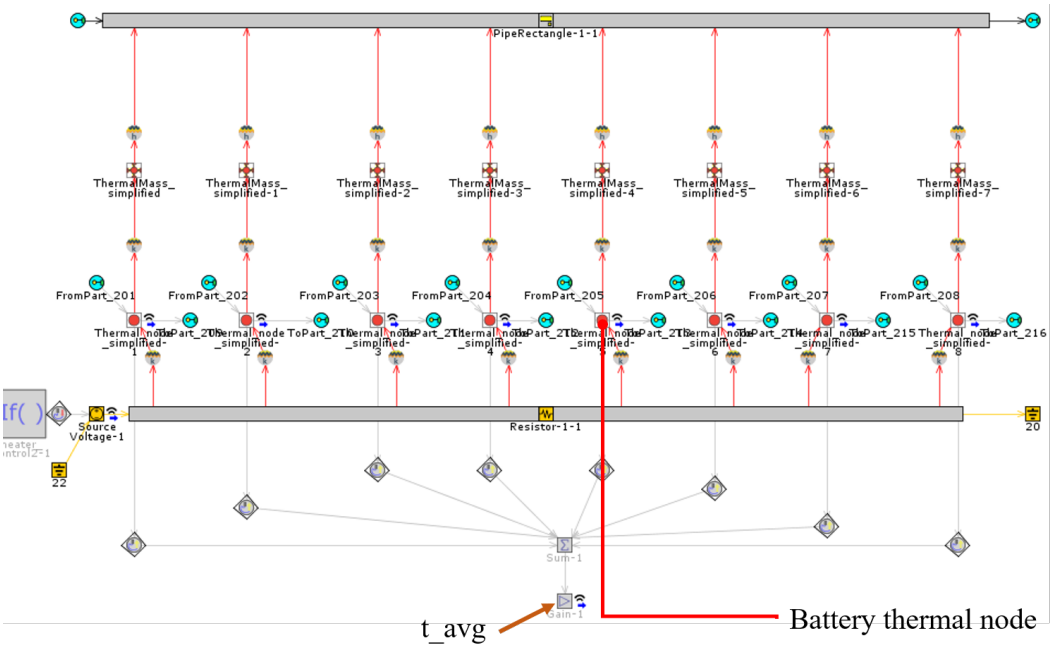

Figure 3.29: Internal view of simplified battery with cell modules as thermal nodes

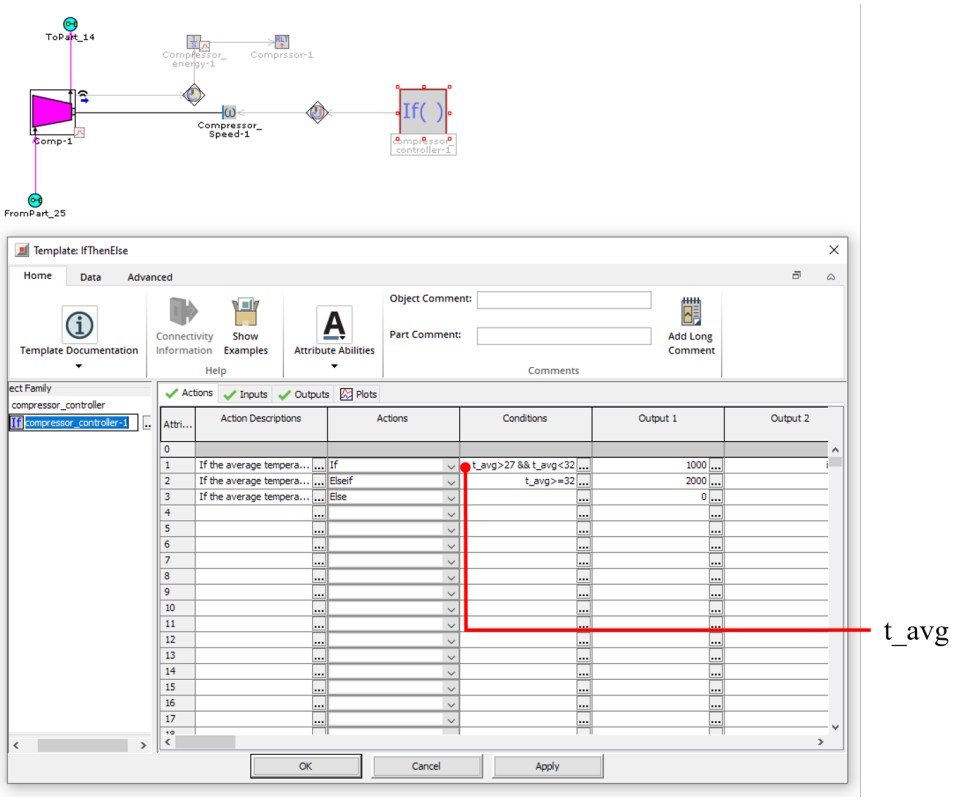

Figure 3.30: Compressor internal section with controller actuation parameter *t_avg*

4

Results and Analysis

Different cases that were described in section 3.2.5 were simulated iteratively while continuously optimising the simulation variables like time steps, solver configurations including stabilisation and acceleration factors to obtain reliable and reasonably accurate results. This section deals with the discussion of the results obtained and corresponding analyses.

4.1 Preliminary Analysis

As the consideration of using a lumped material instead of all the constituent layers was described in section 3.2.2, a preliminary analysis was carried out to determine the reliability of the proposal.

4.1.1 Layered Thermal Model

The test setup considered for the layered thermal model is as described in section 3.2.2.1. With all the outer surfaces exposed to air at ambient conditions (T_{amb}=20 °C, h=10 W/m^2 · K) and having a constant heat output of 15 000 W/m^3 from the inner functional sections as shown in Figure 3.6, following results were observed.

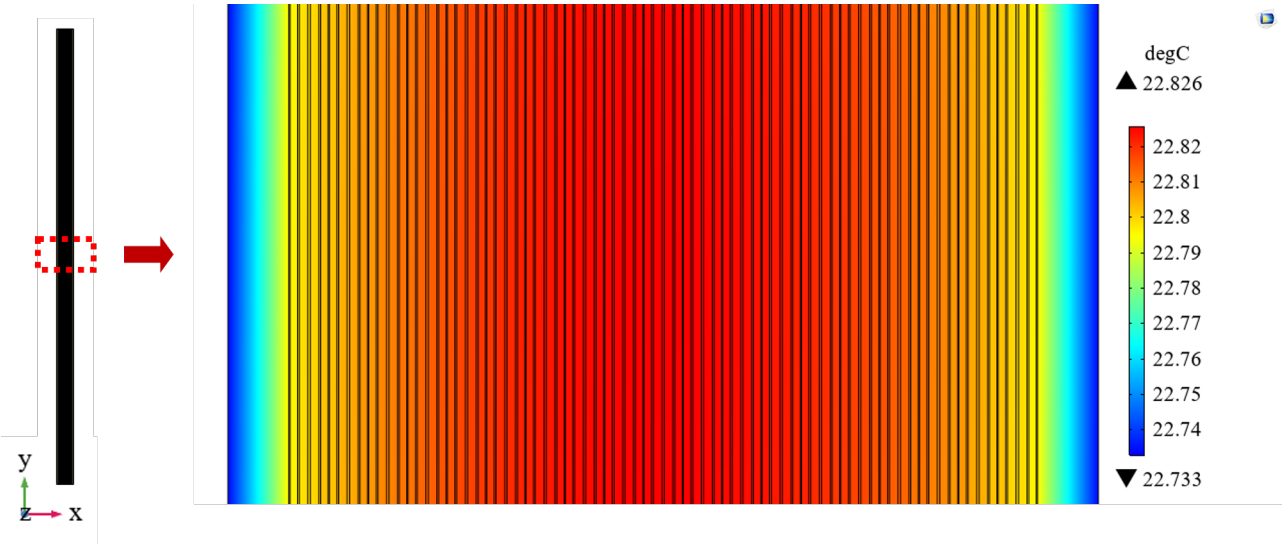

Figure 4.1: Temperature distribution through the cell thickness at the central section in the layered model

Figure 4.1 shows the temperature distribution across the central section of the cell with all the constituent layers. As it can be observed, the central layers are at a higher temperature than the layers at ends. This is attributed to the fact that it takes relatively longer time for the heat to flow from the central section to the external surface than for the layers at the periphery.

4.1.2 Lumped Thermal Model

Section 3.2.2.2 described the test setup and it is same is layered setup for a logical comparison of the cases. Hence, all the outer surfaces are exposed to air at ambient conditions and a constant heat source of 15 000 W/m^3 from the inner functional sections as shown in Figure 3.8, the following results were observed.

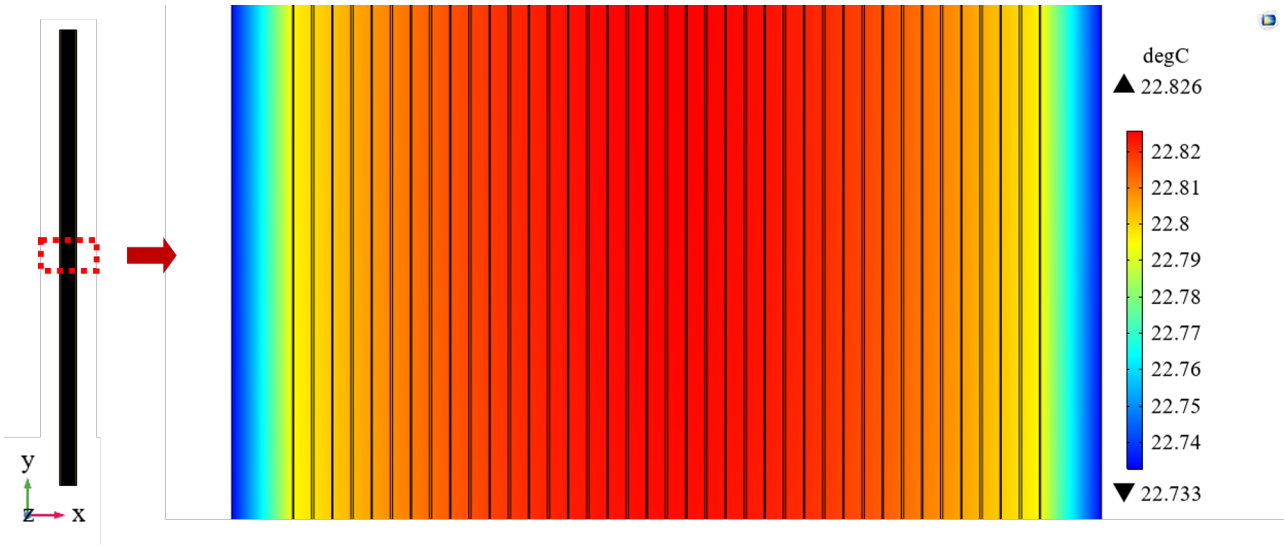

Figure 4.2: Temperature distribution through the cell thickness at the central section in the lumped model

Figure 4.2 shows the temperature distribution across the central section of the cell with all the constituent layers. Similar to the layered model and due to the same reason, the temperature at the peripheral layers closer to the external surfaces are at a lower temperature than the central layers. However, it is to be noted that the active layers of the anode, separator and the cathode are lumped into a single lumped active material with the equivalent properties.

4.1.3 Layered vs Lumped Thermal Model

To determine the error in temperature distribution between both the above approaches, the temperature across the central horizontal section was plotted against the thickness as shown in Figure 4.3 and Figure 4.4.

As it can be clearly observed from Figure 4.3, the maximum temperature drop of 0.07 °C occurred in the pouch layer on either extreme sides. This is attributed to the lower thermal conductivity of the pouch material and its direct contact with the

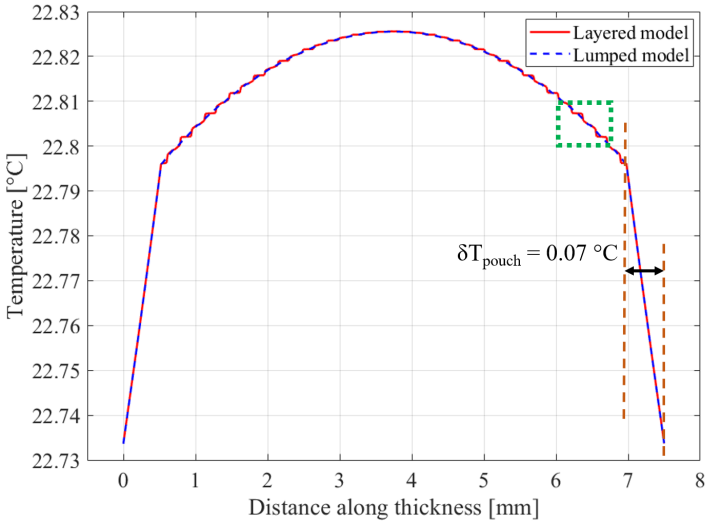

Figure 4.3: Temperature distribution comparison between the layered and the lumped models

ambient conditions. Since the pouch was the same in the layered and the lumped models, the temperature curve overlapped at those particular sections.

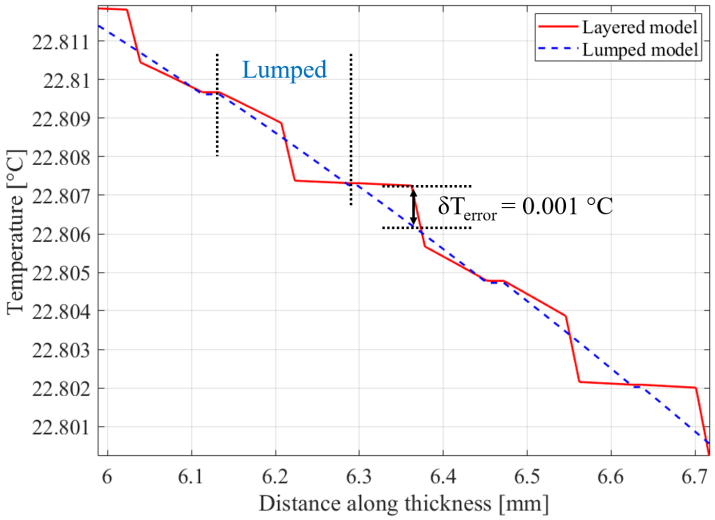

Figure 4.4: Magnified section of temperature distribution comparison between the layered and the lumped models from Figure 4.3

The lumped material replaced the individual layers as described in section 3.2.2.2. Hence, the temperature distribution between a set of Cu and Al current collectors varied. In case of the lumped model, it was a continuous curve represented by the blue dashed line in Figure 4.4 as the material was the same between the considered set (unit cell) of Cu and Al current collectors. However, since the layered unit cell had all individual layers (cathode, separator and anode) with their own material properties, the drop in temperature was different across each layer. For example, the sudden nearly vertical drop is from the separator due to its lower thermal conductivity and it contributed to the maximum possible error (δT=0.001 °C) between

the layered and the lumped modeling approaches.

Therefore, the acceptance of the lumped approach depends on the level of accuracy expected for the considered application. The layered approach nearly emulates the real arrangement and provides the accurate temperature at every μm depth while the lumped approach provides an accurate temperature at nearly every 154.5 μm. Since the maximum difference in the temperatures can be a mere 0.001 °C, the lumped model is considered appropriate in the present work as the computational effort and time saved outweigh the third decimal accuracy loss. The following unit cell, full cell, pulse test and the cooling system use accuracy up to two decimal in temperatures.

4.2 Unit Cell

Section 3.2.5.1 described the simulation set-up considered for the below set of simulations. For a unit cell, only steady-state simulations were carried out to verify the electrical arrangement and temperature distributions across the volume without considering the pouch material. As the electrical conductivity is a temperature dependent property, its effect on heat dissipation is studied and analysed in subsequent sections.

4.2.1 Steady-State

A constant current of 52/38 A which is equivalent to 2C for a single unit cell resulted in slightly different temperature distributions for the case with constant electrical conductivity and temperature dependent electrical conductivity. The heat loss (P_{unit}, P_{loss}) presented in the following cases are obtained by the integration of volumetric heat release (W/m^3) from the entire unit cell volume which included the Cu current collector, the Active lumped material and the Al current collector. In addition, the heat transfer coefficient taken was $10/38\,\mathrm{W/m^2 \cdot K}$ as elaborated in section 3.2.5.1. For the sake of convenience and ease of comparison between the following cases, same color scale is used for the heat distributions in the results below.

Case 1 : Constant Electrical Conductivity

With a constant electrical conductivity for the current collectors and active material (calibrated), the heat dissipated due to the flow of current $I_{unit} = 52/38$ A resulted in a heat loss of $P_{unit} = 0.213\,12$ W. Consequently, the resistance of a unit cell R_{unit} is calculated as below.

$$R_{unit} = \frac{P_{unit}}{I_{unit}^2} = \frac{0.21312}{(52/38)^2} = 113.81\,\mathrm{m\Omega} \tag{4.1}$$

As depicted in Figure 4.5, the lower section of the unit cell seems to have a higher level of temperature uniformity and lower magnitude than the upper. This is due to the fact that the charges follow the shortest part between terminals when the resistance is the same throughout due to constant electrical conductivity.

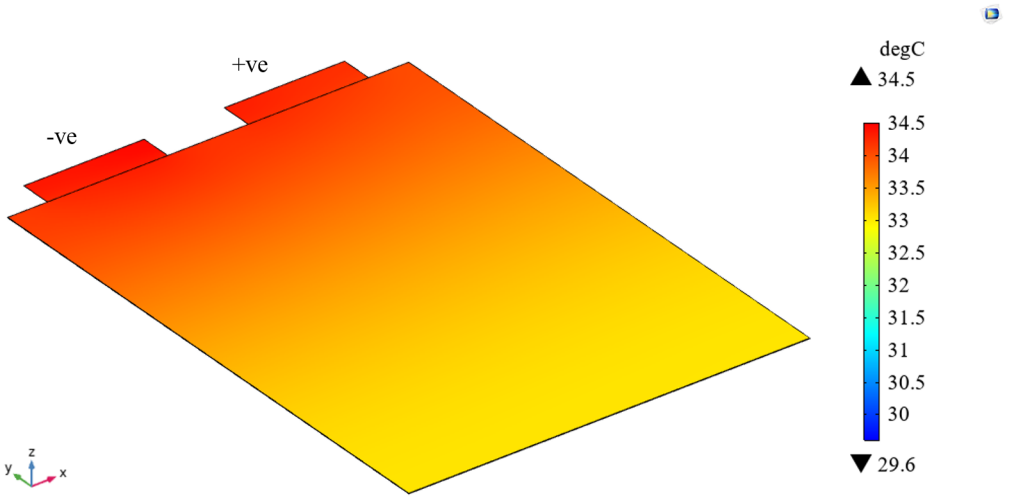

Figure 4.5: Unit cell temperature distribution with constant electrical conductivity

Case 2 : Varying Electrical Conductivity

When the case with varying electrical conductivity was simulated with the same boundary conditions as in Case 1, a slightly lower heat loss of $P_{loss} = 0.161\,19\,\mathrm{W}$ was observed. The corresponding temperature dependent resistance $R_{unit}(T)$ is calculated as,

$$R_{unit}(T) = \frac{P_{unit}}{I_{unit}^2} = \frac{0.16119}{(52/38)^2} = 86.08\,\mathrm{m\Omega} \tag{4.2}$$

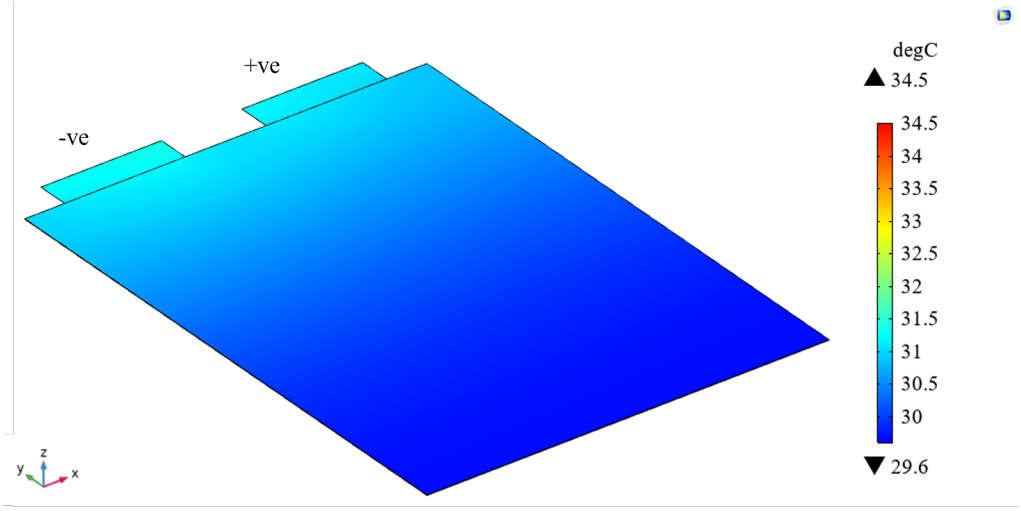

Figure 4.6: Unit cell temperature distribution with varying electrical conductivity

Similar to Case 1, the temperature distribution is relatively uniform at the lower sections as opposed to the upper section near and around the current collector projections as displayed in Figure 4.6. The charges following a path of lower resistance which in this case happens to be near the upper end of the unit cell as the increase in the temperature reduces resistance around the upper area.

As can be seen from Figure 4.5 and Figure 4.6, the nature of temperature distribution looks similar but the magnitude of temperate reached is different. In Case 1 with constant electrical conductivity of 0.048 S/m at 20 °C, the heat generated remains constant. Consequently, as the steady-state temperature is reached, its heat generation is still based on the reference conductivity of 0.048 S/m which is applied for all temperatures. In contrast for Case 2 with temperature dependent conductivity which increases with an increased rate of active material chemical reactions providing free charges, relatively lower heat is generated. Therefore, the temperature range in Figure 4.5 is higher (between 33 and 34.5 °C) than in Figure 4.6 (between 29.6 and 31.5 °C) because of R_{unit} reduction by 24.37 % in unit cell in Case 2. Hence, ignoring the temperature dependence parameter in the present study could impose an error in the resistance of up to 32.2 %, which led to the temperature extreme range differences mentioned above.

4.3 Full Cell

The simulation setup from section 3.2.5.2 described the procedure followed in the full cell simulations. This section deals with the entire cell, its volumetric temperature distribution for similar cases as the unit cell in the preceding section.

4.3.1 Steady-State

Similar to the unit cell simulations, a steady current of 2C i.e., $I_{cell} = 52\,\text{A}$ was used. Again, two cases were simulated, one with the constant electrical conductivity and the other utilising temperature dependent electrical conductivity. Similar to the section 4.2, the heat loss (P_{cell}) presented in the following cases are also computed by the integration of volumetric heat release (W/m^3) from the entire cell volume which included the Cu current collector, the Cu tab (-ve), the Active lumped material, the Al current collector, the Al tab (+ve) and the pouch though it did not generate any heat as no current flowed through it.

Case 1 : Constant Electrical Conductivity

With the calibrated electrical conductivity of 0.048 S/m at 20 °C, when simulated at a constant current of 52 A, the heat dissipation rate of $P_{cell} = 8.1918\,\text{W}$ was observed and the corresponding cell resistance R_{cell} was computed as,

$$R_{cell} = \frac{P_{cell}}{I_{cell}^2} = \frac{8.1918}{52^2} = 3.02\,\text{m}\Omega \tag{4.3}$$

When compared with (4.1) for R_{unit} in Case 1, the relation can be clearly established that all the unit cells are connected in parallel within a full cell. The below calculation proves the same as each of the 38 unit cells behaving as a sub-resistor amount to the overall cell resistance.

$$R_{cell} = \frac{R_{unit}}{unit\ cells\ in\ parallel} = \frac{113.81}{38} = 3\,\text{m}\Omega \tag{4.4}$$

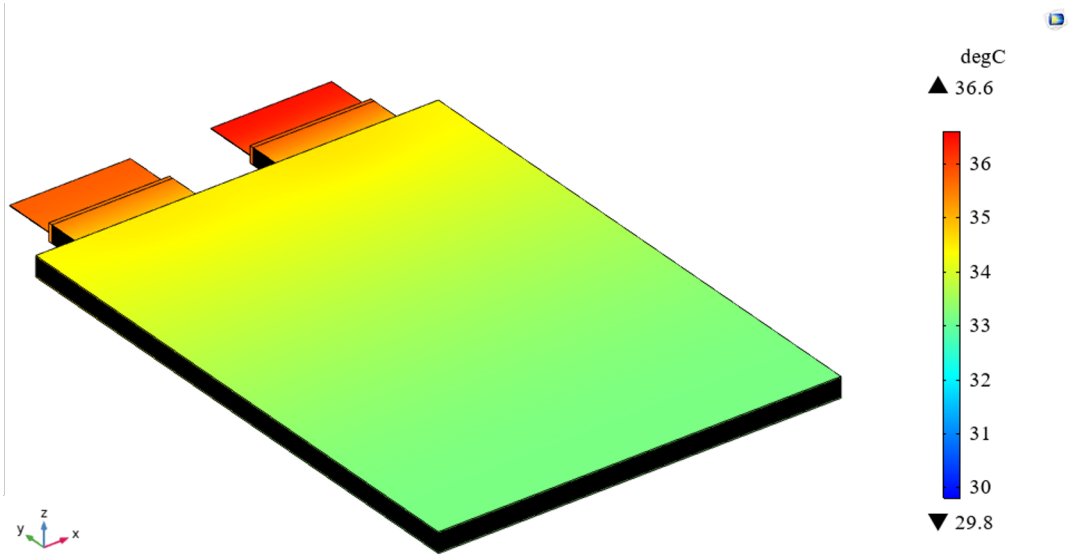

Figure 4.7: Full cell temperature distribution with constant electrical conductivity

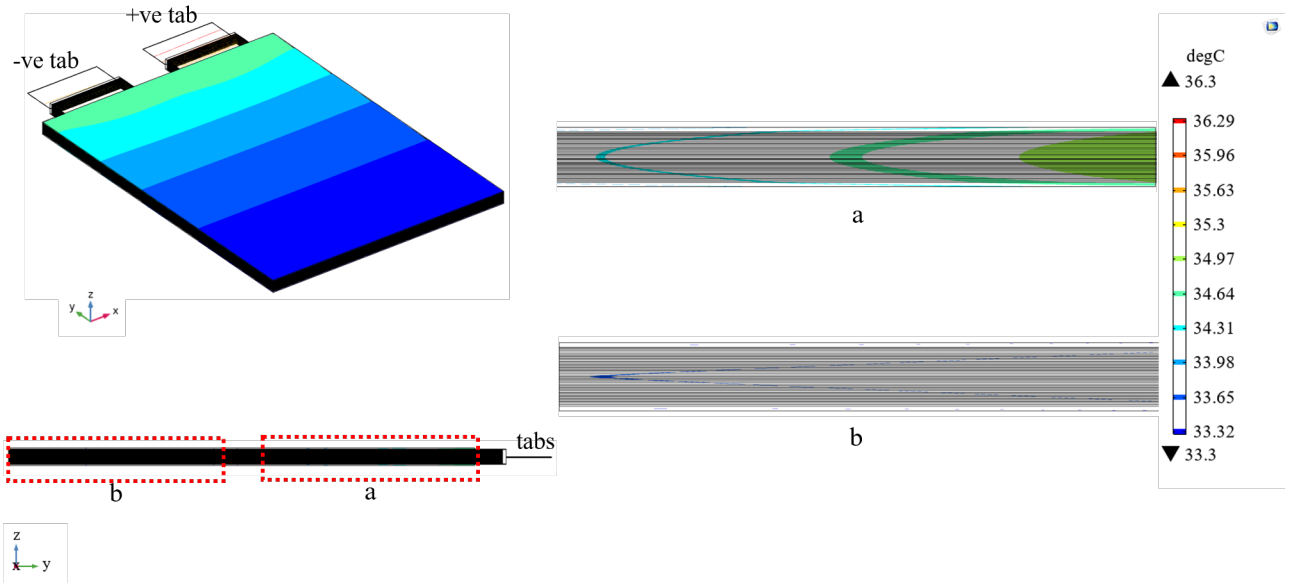

Figure 4.8: Full cell isothermal contours inside the cell with constant electrical conductivity

As shown in Figure 4.7, higher temperatures are observed near the +ve tab and upper sections of the cell as opposed to the lower. This is justified because the charges prefer the shortest path and path of least resistance. The reason for the higher temperature of the +ve tab is due to the material used in the +ve current collectors and its respective tab. Due to the aluminum's higher specific thermal capacity and lower electrical conductivity, it heats up more for the cross-section used in the presented case. Axiomatically, the Cu tab is relatively at a lower temperature due to its lower specific heat capacity and higher electrical conductivity hence generating lower heat for the same charge/current flow. Figure 4.8 illustrates the isothermal contours within the cell thickness. Due to a higher quantity of charge

flow at the upper sections near the tabs, more temperature inhomogeneities are observed as opposed to the lower cell part. It is also to be noted that the color scale for the temperatures in Figure 4.7 is different from Figure 4.8.

Case 2 : Varying Electrical Conductivity

Varying electrical conductivity as shown in Figure 3.13 for the full cell constituents is integrated into the model and simulated similar to Case 2 in the unit cell simulations. Evidently, due to the increased temperatures during operation, the electrical conductivity of the active material increases while that of the metal current collectors decreases. But, the total heat generated $P_{cell} = 6.3134\,\mathrm{W}$ is less than the model with constant electrical conductivity described in Case 1. The cell resistance $R_{cell}(T)$ which is inversely proportional to the electrical conductivity, is dependent on temperature and hence calculated as,

$$R_{cell} = \frac{P_{cell}}{I_{cell}^2} = \frac{6.3134}{52^2} = 2.33\,\mathrm{m\Omega} \tag{4.5}$$

When comparing with (4.2) for R_{unit} in Case 2, the temperature dependent electrical conductivity has increased leading to a lower unit cell resistance. As shown in Case 1, all 38 unit cells are connected in parallel and the full cell resistance calculation proves the same.

$$R_{cell} = \frac{R_{unit}}{unit\ cells\ in\ parallel} = \frac{86.08}{38} = 2.3\,\mathrm{m\Omega} \tag{4.6}$$

The difference of $0.03\,\mathrm{m\Omega}$ between (4.5) and (4.6) is attributed to the meshing inaccuracies.

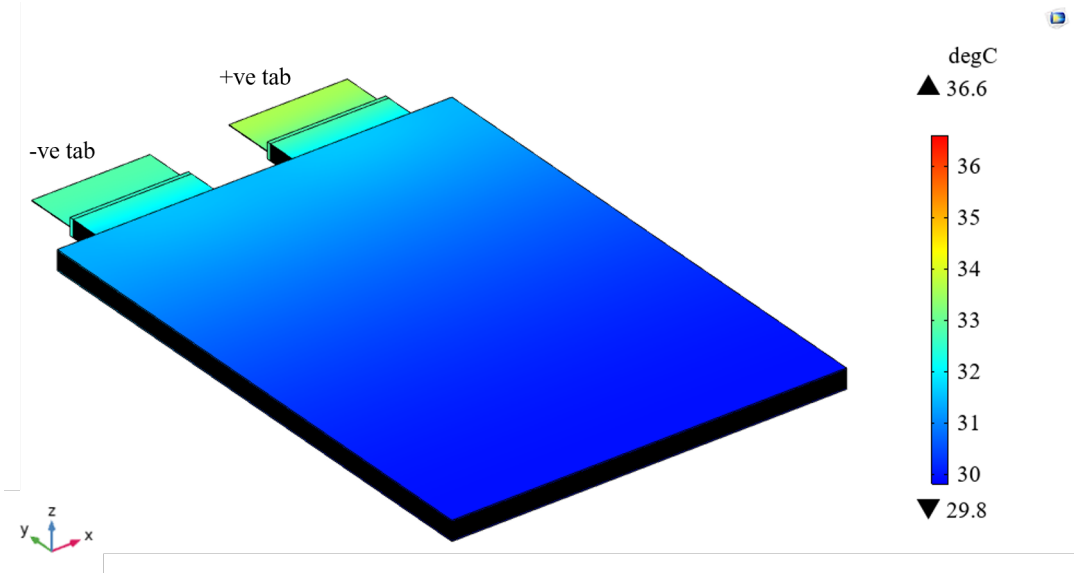

Figure 4.9: Full cell temperature distribution with varying electrical conductivity

As displayed in Figure 4.9, the temperature range is lower than that in Figure 4.7. This is due to the lower cell resistance in Case 2. As the temperature

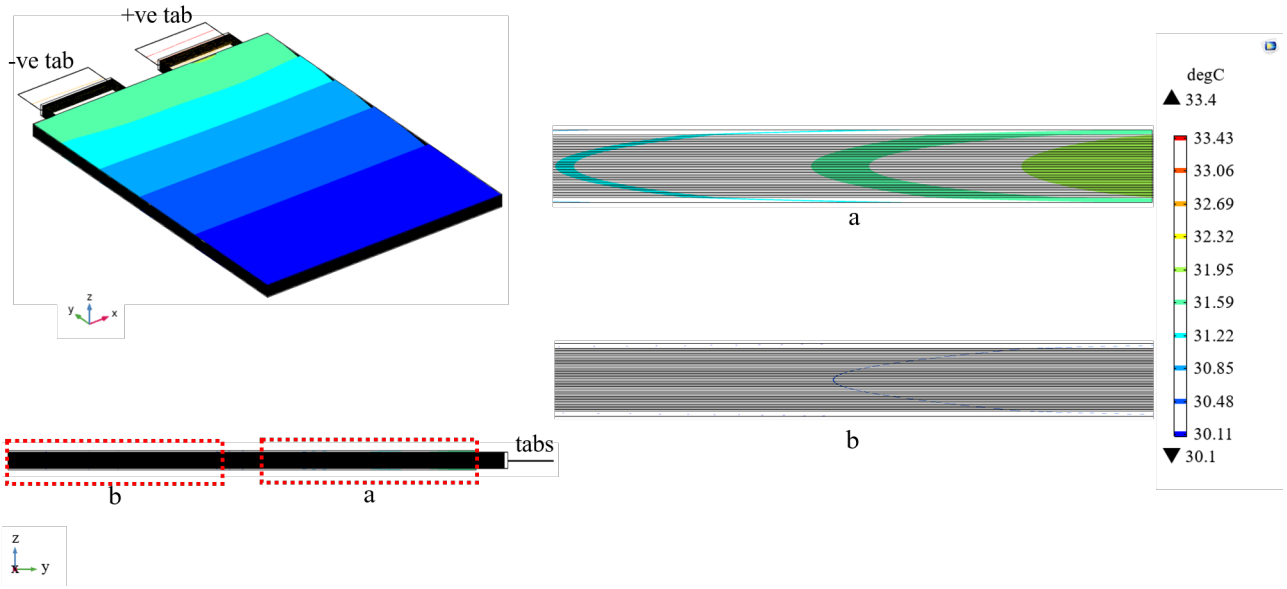

Figure 4.10: Full cell isothermal contours inside the cell with varying electrical conductivity

increases, the active material's conductivity increases hence reducing its individual resistance. Though an increase in temperature reduces the current collector electrical conductivity, it is not of such a significant magnitude as that of active material. Since active material is characterised by the chemical reactions providing the charge as a functional part of the cell, its contribution dominates and over-runs the current collectors' conductivity decrease. Approximately, a reduction in R_{cell} by 22.85% was observed for Case 2 against Case 1. The reason given in Case 1 for higher temperatures of the +ve tab when compared to the -ve tab applies here as well.

Isothermal contours represent the constant temperature trajectories within a cell volume and Figure 4.10 illustrates the same. It is to be noted that the color scale for the temperatures in Figure 4.10 is different from Figure 4.9. As explained in Case 1, the preference of charges to follow the path of least resistance justify the higher amount of temperature uniformities near the upper part of the cell when compared to the lower. Most of the experimental tests justify the higher temperature of the +ve tab and the upper surface when compared to the -ve tab and the lower surface respectively. The upper and the lower surfaces referred here are based on the direction in the y-axis of the co-ordinate system.

4.3.2 Transient

The time dependent simulations are time consuming and require excessive computational power. Steady-state simulations can take a few minutes while transient simulations run for days as was the case in the present study. As specified in section 3.2.5.2, two cases were simulated to demonstrate and analyse heat distribution as a function of time for the respective nature of time dependent current load.

Case 1 : 2C

Since 1C current is required to discharge a fully charged cell in 1 hour, 2C would need 30 minutes to do the same. In the current case, 2C = 52 A is simulated to determine the steady temperature increase at different locations of interest in the study cell. The temperature probe locations are as shown in Figure 3.18. Independent time steps size were specified, which considered shorter steps at the beginning of the simulation with a gradual increase until the end.

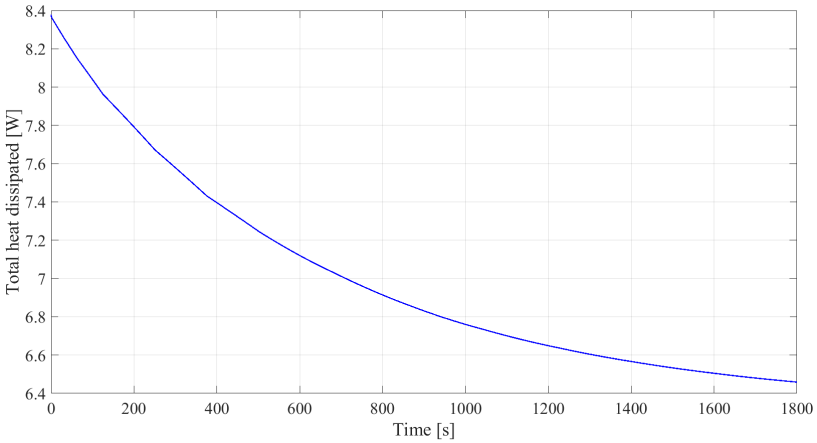

Figure 4.11: Total heat dissipated from the entire cell volume over time

Figure 4.11 shows the total heat dissipated from the entire cell volume over the entire 1800 s of operation. As it can be observed, heat dissipated at the start with the initial temperature as 20 °C is high at over 8.3 W while it reduces to just over 6.4 W at 1800 s as the increased temperature led to a reduction in the resistance hence lower heat.

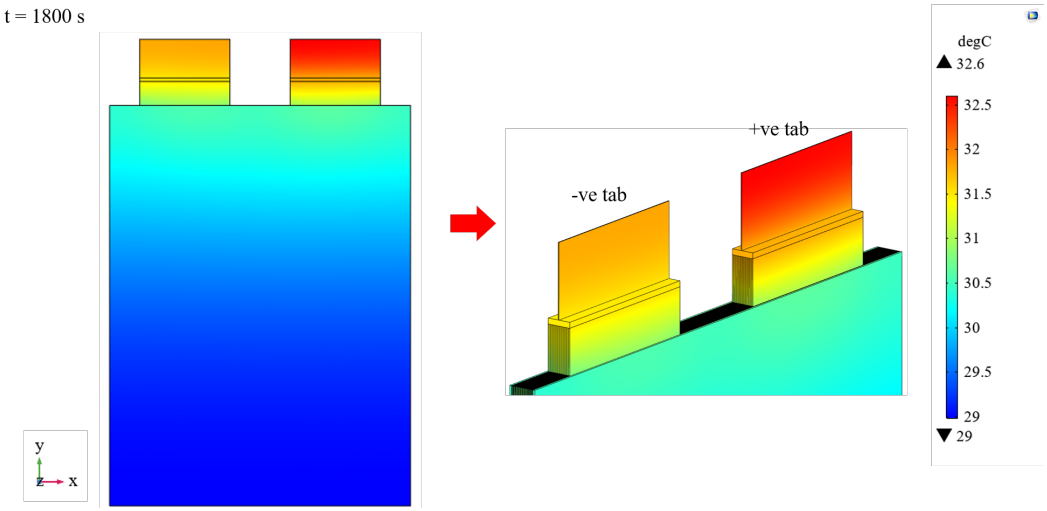

Figure 4.12: Temperature distribution on the front face and tabs at time instant 1800 s

Similar to the results in steady-state simulations, the +ve tab is observed to be at a higher temperature than the rest of the cell. As the charges flow through the cell

layers, the cross-sectional area for flow is much higher than at the tabs. As a result, the current density is more significant at the tabs contributing to the higher heat generation. Figure 4.12 illustrates the temperature distribution when the cell fully gets discharged. Since the reversible heat is higher at lower SoC and the present simulation does not account for it, the temperature reached is higher in the case of a real cell tested with similar boundary conditions.

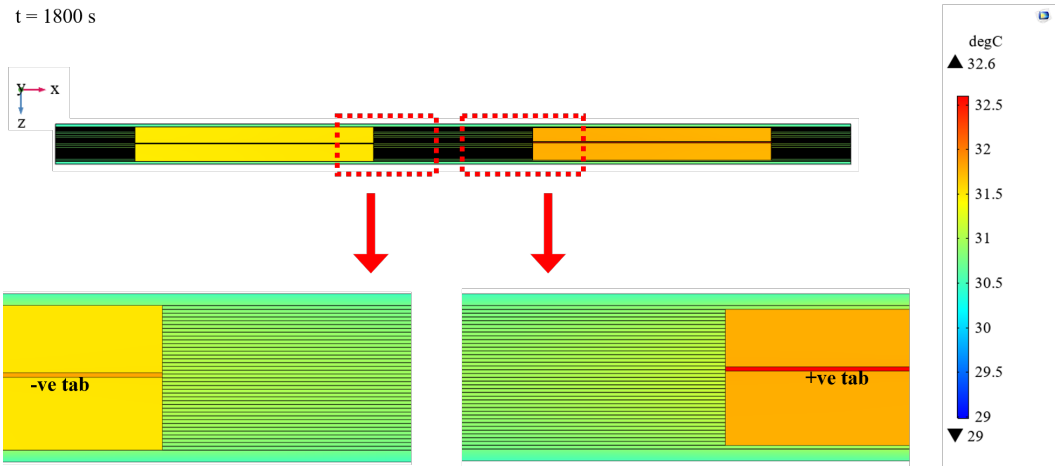

Figure 4.13: Temperature distribution in tabs and the region between them at time instant 1800 s

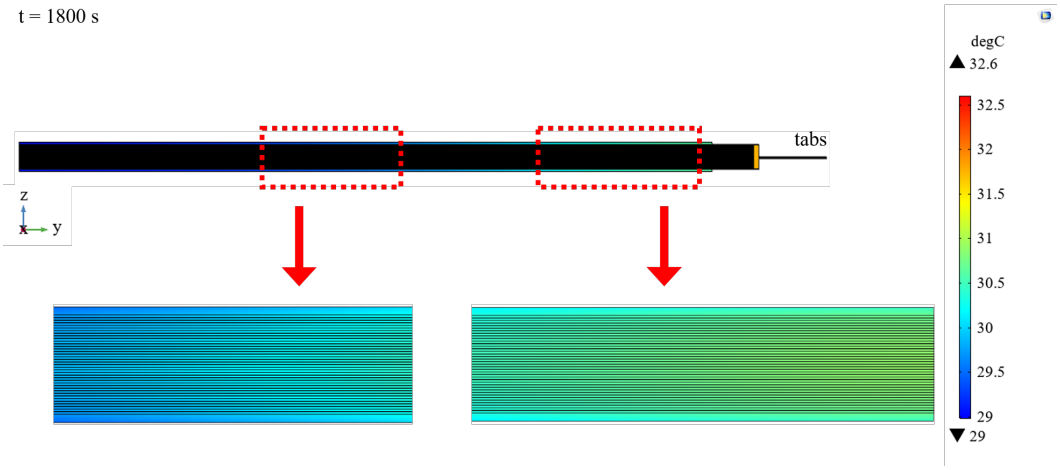

Figure 4.14: Temperature distribution along the length on lateral side at time instant 1800 s

Figure 4.13 and Figure 4.14 show the temperature distribution from top and side views respectively. The difference between the minimum and maximum temperatures is about 3.6 °C. This exists between the +ve tab and the bottom of the cell. However, for the active material nearest to the +ve tab, the temperature is around 31.25 °C while at the bottom is 29 °C leading to a difference of 2.25 °C. This difference causes uneven ageing in the cells as active material at higher temperature deteriorates faster than at lower temperature though it performs better at a reasonably high temperature.

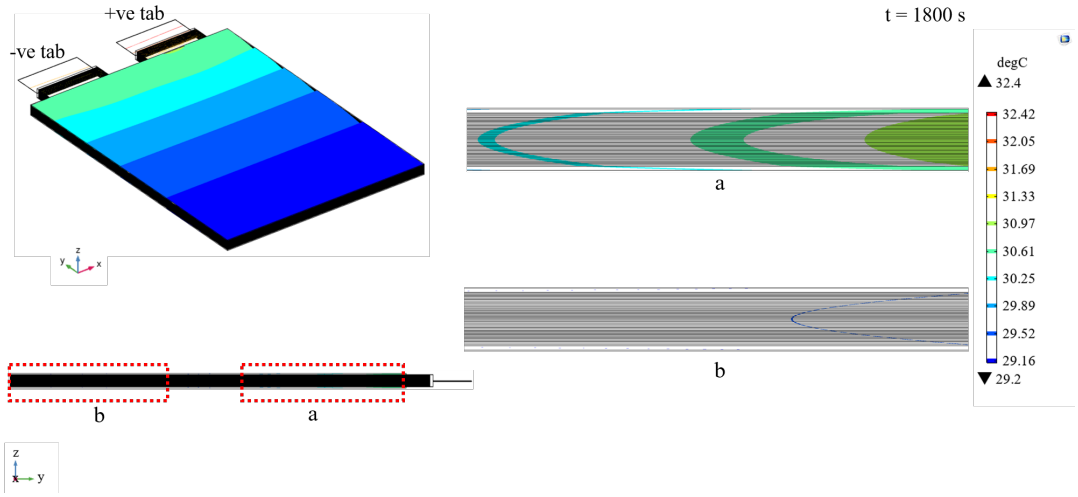

Figure 4.15: Isothermal contours throughout the cell volume at time instant 1800 s

From the isothermal contours in Figure 4.15, it is evident that the temperature variations are relatively higher at the upper half of the cell along its height (y-axis) when compared to the lower half. This is again due to charge flow preference to the path of lower resistance. Figure 4.15 a. and b. demonstrate this.

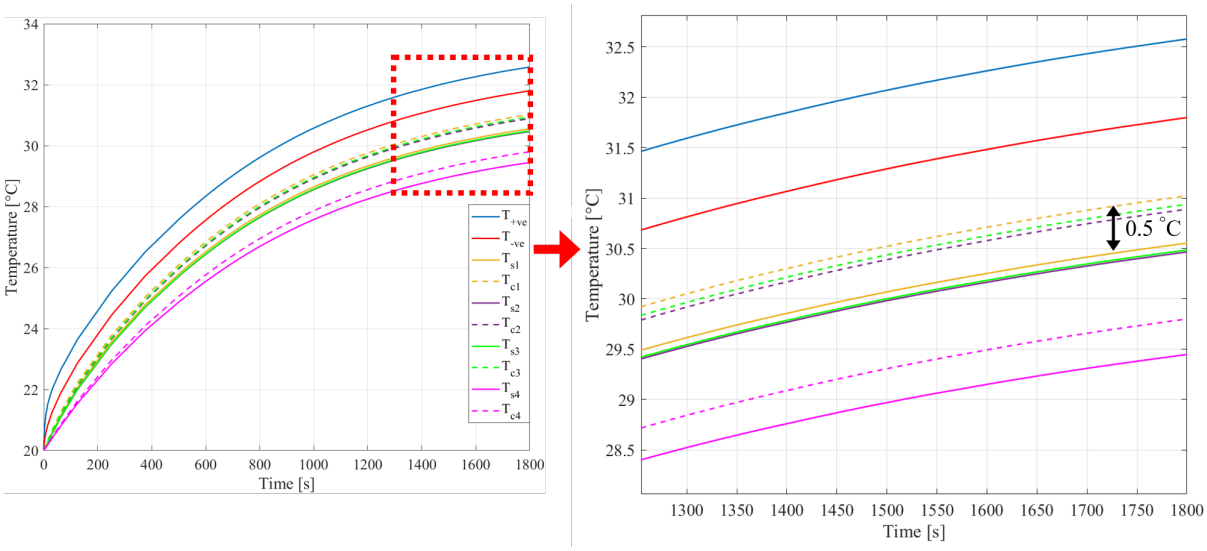

Figure 4.16: Temperature variation from 0 s to 1800 s at probes specified in Figure 3.18

The temperature increase with time is shown in Figure 4.16. As can be seen, by the end of 1800 seconds, different points are reaching their respective steady-state temperatures. The surface temperatures are evidently lower than at the core beneath same locations. A temperature difference of 0.5 °C was observed for the probes at the upper surface (T_{s1}, T_{s2}, T_{s3}) and core (T_{c1}, T_{c2}, T_{c3}). However at the cell centre, the temperature difference was 0.3 °C between T_{s4} and T_{c4}.

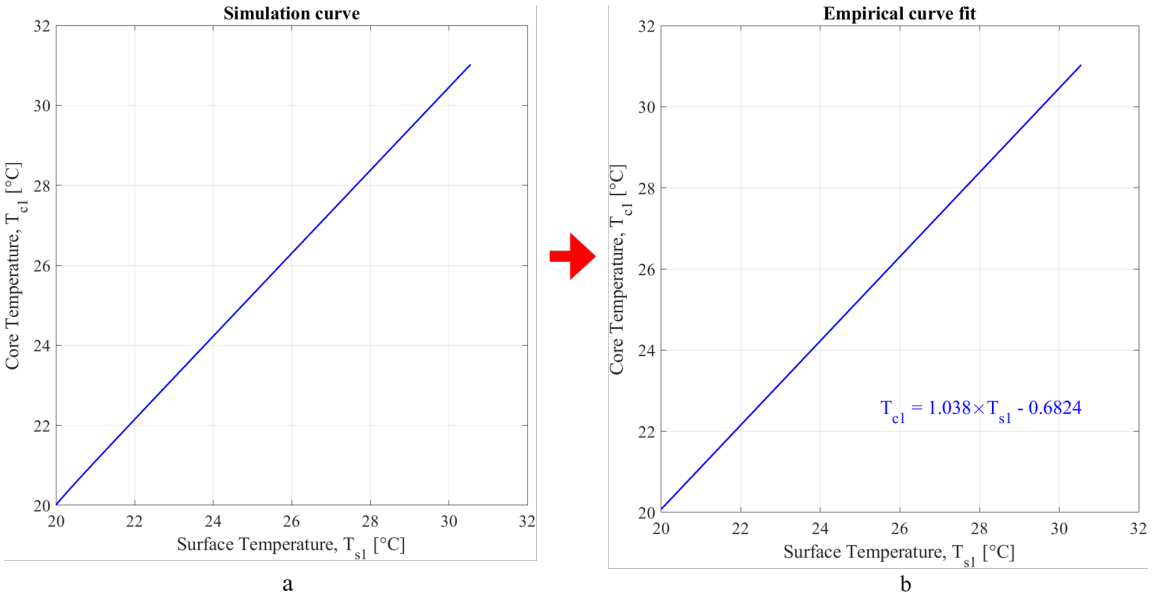

Figure 4.17: 2C current plot for core temperature variation against surface temperature from (a). Simulation results and (b). Corresponding empirical fit curve with equation

Figure 4.17 b. relates the surface temperature and core temperatures empirically providing the underlying equation. It can be observed that for each value of T_{s1}, there is a corresponding value of T_{c1}, which is marginally more than T_{s1}, except for first few seconds when it is almost the same. The maximum difference reached is 0.52 °C.

Case 2 : WLTC

Using the same boundary conditions as in the previous case but with the replacement of current profile as computed in section 3.2.5.2 and displayed in Figure 3.21, the following temperature distribution was obtained at the end of 1800 s.

Figure 4.18 shows the total heat dissipated from an entire cell volume over the duration of 1800 s of operation. As it can be noted, the nature of heat dissipation varies similarly as the single cell current flow for the WLTC as shown in Figure 3.21. Since only the joule heat is considered assuming operation at high SoC, the total heat generated is exothermic throughout the entire duration of 1800 s.

Between $t = 1450$ s and $t = 1600$ s in the WLTC, the vehicle speed gain is high and hence a high acceleration region is observed. This leads to a higher current being drawn from the batteries resulting in excess heat generation. The instant of highest temperature of 22.5 °C is at $t = 1571$ s as shown in Figure 4.19. As reasoned in the previous case, the +ve tab is bound to be at a higher temperature than the -ve tab due to the Aluminum's lower electrical and thermal conductivities than Copper.

Figure 4.20 and Figure 4.21 show the temperature distribution from the top and side views respectively at $t = 1571$ s. The difference between the minimum and maximum temperatures is about 1.9 °C which exists between the +ve tab and

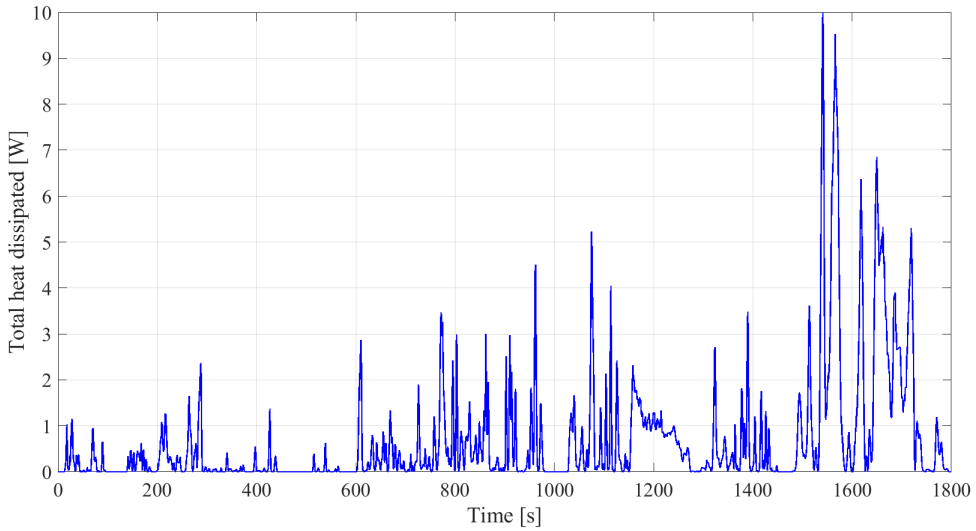

Figure 4.18: Total heat dissipated from the entire cell over time

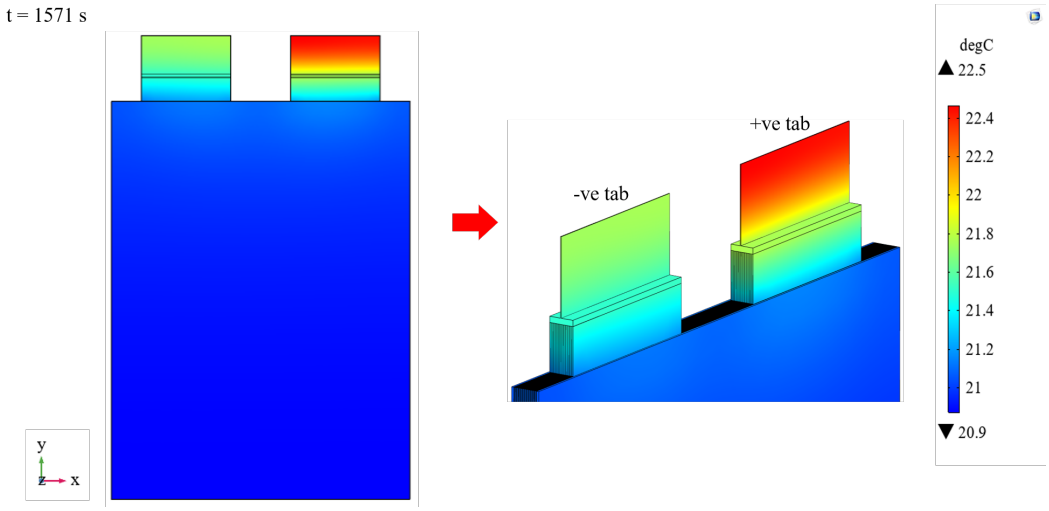

Figure 4.19: Temperature distribution on the front face and tabs at time instant 1571 s

the bottom of the cell. But, for the active material nearest to the +ve tab, the temperature is around 21.3 °C while at the bottom it is 20.9 °C leading to a difference of 0.4 °C. When comparing with the previous case which could be equated to a drive cycle with an acceleration higher than what is found in the WLTC, the difference is smaller leading to lower the amount of temperature inhomogeneity for the WLTC.

As shown in Figure 4.22 a., the blue contour is nearer to the tabs and the temperature is almost uniform below the contour maintained at 21.03 °C. From the initial state at 20 °C a rise of only 1.3 °C is seen until $t = 1571$ s due to the less aggressive nature of WLTC. While in figure Figure 4.22 b. which displays contours at the end, the temperature distribution is relatively less uniform based on the heat dissipation from the surface as the heat generation reduces in the latter part of WLTC. The 'U' shaped contours when seen from the y-z plane confirm the non-

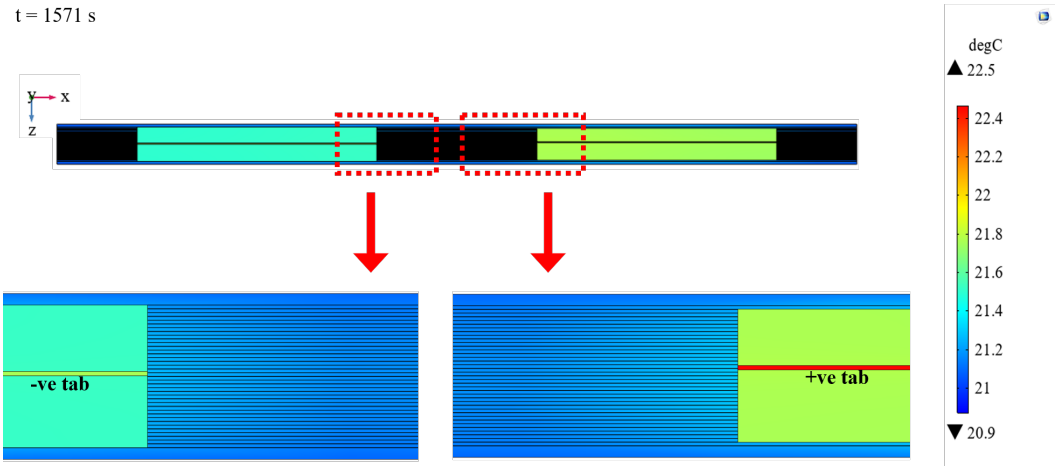

Figure 4.20: Temperature distribution in tabs and the region between them at time instant 1571 s

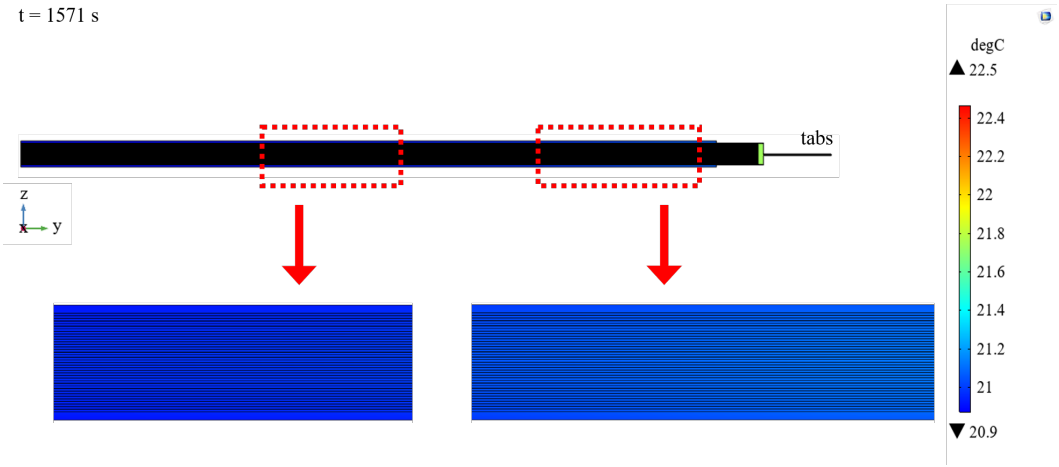

Figure 4.21: Temperature distribution along the length on lateral side at time instant 1571 s

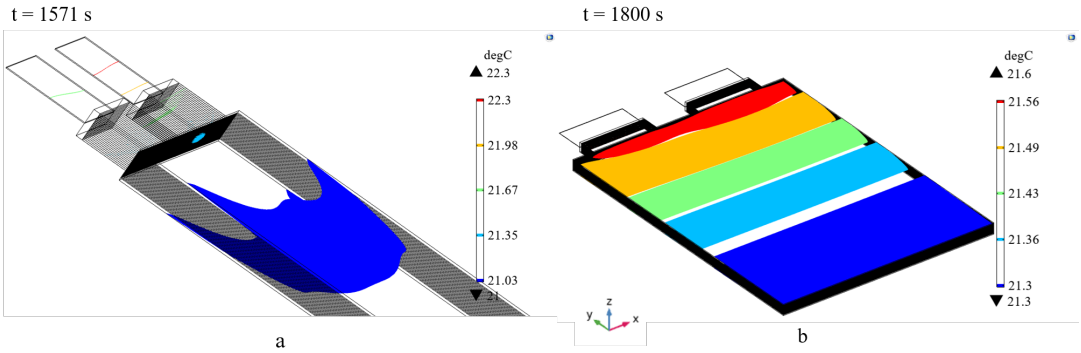

Figure 4.22: Isothermal contours throughout the cell volume at (a). 1571 s and (b). 1800 s

linear temperature distribution and hence inhomogeneity though less than 1.5 °C for WLTC.

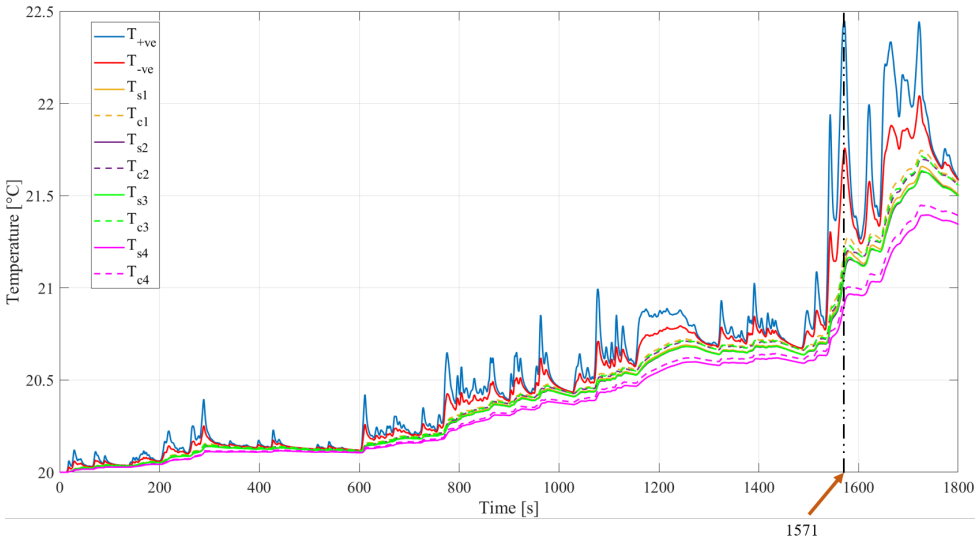

Figure 4.23: Temperature variation from 0 s to 1800 s at probes specified in Figure 3.18

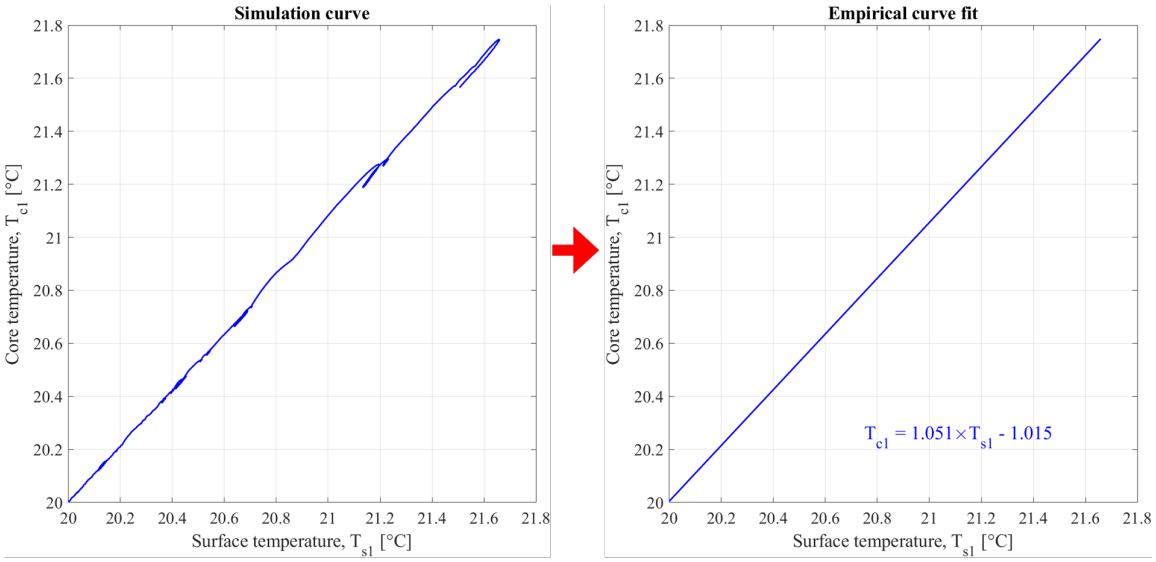

Figure 4.24: WLTC current plot for core temperature variation against surface temperature from (a). Simulation results and (b). Corresponding empirical fit curve with equation

Similar to the previous case, the temperature probes on the surface and the core are recorded for each time step until 1800 s. Figure 4.23 represents the same. As can be seen, the overshooting of the +ve tab is due to the aluminum's lower thermal conductivity and its lower electrical conductivity as opposed to the Copper leading

to more localised heat generation than the Cu at the -ve tab. Yellow, purple and green curves represent the temperatures at the upper part of the cell where higher temperatures are observed due to their closer vicinity to the tabs and forming a path of low resistance. However, the pink curve shows the lower temperatures throughout the drive cycle as it is at the cell's geometric centre, further away from the tabs. The dashed curves give the profile of the probes at the core (T_{c1}, T_{c2}, T_{c3}) and are undoubtedly at higher temperatures than the corresponding surface probes (T_{s1}, T_{s2}, T_{s3}) due to the existence of the thermal resistance from the core to the surface caused by the low thermal conductivity of the lumped active material and the pouch material. For the entire WLTC, at time instant 1571 s, the highest temperature is recorded on +ve tab due to high acceleration demand.

Figure 4.24 b. relates the surface temperature and core temperatures empirically providing the underlying equation for the WLTC. Similar to the 2C current results, it can be observed that for each value of T_{s1}, there is a corresponding value of T_{c1} which is marginally more than T_{s1} except for first few seconds when it is almost the same. The maximum difference reached was a mere 0.1 °C.

4.3.3 Pulse Test

As described in section 3.2.5.3, with considered boundary conditions simulations were run. Initial steady-state simulations resulted in the calibration of the model towards the test room's heat transfer coefficient and thermal contact resistances. Then, transient pulse test simulations were used to compare and relate the deviations from the experimental results.

4.3.3.1 Steady-State Calibration

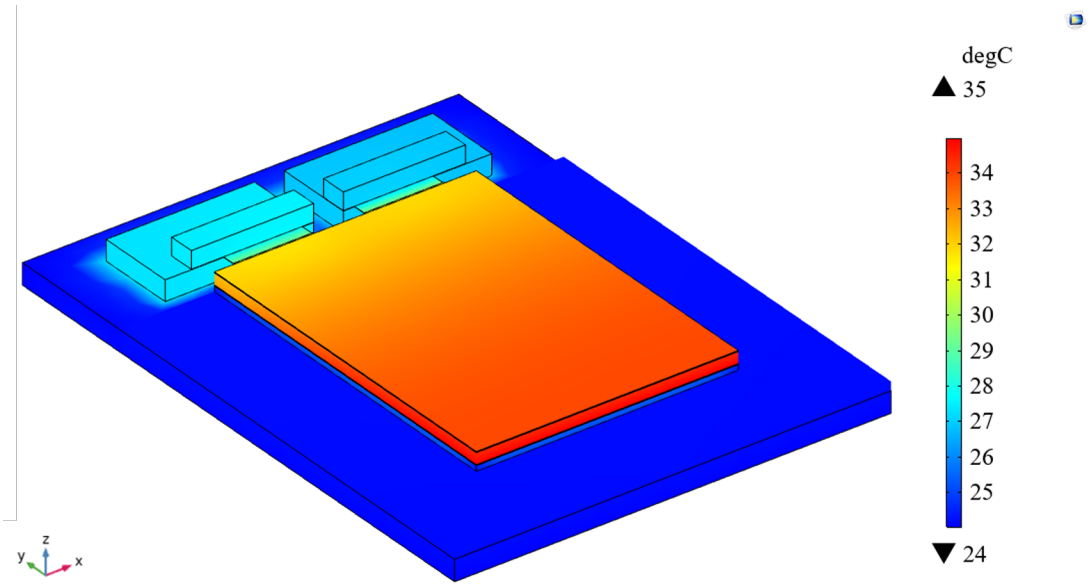

Figure 4.25: Temperature distribution in steady-state with 50 A current

With a constant heat source due to 50 A, the temperature distribution as shown in Figure 4.25 was obtained. It is contrary to see the higher temperatures reached near the lower cell surfaces than near the tabs. This is justified by the set-up used, as it ignores the heat flowing in from the copper cables near the brass bars and considers the heat loss/ambient cooling of brass bars hence acting as a heat sink to the upper section of the cell. The heat transfer coefficient was calibrated based on the steady temperature reached in experiments at cell centre (T_{centre}) and the + side ($T_{+\ side}$). The calibrated heat transfer coefficient was 20.23 $W/m^2 \cdot K$ and the same was used in pulse tests.

4.3.3.2 Pulse Tests : High and Low SoC

A pulse test is characterised by a constant current charge and discharge pulses with a specific frequency. In the present study, the pulse test at higher SoC was carried out at twice the frequency than at low SoC.

- High SoC

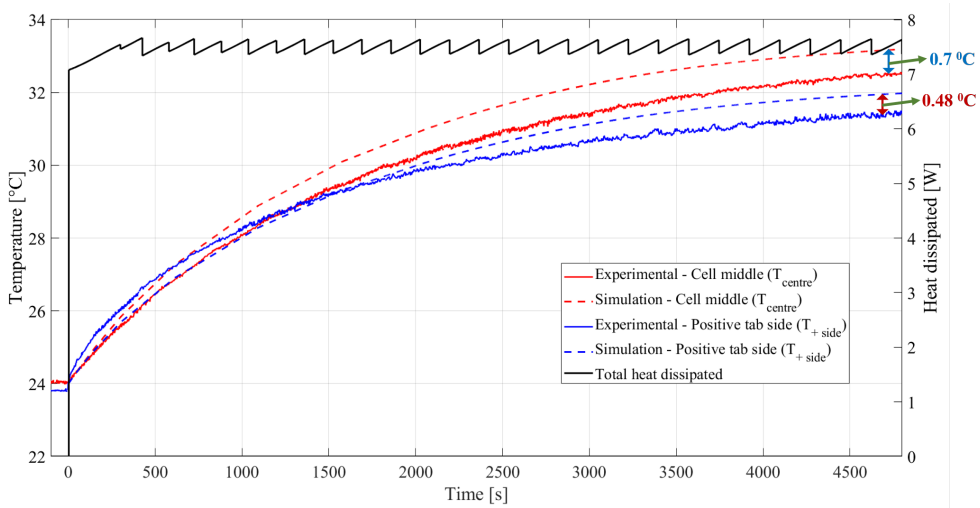

Figure 4.26: Cell surface temperature comparison between simulation and experiment for high SoC

Figure 4.26 shows the temperature increase and the total heat dissipated for the time from 0 s to 4800 s and is compared with experimental results. It can be inferred that the simulation temperature profile is nearly the same as the experiments at the cell centre and near the +ve tab side shown in Figure 3.22. Since the test is at high SoC and the reversible heat's effect is not considerable, the difference between the minimum and maximum heat dissipated is within 0.3 W. Therefore a gradual increase in temperature is observed rather than a temperature drop during the SoC decrease and when current changes direction during switching from charging to discharging and vice versa. The temperature deviations of 0.48 °C and 0.7 °C between simulation and experimental results at the + side probes and the cell centre respectively were observed. This deviation can be attributed to the approximation of thermal contact resistances between

the cell surface, cardboard and Al plate. However, the major observation to be considered here is the nature of simulation temperatures variation with the time which attest to the closeness and reliability of the model with the real test set-up.

- Low *SoC*

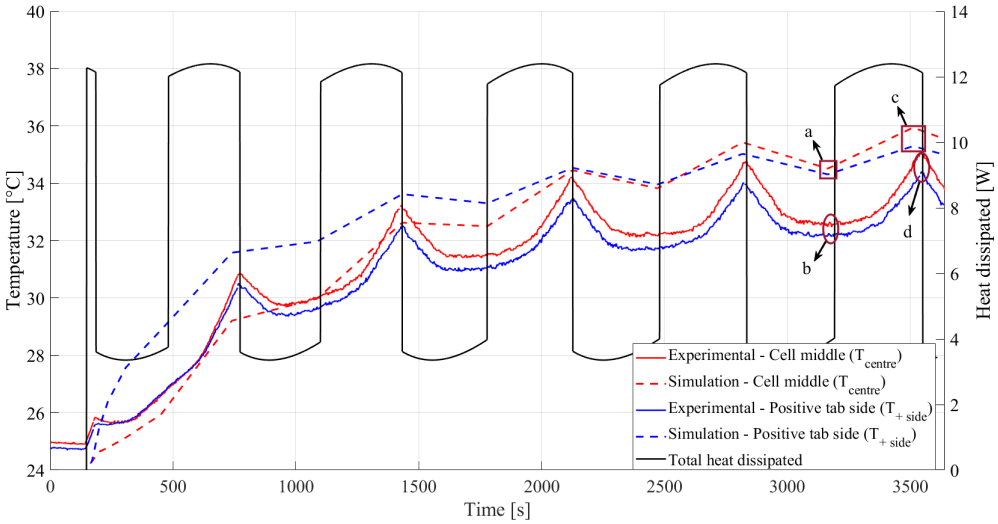

Figure 4.27: Cell surface temperature comparison between simulation and experiment for low *SoC* between simulation start and 3600 s (setup 2a)

Two separate time intervals were considered for the low *SoC* simulations since the experimental duration was longer than 10 hrs i.e., 36 000 s. The first setup, setup 2a was for initial ramp-up phase from the start at 0 s to 3600 s presented in Figure 4.27. The second setup, setup 2b was for time interval 10 140 s to 13 800 s which is the section after the ramp-up phase when the tab temperatures become almost steady and just the cell internal, surface temperatures vary as depicted in Figure 4.28.

As can be seen in Figure 4.27 (set-up 2a), the rise of temperatures for the simulation from 0 s to 3600 s follow a similar increase rate though the cell middle overtakes the + side after 2500 s. It can be seen that the temperature profile is characterised by peaks and troughs signifying the lower total heat generated during discharging at low *SoC* and higher heat generated during charging at low *SoC*. The total heat dissipated is shown by the black curve. It can also be observed that the simulation temperature troughs do not match precisely with the experimental counterparts due to the negligence of the dynamic effects and the presence of the meshing errors and thermal contact resistance approximations in considered simulation set-up. However, the peaks seem to be closer both for temperatures at the cell centre and + side. A deviation of 0.9 °C can be observed from the cell middle temperatures at 3500 s (regions c and d in Figure 4.27) representing peaks between simulation and experiments while deviation stands at 2 °C at 3172 s (regions a and b in Figure 4.27) which represents the troughs. Similarly, in case of the + side, the

difference in peaks (regions c and d in Figure 4.27) at similar time instants at the cell centre was 0.8 °C, but it remained as high as 2.1 °C at 3172 s trough (regions a and b in Figure 4.27).

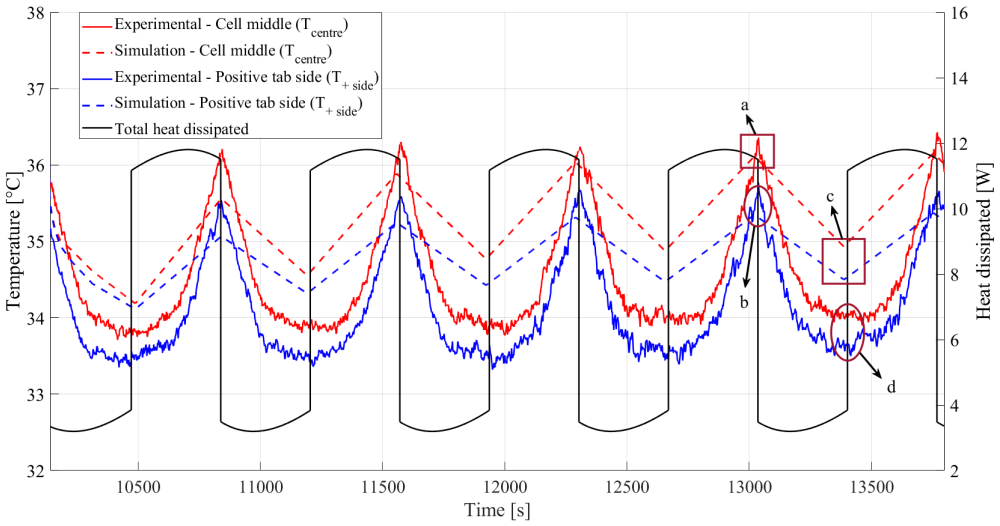

Figure 4.28: Cell surface temperature comparison between simulation and experiment for low *SoC* between 10140 s and 13800 s (setup 2b)

Figure 4.28 (setup 2b) displays the heat dissipated, the temperature profiles during the middle of test i.e., from 10140 s to 13800 s. In this separate simulation, initialisation temperature was specified being around 35.5 °C from the experiment. The trend followed by the simulation profile matched to the experiments with lower deviations when compared to the beginning simulation between 0 s and 3600 s representing ramp-up in set-up 2a. As can be seen, due to the negligence of the dynamic nature of the cell in the simulations, the temperature profiles follow a 'V' shaped curve while the experiment demonstrates 'U' shaped variations. At 13040 s (regions a and b in Figure 4.28) representing the crest, deviation at the cell centre and the + side was relatively low at 0.28 °C and 0.45 °C respectively. However, the difference was more at trough on 13390 s (regions c and d in Figure 4.28) for the cell centre at 0.95 °C and 0.95 °C at the + side. These differences were moderately lower than at previous sub-case studying initial phase from 0 s to 3600 s. The reasonable agreement in the overall nature of the temperature variations with time both for the experiment and the simulations justified the approximate reliance of the model while providing the potential for improvements in future studies.

4.4 Powertrain Cooling System

The cooling system model was run for 2C and WLTC cases considering the conventional VCR and enhanced VCR cooling systems. The boundary conditions remained the same except the control parameters which actuated the compressor and hence the cooling action described in section 3.3. For demonstrating the operation

of the powertrain cooling system, an initial temperature of 30 °C and start *SoC* of 95% were considered. Since the present work only considers the cooling system design and simulation of the powertrain, powertrain cooling system will be referred to as 'cooling system' in the following sections.

Case 1 : WLTC

The WLTC consists of an improved speed profile when compared to old NEDC with less aggressive speed variations presented following variations in parameters of interest. The corresponding relevant results extracted were the cell surface temperatures, compressor speed, refrigerant flow rate and *SoC* variations over time.

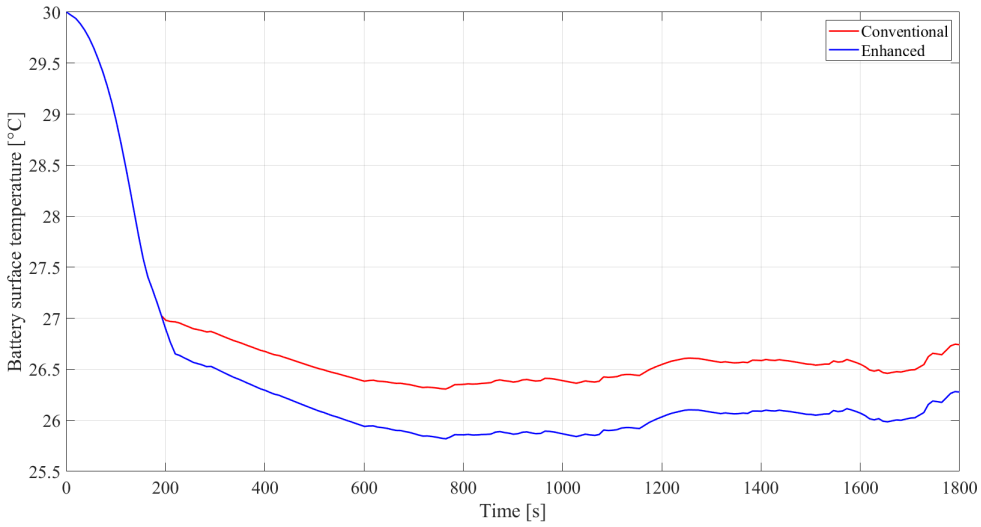

Figure 4.29: Cell surface temperature variation over time with the initial state at 30 °C

Since the threshold temperature specified in the battery TMS controller is 27 °C, the cooling begins at the start of the simulation and hence a continuous drop in temperature is observed from Figure 4.29. Near 200 s, the target temperature is reached for the conventional cooling system and therefore, the cooling system tries to maintain the battery surface at around the same range. This is depicted from nearly a horizontal red curve in Figure 4.29. However, as the enhanced cooling system uses cell core temperature as control parameter which is almost always marginally higher than the surface as discussed in previous sections, the cell is further cooled resulting in relatively lower surface temperature.

Figure 4.30 represents the compressor operation over the entire duration of the WLTC. As it can be observed from Figure 4.30(a)., the compressor is on from the beginning since the initial temperature is already above the target temperature. Nevertheless, the compressor in the conventional system turns off earlier compared to the enhanced cooling system as the target temperature is reached later in its case. The resulting refrigerant flow rate is as seen in Figure 4.30(b).

Figure 4.31 presents the *SoC* variation over the entire WLTC duration. Since the

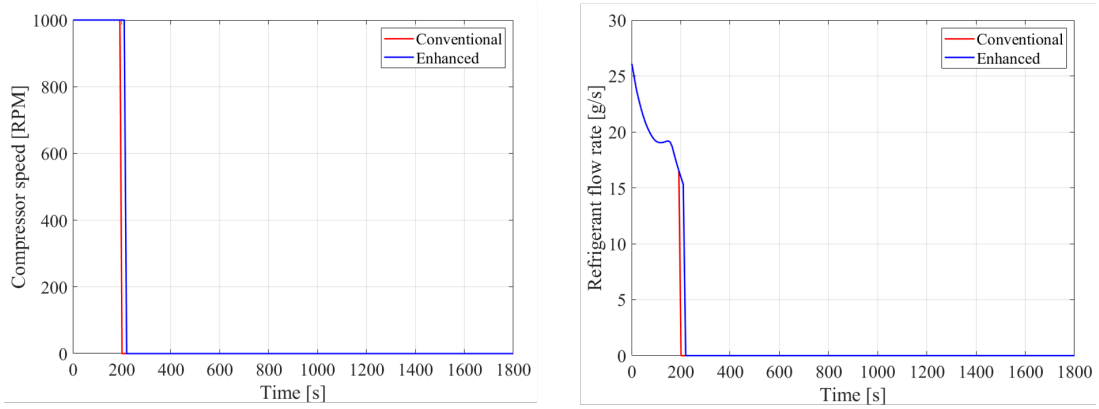

Figure 4.30: (a). Compressor speed variation over time and (b). Corresponding refrigerant flow rate

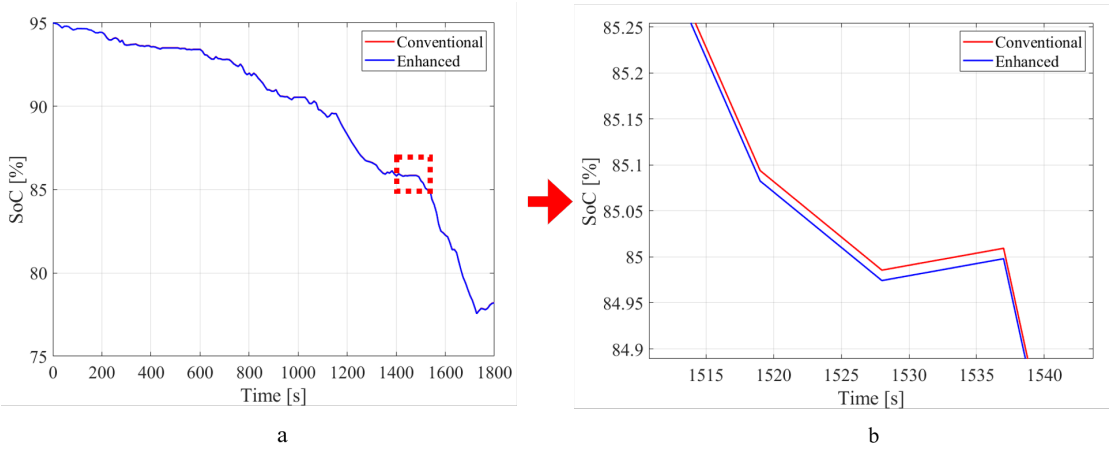

Figure 4.31: (a). Battery state of charge variation over time for WLTC (b). Magnified section of SoC variation

battery pack used in the current simulations is of relatively low energy at 23 kWh, the SoC drop of about 17.5% is plausible for the 23 km distance covered in this single WLTC from Figure 4.31 (a). As the conventional cooling system operates the compressor for a relatively shorter time, its SoC is marginally higher at specific time instants though not significant enough to consider in a single WLTC. It is shown in Figure 4.31(b).

Figure 4.32 shows the deviation of the battery cell average surface temperatures over the considered lower optimum of 27 °C. The mean temperature deviation for the conventional system was 0.24 °C while it extended to 0.65 °C for the enhanced system. However, the cell core temperature deviation in the case of the enhanced system was relatively lower at 0.3 °C. Hence, it can be observed that system improvements and optimisations using a well-calibrated cooling system controller could further reduce the deviations leading to effective temperature moderation.

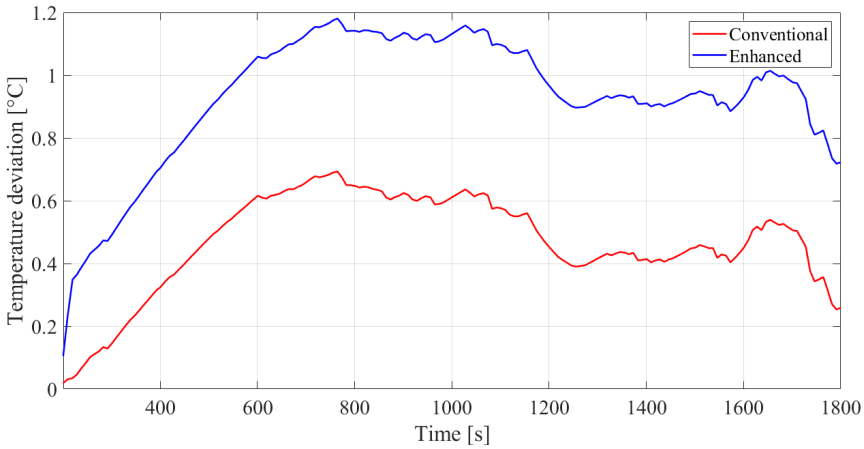

Figure 4.32: Deviation of battery temperature from considered lower optimum of 27 °C

Case 2 : 2C

A constant current of 2C accounted for high speed/rapid acceleration load on the battery. The relevant results extracted were the cell surface temperatures, compressor speed, refrigerant flow rate and *SoC* variations over time.

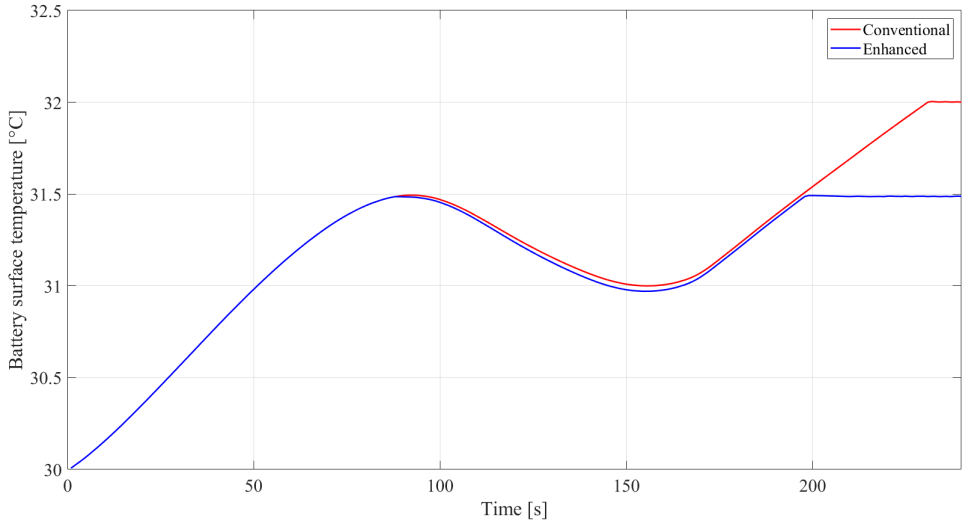

Figure 4.33: Cell surface temperature variation over time with initial state at 30 °C

Since the 2C current is run only for a short duration of 240 s; the same resulting temperature profile can be seen in Figure 4.33. Similar to the WLTC, due to an initial temperature of 30 °C, the surface temperature increases at a similar rate until about 90 s. Further, the deviation occurs and the conventional system transcends to maintain the surface temperature at 32 °C while the enhanced cooling system achieves 31.5 °C at 200 s. As the core temperature is typically at 0.5 °C higher than the surface for 2C, a surface temperature of 31.5 °C would relate to the core temperature of 32 °C which the conventional model reaches at around 230 s.

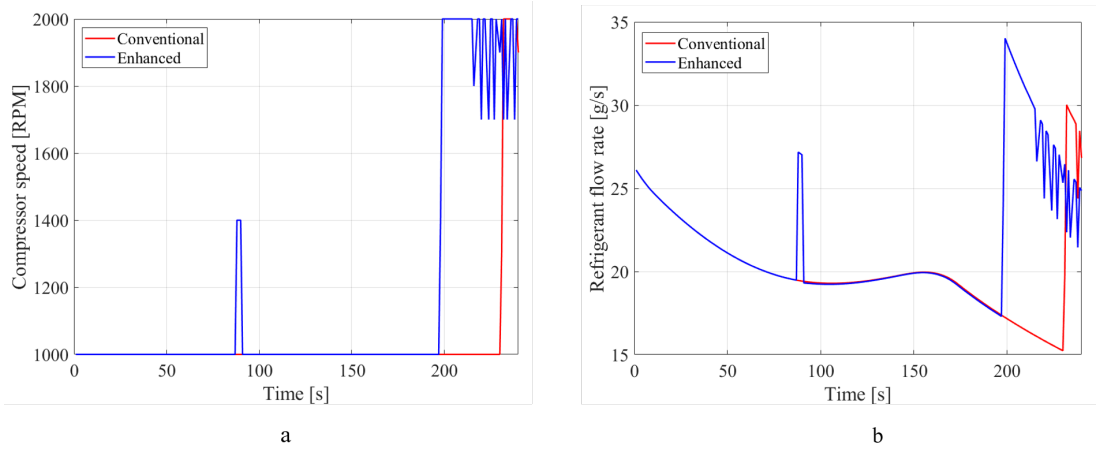

Figure 4.34: (a). Compressor speed variation over time and (b). Corresponding refrigerant flow rate

The enhanced cooling system turns up the compressor speed earlier than conventional as core temperature would have reached the threshold inducing compressor action. The same is observable in Figure 4.34(a). The corresponding refrigerant flow is triggered and represented in Figure 4.34(b). The compressor has a second threshold of 32 °C at 2000 RPM which explains the speed after 200 s and the temperatures attained in Figure 4.33.

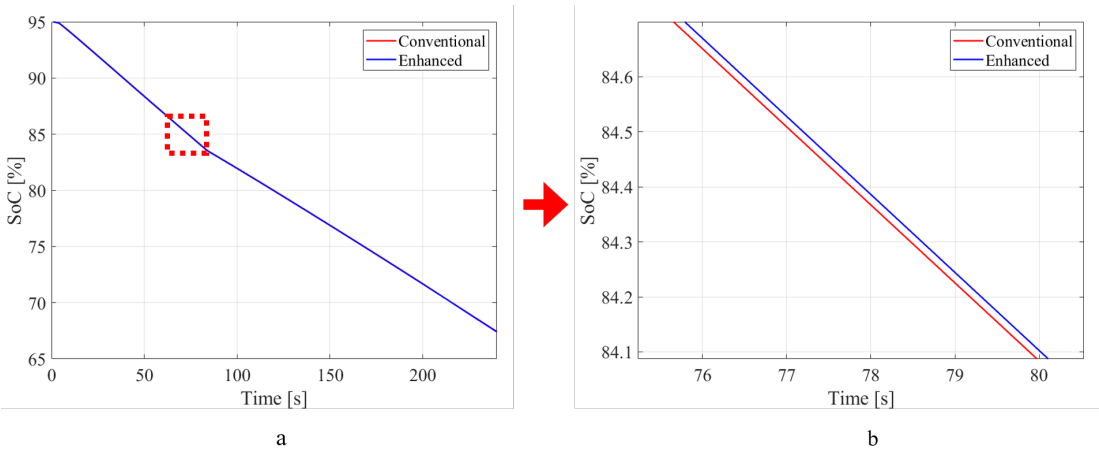

Figure 4.35: (a). Battery state of charge variation over time for 2C (b). Magnified section of SoC variation

A significant SoC drop of 27.5% is observed in a span of 240 s from Figure 4.35(a). High speed with no braking leads to no regeneration as can be noticed with the SoC increase intervals in Figure 4.31. Figure 4.35(b) gives a closer view of the SoC variation with the conventional system at a marginally lower SoC, which is contrasting to the operation modes of the compressor leading to higher a power consumption. A repetitive WLTC and 2C analysis could yield more considerable variations and help in inferring more certain results.

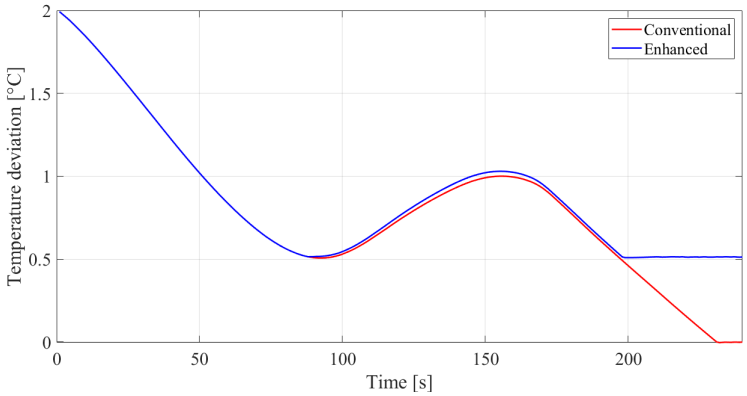

Figure 4.36: Deviation of battery surface temperature from considered higher optimum of 32 °C

Figure 4.36 shows the deviation of the battery cell average surface temperatures over the considered upper optimum of 32 °C. The mean temperature deviation for the conventional system was 0.8 °C while it extended to 0.87 °C for the enhanced system. But, the cell core temperature deviation in case of the enhanced system was relatively lower at 0.37 °C. Hence, it can be deduced that the system improvements and optimisations using well-calibrated cooling system controllers could further reduce the deviations leading to better temperature regulation and operation.

4.5 Discussion on Ethics and Sustainability

As the cost of EVs reduce and becomes comparable with that of conventional ICEVs, consumers face an ethical challenge about the choice of personal transport based on several factors. Eventually, though EVs may match and even become more affordable than the conventional vehicles, cost solely would not determine the customers' decision. In addition to the importance of battery recharging duration and the driving range, the sourcing of materials used in Li-ion batteries have brought some ominous facts into light. There have been reports questioning the sourcing of raw materials used in EV batteries such as Lithium, Cobalt and Manganese. The environmental effects of the indiscriminate mining and possible involvement of child labour in some locations have added specs of considerable doubt on the use of EVs from sustainability and morality standpoint.

Ultimately, it is going to come to the priorities of each individual purchasing an EV and the geographic region of its use with the locally available electrical energy sources. If the EV is recharged using electricity generated by coal-powered plants, then the extent of net carbon emissions and hence the degree of sustainability between EVs and ICEVs may become comparable. Moreover, the EV manufacturers will also have an ethical responsibility to collaborate with the battery and other component suppliers adhering to sustainable supply chain and traceability. As EVs become more common, even the customers can be familiarised with the legitimacy of material sources and the legal practices followed to develop a trusted relationship with the manufacturer.

Finally, concerning the present work, proper thermal management of the batteries could not only reduce the risk of battery fires for passengers but may also potentially help in extending the service life based on the future studies on ageing. Hence for the EV manufacturers', addressing the ethical responsibility of delivering the safest possible vehicles along with the sustainable sourcing and net-zero carbon vehicle development have continued to move up the priority order over recent times and will ultimately drive the future development of personal and commercial mobility solutions.

5
Conclusion

With all the simulations results obtained and analysed with available experimental results, a few important inferences were made and conclusions were drawn. For the remainder of the observations and anomalies, an in-depth study was necessary and hence presented the scope for the interesting future works.

5.1 Present Work

The current study demonstrated the multi-physical approach of modeling a 3-D Li-ion pouch cell of a known volume and sub-component properties. Though the mechanical part was not considered and the chemical section was included partially with a separate 1-D electro-chemical simulations, the resulting electro-thermal model with chemical domain integrated demonstrated reliable results and corresponded with experimental tests with acceptable deviations. The present methodology employed also proved the level of detail that can be used by creating a lumped active material with equivalent properties replacing individual sub-components as cathode, separator, anode and electrolyte. The parallel connection between the constituent unit cells in the entire pouch cell was also verified based on a set of relevant calculations.

Two specific load cases (2C and WLTC) employed in the simulations demonstrated the nature of temperature distribution throughout the cell volume. It was concluded that the positive tab was the part having the highest temperature at 3.3 °C above the lowest temperature point at the cell bottom for a constant current of 2C. When the positive tab was ignored, the region below the tab where its current collectors were in contact with the active/lumped material was the next high temperature hot spot with a maximum at a depth of half the cell thickness. On an average, the cell core temperature was observed to be at 0.5 °C higher than at surface up to the upper 25% the cell height distance below the tabs. In case of the WLTC, the maximum temperature was reached at the time instant of 1571 s and the extreme temperature difference reached 1.9 °C while the difference between core and surface maxed out at mere 0.1 °C. In pulse tests at high SoC, almost the same temperature rise was observed as the same magnitude constant current. However, the variations were significant at low SoC pulse tests.

The cooling systems using conventional and enhanced temperature control parameters depicted relatively more prolonged duration of operation in the enhanced system which used the core temperature as control parameter based on the em-

pirical relation with surface temperature. As only a single WLTC and 2C cycles were run, minimal excess battery usage and hence higher drop in SoC was observed due to longer compressor (cooling system) operation in the enhanced cooling model. However, the improvement in service life due to the optimum cell temperature maintenance could not be quantified, hence paving a way to providing a compelling scope for future studies.

5.2 Future Scope

Most of the assumptions considered in the present study could be addressed and quantified analytically. A few of them are mentioned below, which can act as the outset for further advancements.

A more detailed 3-D multi-physics model including all contributing physics of electrical, chemical, thermal and mechanical could be created and the ageing phenomenon from chemical degradation integrated into the effects on other physics would provide a whole realistic model.

Quantifying contact resistance, both thermal and electrical could explain the temperature drops across individual layers and how increased pressure of the assembly and operation could vary over the service life as the cell ages. Instead of lumping the active parts of the cell, all layers could be modeled as found in a real cell and the charge trajectories through tortuous pores through the cell could be traced.

The capacitive nature of the cell as modeled from RC circuits could be accommodated in the multi-physics model and gradual variations at step responses would provide and relate to real cell behaviors. Instead of using empirical equations from the test carried out on test rigs or finite element simulations, an analytical approach needs to be developed where the temperature at any point in the cell volume is a function of the state of charge, C-rate, temperature, heat transfer coefficient, thermal conductivity, electrical conductivity and other related parameters.

From the cooling system perspective, an elaborate model with a PID controller and a radiator- A/C combined cooling system could be employed. Each module with reasonable quantification of cooling channels and effective cooling area available could be modeled as well. Even an algorithm which channels the heat dissipated from the cell to a cabin heater could be created. Repetitive standard drive cycles and on-board live control and diagnostics could be run and machine learning algorithms could be implemented which could plan the cooling strategies based on the GPS data of specific journeys. A study on improvement of the battery life due to the optimum temperature maintenance could also be explored.

Bibliography

[1] Sectoral greenhouse gas emissions by IPCC sector, https://www.eea.europa.eu/data-and-maps/daviz/change-of-co2-eq-emissions-2#tab-dashboard-01

[2] Wittmann, Jochen. (2017). Electrification and Digitalization as Disruptive Trends: New Perspectives for the Automotive Industry? 10.1007/978-3-319-44468-09

[3] CO_2 Emission by sector, https://ourworldindata.org/grapher/carbon-dioxide-co2-emissions-by-sector-or-source

[4] IEA (2019), 'Global EV Outlook 2019', IEA, Paris https://www.iea.org/reports/global-ev-outlook-2019

[5] Annual Li-Ion battery demand year by year, https://seekingalpha.com/article/4289626-look-top-5-lithium-ion-battery-manufacturers-in-2019

[6] Omtanke Sustainability, https://group.volvocars.com/sustainability

[7] D. Andrea, *Battery Management Systems for Large Lithium-Ion Battery Packs*, ISBN-13 978-1-60807-104-3

[8] Lead Acid vs Li-Ion Batteries https://www.autonom.ca/lead-acid-vs-lithium-ion-batteries/

[9] Rajath Kantharaj, Amy M. Marconnet (2019) *Heat Generation and Thermal Transport in Lithium-Ion Batteries: A Scale-Bridging Perspective, Nanoscale and Microscale*, Thermophysical Engineering, 23:2, 128-156, DOI: 10.1080/15567265.2019.1572679

[10] Sun, P., Bisschop, R., Niu, H. et al., *A Review of Battery Fires in Electric Vehicles*,Fire Technology 56, 1361–1410 (2020)

[11] M. Nikowitz, *Advanced Hybrid and Electric Vehicles: System Optimization and Vehicle Integration*, Springer, 2016

[12] Jiuchun Jiang, Caiping Zhang, *Fundamentals and Applications of Lithium-ion Batteries in Electric Drive Vehicles*, John Wiley & Sons INC International Concepts

[13] C.Julien, Z.Stoynov, *Materials for Lithium-Ion Batteries*, Springer Netherlands, 2000

[14] Dafen Chen, Jiuchun Jiang, Heon Kim, Chuanbo Yang, Ahmad Pesaran, *Comparison of different cooling methods for lithium ion battery cells*,Journal of Applied Thermal Engineering, vol. 94, pg. 846-854, 2016

[15] The History of the Electric Car, September 2015 https://www.energy.gov/articles/history-electric-car

[16] Gustave Trouvé's tricycle from Jacques Cattelin
http://academie-de-touraine.com/Tome_25_files/067-092.pdf

[17] Advanced Hybrid and Electric Vehicles
https://doi.org/10.1007/978-3-319-26305-2

[18] Voltage Classes for Electric Mobility,
https://www.zvei.org/fileadmin/user_upload/Presse_und_Medien/Publ-ikationen/2014/april/Voltage_Classes_for_Electric_Mobility/Voltage_Classes_for_Elec_Mobility.pdf

[19] Cheng, Ming and Sun, Le and Buja, G. and Song, Lihua. (2015). Advanced Electrical Machines and Machine-Based Systems for Electric and Hybrid Vehicles. vol. 8, Energies, pg. 9541-9564, 10.3390/8099541

[20] Y. Cengel, A. Ghazar*Heat and Mass Transfer - Fundamentals and Applications*, Fifth edition, ISBN-13: 978-0073398181

[21] C. Madhusudana, *Thermal Contact Conductance*, Second edition,DOI 10.1007/978-3-319-01276-6, ISBN 978-3-319-01276-6

[22] S. Stewart, V. Srinivisan J. Newman (2008) *Modeling the performance of lithium-ion batteries and capacitors during hybrid-electric-vehicle operation*, Journal of The Electrochemical Society, vol:155, issue: 9, DOI: 10.1149/1.2953524

[23] M. Krepelkov *Evolution of batteries:From experiments to everyday usage*, Department of Economics, Management and Humanities, Czech Technical University, Prague, Czech Republic

[24] Supercapacitors: A Comparative Analysis,
https://www.exponent.com/ /media/news-events-alerts/alerts/2018/02/supercapacitors/supercapacitors-a-comparative-analysis.pdf

[25] MIT Electric Vehicle, *A guide to understanding battery specifications*

[26] E. Wikner, *Ageing in Commercial Li-ion Batteries:Lifetime Testing and Modelling for Electrified Vehicle Applications*, Doktorsavhandlingar vid Chalmers tekniska högskola Ny serie nr. 4633, ISBN 978-91-7905-166-2

[27] Berg H; Batteries for Electric Vehicles: Materials and Electrochemistry
Cambridge University Press, ISBN: 9781316371633

[28] How Does a Lithium-ion Battery Work?
https://www.energy.gov/eere/articles/how-does-lithium-ion-battery-work

[29] Cell stacking processes for lithium-ion cells
https://www.youtube.com/watch?v=ESvVLEwXYwM

[30] Skoog S, David S *Parameterization of linear equivalent circuit models over wide temperature and SOC spans for automotive lithium-ion cells using electrochemical impedance spectroscopy*,Journal of Energy Storage, vol 14, part 1, pg. 39-48, https://doi.org/10.1016/j.est.2017.08.004

[31] Barth T, Swaim R; *NTSB investigation of EV fires*, Electrical Vehicle Safety IWG, Global Technical Regulation Session 16

[32] Yao X, Biswas A; *Mild Hybrid Electro-Thermal Battery Modelling*, Division of Electric Power Engineering, Chalmers University of Technology

[33] Ma S, Jiang M, Tao P, Song C, Wu J, Wang J, Deng T, Shang W *Temperature effect and thermal impact in lithium-ion batteries: A review*, Progress in Natural

Science: Materials International, Vol. 28, Issue 6, December 2018, Pg 653-666, https://doi.org/10.1016/j.pnsc.2018.11.002

[34] Bandhauer T M,Garimella S, Fuller T F, *A Critical Review of Thermal Issues in Lithium-Ion Batteries*, Journal of The Electrochemical Society, Vol. 158, issue 3, https://iopscience.iop.org/article/10.1149/1.3515880

[35] Kantharaj R, Marconnet A M, *Heat Generation and Thermal Transport in Lithium-Ion Batteries: A Scale-Bridging Perspective*, Nanoscale and Microscale Thermophysical Engineering, Vol. 23, issue 2, Pg 128-156, https://doi.org/10.1080/15567265.2019.1572679

[36] Electrical conductivity and temperature co-efficient https://www.cirris.com/learning-center/general-testing/special-topics/177-temperature-coefficient-of-copper

[37] Transportation, Air Pollution, and Climate Change https://www.epa.gov/transportation-air-pollution-and-climate-change

[38] A/C introduction in passenger cars https://www.50states.com/facts/michigan.htm

[39] Baum L, Bidari S, Danaraddi S, Jiang B, Satishkumar, Simpi P; *Automotive Thermal Management for Performant Battery Systems & Rotor Cooled Induction Machine as Traction Machine*, Division of Electric Power Engineering, Department of Mechanics and Maritime Sciences, Chalmers University of Technology

[40] Dincer I, Hamut H, Nader Javani N; Thermal Management of Electric Vehicle Battery Systems
JohnWiley Sons Ltd, ISBN: 978-1-118-90022-2

[41] Dinakar P, Rajeeve G; *Modelling and Simulation of Cooling Systems for BEV High Voltage Battery*, Division of Vehicle Engineering and Autonomous Systems, Chalmers University of Technology; ISSN 1652-8557

[42] Finite Element vs Finite Volume https://knowledge.autodesk.com/support/cfd/learn-explore/caas/CloudHelp/cloudhelp/2014/ENU/SimCFD/files/GUID-12A9AED8-2047-4D3A-BC80-82BE9CF47517-htm.html

[43] What's The Difference Between FEM, FDM, and FVM? https://www.machinedesign.com/3d-printing-cad/fea-and-simulati-/article/21832072/whats-the-difference-between-fem-fdm-and-fvm

[44] Z. Geng, J. Groot T. Thiringer, *A Time and Cost Effective Method for Entropic Coefficient Determination of a Large Commercial Battery Cell*,Transactions on Transportation Electrification, vol. 6, no. 1, pp. 257-266, March 2020, doi: 10.1109/TTE.2020.2971454

[45] Matweb - Material data sheets http://www.matweb.com/

[46] Svens P, Kjell M.H, Tengstedt C, Flodberg G, Lindbergh G, *Li-Ion Pouch Cells for Vehicle Applications — Studies of Water Transmission and Packing Materials*,Energies 2013, 6(1), 400-410, https://doi.org/10.3390/en6010400

[47] Groot J, KTH, Chalmers, Uppsala Universitet, Scania CV AB, Volvo Cars; *Fast-Charging of Large Energy-optimised Li-ion Cells for Electrified Drivelines*, Volvo Technology AB, BF68700, Energimyndigheten, dt: 2018-12-21